BIOPLASTIC DEVELOPMENT, CHARACTERISATION, AND OPTIMIZATION OF FUSED FILAMENT FABRICATION PARAMETERS

MAURINE NALIAKA ANDANJE

DOCTOR OF PHILOSOPHY IN MECHANICAL ENGINEERING

JOMO KENYATTA UNIVERSITY OF AGRICULTURE AND TECHNOLOGY

2026

Bioplastic Development, Characterisation, and Optimization of Fused Filament Fabrication Parameters

Maurine Naliaka Andanje

A Thesis Submitted in Partial Fulfillment of the Requirements for the Degree of Doctor of Philosophy in Mechanical Engineering of the Jomo Kenyatta University of Agriculture and Technology

2026

DECLARATION

This thesis is my original work and has not been presented for a degree in any other University

Signature……. Date……

Maurine Naliaka Andanje

This thesis has been submitted for examination with our approval as the University Supervisors

Signature……. Date……

Dr. -Ing. James Wamai Mwangi

JKUAT, Kenya

Signature……. Date……

Bruno Roberts Mose, PhD, PostDoc, PE, MIEK

JKUAT, Kenya

Signature……. Date……

Prof. Sandro Carrara, PhD

EPFL, Switzerland

DEDICATION

To my three children, Zoey Imora, Zuri Hawi, and Zayn Hera; my parents, Mr. and Mrs. Andanje; and my siblings, David, Vivian, Collins, Ruth, and Esther.

ACKNOWLEDGEMENT

First and foremost, I am deeply grateful to God Almighty for His faithfulness, love, and mercies during this journey. His guidance and strength have seen me through the successful completion of this research.

Secondly, I am incredibly grateful to my supervisors for their invaluable input, guidance, and feedback throughout this research. To Dr. Ing James Wamai Mwangi, I am grateful for walking with me every step of this journey. Your expertise in the field of Additive Manufacturing and your words of encouragement have been a pillar of hope. My co-supervisor from École Polytechnique Fédérale de Lausanne (EPFL), Prof. Sandro Carrara, for his thoughtful comments, recommendations, and hospitality during my research visit to his Lab at EPFL, Neuchâtel campus. Dr. Bruno Mose for his expertise in Materials Engineering and contributions, especially during material development and characterization.

Special appreciation to the teaching and technical staff at Mechatronic Engineering in JKUAT for their consistent support during this research period. Mr. Matunda for always going out of his way to assist in conducting experiments and analyzing data. The SustainAM project, a collaboration between JKUAT and Technische Universität Bergakademie Freiberg (TUBAF), Germany, for availing machines and equipment for use in the Advanced Manufacturing Laboratory in JKUAT. The project members with whom I was also part, for their contribution and positive criticism of my work during seminars and conference presentations. I am greatly indebted to Mr. Green Africa for allowing access to their laboratories for practical work.

I wish to acknowledge and sincerely thank Excellence in Africa (EXAF), 100 Ph.Ds for Africa Programme, for the scholarship award which funded this PhD study. The scholarship has supported my studies and staff training, and the procurement of a high-performance 3D printer, the Creatbot F430. Lastly, to my husband and three children for their cheerfulness, encouragement, and patience during the entire research period.

TABLE OF CONTENTS

DECLARATION ..... **ii**

DEDICATION ..... **iii**

ACKNOWLEDGEMENT ..... **iv**

TABLE OF CONTENTS ..... **v**

LIST OF TABLES ..... **xi**

LIST OF FIGURES ..... **xiv**

LIST OF APPENDICES ..... **xix**

ABBREVIATIONS AND ACRONMS ..... **xx**

LIST OF SYMBOLS ..... **xxiii**

ABSTRACT ..... **xxv**

CHAPTER ONE **1**

INTRODUCTION **1**

1.1 Overview 1

1.2 Background of Biocomposites 1

1.3 Biocomposite Development 3

1.3.1 Processing Methods of Biocomposites 3

1.4 Additive Manufacturing of Fiber-Reinforced Polymer Composites 5

1.4.1 Material Extrusion Methods 6

1.5 Application of Biocomposites 6

1.6 Challenges Associated with Application of Biocomposites 7

1.7 Problem Statement 8

1.8 Objectives 9

1.9 Justification of the Study 10

1.10 Thesis Structure 11

CHAPTER TWO 12

LITERATURE REVIEW 12

2.1 Overview 12

2.2 Theoretical Background 12

2.3 Techniques for Developing Biocomposites 14

2.3.1 Extrusion Process 14

2.3.2 Injection Molding 15

2.3.3 Compression Molding 15

2.3.4 Pultrusion 15

2.4 Characterization Techniques of 3D Printed Products from Biocomposites 16

2.4.1 Mechanical Properties of Biocomposite Parts 16

2.4.2 Thermal Properties of Biocomposite Parts 21

2.5 Fused Filament Fabrication of Biocomposites 23

2.5.1 Process Parameters of Fused Filament Fabrication 24

2.5.2 Optimization Techniques Used in Fused Filament Fabrication 28

2.6 Previous Research on Biocomposites from HDPE and Rice Husks 34

2.7 Summary of the Research Gaps 38

CHAPTER THREE 39

METHODOLOGY.....39

3.1 Overview 39

3.2 Development of Bioplastics 39

3.2.1 Materials for the Bioplastic Development 40

3.2.2 Biofilament Fabrication 41

3.3 Bioplastic Characterization 45

3.3.1 Fused Filament Fabrication (FFF) of the Developed Bioplastics 45

3.3.2 Mechanical Characterization of the Developed Bioplastics 47

3.3.3 Thermal Properties 49

3.3.4 Morphological Analysis of the Developed Bioplastics 49

3.3.5 Surface Roughness Analysis of the Developed Bioplastics 50

3.3.6 Biodegradability Analysis of the Developed Bioplastics 50

3.3.7 Chemical Composition Analysis of the Developed Bioplastics 52

3.4 Simulation of the Printing Process 52

3.4.1 Generation of Digimat-AM Material Cards 52

3.4.2 Reverse-Engineering in Digimat-MX 59

3.4.3 Fused Filament Fabrication Process Simulation 64

3.4.4.Taguchi Design of Experiment and Optimization using Grey Relational Analysis 69

3.4.5 Structural Modeling 71

3.4.6 Structural Analysis - Coupled Simulation 72

3.4.7 Experimental Validation of the Fused Filament Fabrication 75

3.4.8 Experimental Validation of Warpage Measurement 75

3.4.9 Experimental Validation of Residual Stress Measurement 76

3.4.10 Building of Biosensor Substrate from Developed Material 78

CHAPTER FOUR 80

RESULTS AND DISCUSSION 80

4.1 Overview 80

4.2. Properties of Milled Rice Husks 80

4.3 Fabricated Biofilaments 83

4.4 Characterization of Biofilaments 90

4.4.1 Fused Filament Fabrication of Developed Biofilaments 90

4.4.2 Mechanical Properties of the Bioplastics 92

4.4.3 Thermal Properties of the Bioplastics 97

4.4.4 Morphological Properties of the Bioplastics 100

4.4.5 Surface Roughness Properties of the Bioplastics 103

4.4.6 Fourier Transform Infrared Spectroscopy Analysis 106

4.4.7 Biodegradation Properties of the Bioplastics 107

4.5 Simulation Results of the Fused Filament Fabrication Process 112

4.5.1 Warpage and Residual Stress for the 100 wt. % rHDPE 113

4.5.2 Warpage and Residual Stress for the 85 wt. % rHDPE + 15 wt.% RH 119

4.5.3 Warpage and Residual Stress for the 40% rHDPE + 30 % RH + 30 % MAPE 124

4.6 Multi-Objective Optimization using Grey Relational Analysis 131

4.7 Structural Analysis – Coupled Simulation 133

4.7.1 Structural Results: Total Strain 134

4.7.2 Structural Results: Failure Indicator 135

4.8 Validation of the Printing Simulation Using Experimental Results 137

4.8.1 Warpage Measurement of the Part Printed 137

4.8.2 Residual Stress Analysis of Printed Samples from the Bioplastic 139

4.8.3 Biosensor Fabrication from the Bioplastic 144

CHAPTER FIVE 145

CONCLUSIONS AND RECOMMENDATIONS 145

5.1 Conclusions 145

5.2 Recommendations 147

REFERENCES 148

APPENDICES 165

LIST OF TABLES

Table 2.1: A Summary of Research on the Optimization of FFF Process Parameters....34

Table 3.1: Properties of rHDPE....40

Table 3.2: Properties of MAPE....41

Table 3.3: Different Compositions of the Bioplastic....42

Table 3.4: Extrusion Process Parameters and their Levels....43

Table 3.5: L_9 Taguchi Experimental Design....44

Table 3.6: Printing Parameters for the Biofilaments. 46

Table 3.7: Experimental Properties of the Developed Bioplastics....53

Table 3.8: Properties of the Rice Husk Filler....54

Table 3.9: Input Factors for the FFF Simulation and their Levels....67

Table 3.10: Factors Kept Constant for the FFF Simulation....67

Table 3.11: Taguchi L_9 DoE for the FFF Simulations....69

Table 3.12: Technical Specification Creatbot F430....75

Table 4.1: Response Table for Means for 100 wt.% rHDPE....85

Table 4.2: Response Table for Means for 95 wt.% rHDPE + 5 wt.% RH....86

Table 4.3: Response Table for Means for 90 wt.% rHDPE + 10 wt. % RH....88

Table 4.4: Response Table for Means for 85 wt.% rHDPE + 15 wt.% RH....89

Table 4.5: Thermal Properties of the Biofilaments....98

Table 4.6: FTIR Wave Number for Various Functional Groups.....107

Table 4.7: Mass Decrement of Biocomposites during Biodegradability Analysis.....109

Table 4.8: Residual Stress and Warpage for the 100 wt. % rHDPE.....113

Table 4.9: Response Table for average Warping of the 100% rHDPE.....114

Table 4.10: Response Table for Signal-to-Noise Ratios of the 100% rHDPE Warpage116

Table 4.11: Response Table for Average Residual Stresses of the 100% rHDPE 118

Table 4.12: Response Table for Signal-to-Noise Ratios of the 100% rHDPE Residual Stresses.....118

Table 4.13: Residual Stress and Warpage for the 85 wt. % rHDPE + 15 wt.% RH Bioplastic.....120

Table 4.14: Response Table for the Signal-to-Noise Ratio of the 85 wt.% rHDPE + 15 wt.% RH Bioplastic's Warpage.....122

Table 4.15: Response Table for Average Warpage of the 85 wt. % rHDPE + 15 wt.% RH Bioplastic. 122

Table 4.16: Response Table for Average Residual Stresses of the 85 wt. % rHDPE + 15 wt.% RH Bioplastic.....124

Table 4.17: Response Table for Signal-to-Noise Ratios of the 85 wt. % rHDPE + 15 wt.% RH Residual Stresses 124

Table 4.18: Residual Stress and Warpage for the 40 wt. % rHDPE + 30 wt. % RH + 30 wt. % MAPE Bioplastic 125

Table 4.19: Response Table for Average Warpage of the 40 wt. % rHDPE + 30 wt. % RH + 30 wt. % MAPE Bioplastic. 128

Table 4.20: Response Table for the Signal-to-Noise Ratio of the 40 wt. % rHDPE + 30 wt. % RH + 30 wt. % MAPE Bioplastic's Warpage 128

Table 4.21: Response Table for Average Residual Stresses of the 40 wt. % rHDPE + 30 wt. % RH + 30 wt. % MAPE Bioplastic 130

Table 4.22: Response Table for Signal-to-Noise Ratios of the 40 wt. % rHDPE + 30 wt. % RH + 30 wt. % MAPE Residual Stresses 130

Table 4.23: Grey Relational Analysis for the 100 wt.% rHDPE 131

Table 4.24: Grey Relational Analysis for the 85 wt. % rHDPE + 15 wt.% RH Bioplastic.....132

Table 4.25: Grey Relational Analysis for the 40 wt. % rHDPE + 30 wt. % RH + 30 wt. % MAPE Bioplastic 132

Table 4.26: Comparison of Measured and Simulated Average Values of Longitudinal Warpage.....138

Table 4.27: Comparison of Measured and Simulated Average Values of Residual Stresses 143

LIST OF FIGURES

Figure 1.1: Additive Manufacturing Technologies 5

Figure 2.1: (A) The Extrusion Process. (B) The Injection Molding. (C) Compression Molding. (D) Pultrusion Process 16

Figure 2.2: Typical Engineering Stress-Strain Curve.....18

Figure 2.3: Strain-Stress Curves of PHBHV Biocomposites with 5 wt.% Fibre, Sample 1 (0 wt.% DCP), Sample 2 (0.25 wt.% DCP), and Sample 3 (2.2 wt.% DCP).....19

Figure 2.4: Thermogravimetric Analysis Curves of PLA, Lignin, and PLA/Lignin Biocomposites.....22

Figure 2.5: a. Large Layer Thickness b. Small Layer Thickness.....25

Figure 2.6: a. Print Orientations b. Raster Direction Angle at 0°, and Layer Thickness 26

Figure 2.7: Different Process Parameters of FFF.....27

Figure 2.8: Commonly Used Infill Patterns 28

Figure 2.9: The Genetic Algorithm Process Flow.....29

Figure 2.10: Steps in Implementing the Taguchi Method of Optimization 30

Figure 2.11: Basic Architecture of an Artificial Neural Network 32

Figure 3.1: The SJ35 Single-Screw Filament Extrusion System 44

Figure 3.2: Prusa i3 MK3S+ 46

Figure 3.3: Experimental Set-Up of the Tensile Test 49

Figure 3.4: Experimental Set-Up for Biodegradability Analysis 51

Figure 3.5: Process Flow from Test Data to Digimat-AM Software Cards 54

Figure 3.6: Calibration of the E-Modulus and Filler Properties on the Thermo-Elastic Material Card 58

Figure 3.7: Calibration of the Thermal Conductivity and Specific Heat Capacity of the Resin on the Thermal Material Card 58

Figure 3.8: Digimat-AM Database Displaying Created Material Files 59

Figure 3.9: Reverse-Engineering to Calibrate the Matrix Density 62

Figure 3.10: Reverse-Engineering of the Matrix Stiffness and Material Microstructure 62

Figure 3.11: Reverse-Engineering of the Matrix Coefficient of Thermal Expansion (CTE) 64

Figure 3.12: ASTM D638 - Type IV Tensile Specimen (Dimensions in mm) 65

Figure 3.13: CAD Drawings of the Breath Analyzer 65

Figure 3.14: Workflow for the Prediction of Warpage and Residual Stress in FFF Simulation 66

Figure 3.15: Screenshot of the Tensile Test Sample in Digimat Software 68

Figure 3.16: Screenshot of the Meshed Geometry of the Breath Analyzer Adapter 68

Figure 3.17: Illustration of the Coupled Models 72

Figure 3.18: Steps in Building a Coupled Simulation 73

Figure 3.19: Illustration of the Mapping of Toolpath Information to the FEA Mesh 74

Figure 3.20: Illustration of the Orientation Tensor after Mapping.....74

Figure 3.21: Navigation Image of the Printed Part 76

Figure 3.22: X-Ray Diffraction Geometries during the Investigation 78

Figure 3.23: Microfluidic Substrate 79

Figure 4.1: Cumulative Distribution of the Milled Rice Husks 81

Figure 4.2: Aspect Ratio of Milled Rice Husks 82

Figure 4.3: Sphericity of the Milled Rice Husks 82

Figure 4.4: Fabricated Biofilaments with Different Compositions.....84

Figure 4.5: Fabrication Parameters According to Rank 85

Figure 4.6: Main Effect Plot for Means -100 wt. % rHDPE.....86

Figure 4.7: Main Effect Plot for Means - 95 wt. % rHDPE + 5 wt. % RH.....87

Figure 4.8: Main Effect Plot For Means – 90 wt.% rHDPE + 10 wt.% RH 88

Figure 4.9: Main Effect Plot for Means – 85 wt.% rHDPE + 15 wt.% RH 89

Figure 4.10: Printed Tensile Test Sample.....91

Figure 4.11: Mechanical Properties of the Biofilaments.....93

Figure 4.12: Stress-Strain Curves of the Biofilaments.....94

Figure 4.13: Flexural Properties of the Biofilaments.....95

Figure 4.14: Maximum Compression Stress of the Biofilaments. 96

Figure 4.15: Crystallinity of the Developed Biofilaments 99

Figure 4.16: Enthalpy of the Developed Biofilaments 99

Figure 4.17: Glass Transition Temperature, Onset of Melting, and Peak Melting Temperature 100

Figure 4.18: SEM Images of the Biofilaments' External Surface and Cross-Section...101

Figure 4.19: SEM Images of the Fractured Tensile Sample 102

Figure 4.20: Surface Roughness of the Developed Biofilaments 105

Figure 4.21: Roughness average (Ra) of the Developed Biofilaments.....105

Figure 4.22: FTIR Spectrum of the Developed Biofilaments.....107

Figure 4.23: Mechanical Properties Before and After Biodegradability 110

Figure 4.24: Moisture Content in the Biofilament.....111

Figure 4.25: Simulation Results of 100 wt.% rHDPE 114

Figure 4.26: Main Effect Plot for Warpage of 100 wt.% rHDPE (a) Means (b) SN Ratio.....115

Figure 4.27: Main Effect Plot for Residual Stresses of 100 wt.% rHDPE (a) Means (b) SN Ratio.....117

Figure 4.28: Simulation Results of 85 wt. % rHDPE + 15 wt.% RH Bioplastic.....120

Figure 4.29: Main Effect Plot for Warpage (a) Means (b) SN Ratio of 85 wt. % rHDPE + 15 wt.% RH Bioplastic. 121

Figure 4.30: Main Effect Plot for Residual Stresses (a) Means (b) SN Ratio of 85 wt. % rHDPE + 15 wt.% RH Bioplastic.....123

Figure 4.31: Simulation Results of 40 wt. % rHDPE + 30 wt. % RH + 30 wt. % MAPE Bioplastic 126

Figure 4.32: Main Effect Plot for Warpage (a) Means (b) SN Ratio of 40 wt. % rHDPE + 30 wt. % RH + 30 wt. % MAPE Bioplastic.....127

Figure 4.34: Orientation Tensor after Mapping (Toolpath to the FEA Model).....134

Figure 4.35: Total Strain of the 85 wt.% rHDPE+15wt.% RH Bioplastic.....135

Figure 4.36: Failure Indicator of the 85 wt.% rHDPE+15wt.% RH Bioplastic.....136

Figure 4.37: Points for Warpage Measurement: (a) Longitudinal Measurement, (b) Lateral Measurements.....137

Figure 4.38: 3D Image of Warped Part 138

Figure 4.39: Total Profile of Warped Printed Part. (a) Center Profile, (b) Top Profile, (c) Bottom Profile 139

Figure 4.40: Combined XRD Spectra of the Bioplastic Samples.....140

Figure 4.41: XRD Spectra of the Bioplastics Illustrating the Different Profiles at the Y-Offset.....141

Figure 4.42: A Plot of Strain ε vs $\sin^2 \psi$ for the 100% rHDPE.....142

Figure 4.43: A Plot of Strain ε vs $\sin^2 \psi$ for the 85% rHDPE + 15% Bioplastic 142

Figure 4.44: A Plot of Strain ε vs $\sin^2 \psi$ for the 40% rHDPE + 30% RH + 30% MAPE Bioplastic 143

Figure 4.45: Printed Biomedical Devices from the Bioplastic (a) Microfluidic Substrate (b) Microfluidic Chip.....144

LIST OF APPENDICES

Appendix I: Material Model Definition..... 142

Appendix II: Measured Warpage..... 144

Appendix III: FFF Simulation Results……... 145

Appendix IV: Modules of Digimat 2024.1 148

ABBREVIATIONS AND ACRONMS

ABS	Acrylonitrile Butadiene Styrene
AM	Additive Manufacturing
ANN	Artificial Neural Networks
ANOVA	Analysis of Variance
ASTM	American Society for Testing and Materials
CAD	Computer-Aided Design
CIJ	Continuous Inkjet
CTE	Coefficient of Thermal Expansion
DCP	Dicumylperoxide
DIW	Direct Ink Writing
DOD	Drop-On-Demand
DOE	Design of Experiments
DSC	Differential Scanning Calorimetry
EPDM-g-MAH	Ethylene-Propylene-Diener Monomer Grafted Maleic Anhydride
FEA	Finite Element Analysis
FEM	Finite Element Method
FFF	Fused Filament Fabrication
FTIR	Fourier Transform Infrared

GA	Genetic Algorithms
GC	Gas Chromatography
GRG	Grey Relational Grade
HP	Hewlett-Packard
LDM	Liquid Deposition Modelling
LOM	Laminated Object Manufacturing
MAPE	Maleic Anhydride-grafted Polyethylene
MAPP	Maleated Polypropylene
MX	Material Exchange
MF	Mean Field
MS	Mass Spectrometer
MS	Multiscale Solution
PA	Polyamide
PC	Polycarbonate
PE	Polyethylene
PEEK	Polyether Ether Ketone
PEI	Polyetherimide
PET	Polyethylene Terephthalate
PHA	Polyhydroxyalkanoates

PHBHV	Poly(3-Hydroxybutyrate-co-3-Hydroxyvalerate)
PLA	Polylactic Acid
PP	Polypropylene
PSO	Particle Swarm Optimization
SEM	Scanning Electron Microscopy
SFF	Solid Freeform Fabrication
STL	Standard Tessellation Language or Stereolithography
TE	Thermo-Elastic
TGA	Thermogravimetric Analysis
TGRA	Taguchi Grey Relational Analysis
TLBO	Teaching-Learning-Based Optimization
TMA	Thermomechanical analysis
TPU	Thermoplastic Polyurethane
TVE	Thermo-Viscoelastic
rHDPE	Recycled High-Density Polyethylene
RP	Rapid Prototyping
RSM	Response Surface Method
RTM	Resin Transfer Molding
VA	Virtual Allowable

LIST OF SYMBOLS

$\boldsymbol{\alpha}$	Coefficient of thermal expansion
$\boldsymbol{e}$	Error estimator
$\boldsymbol{\sigma}$	Stress (MPa)
$\boldsymbol{\varepsilon}$	Strain
$\boldsymbol{\delta}$	Mid-span deflection (mm)
$\boldsymbol{\lambda}$	Grey Relational Unique's coefficient
$\boldsymbol{A}$	Area (mm^2)
c	Specific heat of the material (J/kg K)
$\boldsymbol{d}$	Thickness (mm)
$\boldsymbol{F}$	Force (N)
$\mathbf{E}$	Modulus of elasticity (MPa)
$\boldsymbol{L}$	Length (mm)
$\boldsymbol{k}$	Thermal conductivity (W/m-K)
$\boldsymbol{t}$	Time (seconds)
$\boldsymbol{\rho_{composite}}$	Density of the composite
$\boldsymbol{\rho_{filler}}$	Density of the filler

f	Filler fraction
ρ_{matrix}	Density of the matrix/resin
R_z	Maximum height of the profile / The mean roughness depth
R_q	Root mean square roughness
R_a	Roughness average

ABSTRACT

Additive manufacturing, commonly known as 3D printing, is a rapidly expanding technology that has the potential to support a circular and sustainable economy. This technology supports a wide variety of raw materials and offers design flexibility, expanding its use in prototype and custom part production. One of the most common additive manufacturing technologies is Fused Filament Fabrication (FFF), which utilizes thermoplastic polymers as the raw material. Thermoplastic polymers commonly used in FFF include polylactic acid (PLA), acrylonitrile butadiene styrene (ABS), polyamide (PA), polycarbonate (PC), and Nylon 12. Despite its popularity, high-density polyethylene has not been thoroughly studied in fused filament fabrication due to problems with warping and significant thermal shrinkage of printed parts after solidifying. It has been suggested that adding organic fillers will lessen these difficulties. The use of organic fillers in polymers results in biocomposites that have improved thermal properties and potential for biodegradation. However, printability, low-layer agglomeration, and reduced mechanical properties are some of the challenges that have to be overcome during FFF. Determining the best combination of printing parameters can significantly improve the printability of these biocomposites. In this study, rice husk waste was used as an organic filler in recycled high-density polyethylene to develop a biofilament for FFF. High-density polyethylene was chosen as the polymer since, though it is highly recyclable, it has not qualified as a potential raw material in FFF. This is due to challenges such as high thermal shrinkage that causes it to warp during printing. Organic fillers in polymers have been recommended as a means of reducing warpage of HDPE and enhancing printing directionality. Through the design of an experiment, various filler-to-polymer combinations were tested with the addition of a compatibilizer to enhance the filler's miscibility in the polymer matrix. Using the ball mill, the rice husks were ground into powder with particles smaller than 75 μm. The biofilament's highest composition included 35 wt.% rice husk filler, 35 wt.% recycled high-density polyethylene, and 30 wt.% compatibilizer, indicating an improvement in rice husk filler content compared to earlier research. Digimat 2024.1 was used as the platform for material modeling and printing simulation to identify printing issues, such as warpage and residual stresses. Through a coupled simulation, a finite element model was analyzed to predict part performance. The model was validated experimentally using the standard tensile test specimen. The Taguchi Grey Relational Analysis (TGRA) was used to optimize the printing process due to its efficiency and robustness for multi-response experiments. Printability was successful up to the biofilament whose composition comprised 30 wt.% rice husk filler, 40 wt.% recycled high-density polyethylene, and 30 wt.% compatibilizer. This biofilament's mechanical properties included a tensile strength of 8.53 MPa with a standard deviation of 1.32 MPa, a tensile modulus of 128.56 MPa with a standard deviation of 13 MPa, and a maximum tensile strain of 6.6% with a standard deviation of 0.03%. Experimental validation of warpage yielded a maximum error margin of 5.43%, while validation of residual stresses resulted in a maximum error margin of 5.56%. The incorporation of rice husk filler, a natural reinforcement, into recycled high-density polyethylene improved the crystallinity of the biofilaments, which helped reduce shrinkage and warpage in printed parts. Biodegradability was also enhanced up to 10 % in a period of 24 weeks. The outcome of this study will provide valuable

information for the manufacture of functional parts, such as biomedical devices, including microfluidic substrates, from biocomposite materials using FFF.

CHAPTER ONE

INTRODUCTION

1.1 Overview

This chapter provides an overview of biocomposites, including additive manufacturing technologies for manufacturing bioplastic parts, their applications, opportunities, and challenges associated with their use. Additionally, the problem statement, objectives, and research justification are presented.

1.2 Background of Biocomposites

Biocomposites are a subset of composite materials that offer a contemporary and sustainable alternative to conventional composites. By using natural fibers and biodegradable matrices, they create durable materials that address current sustainability issues and help lower carbon footprints. While biodegradable matrices (natural or synthetic polymers) ensure material cohesiveness and contribute to their ecological qualities, natural fibers such as flax, hemp, and bamboo lend biocomposites their mechanical strength and rigidity. In contrast to conventional composites composed of petroleum-based matrices and synthetic fibers, biocomposites are recyclable and compostable, allowing them to be included in a circular life cycle (Vizureanu et al., 2025).

Bioplastics, defined as polymers that are either biodegradable or bio-derived from renewable natural resources, present a great promise as an alternative to conventional plastics, given their potential for biodegradability and biocompatibility (Pilla, 2011; Syed Ali Ashter, 2016). Biodegradable bioplastics offer disposal techniques that lessen the amount of plastic debris that enters the environment. Also, bioderived bioplastics enable a notable decrease in carbon emissions during the resource extraction phase. Currently, cellulose or starch components are the sources of biomass used to create bioplastics. The biodegradability of a bioplastic is determined by its chemical structure;

for instance, a bioplastic that is entirely bioderived may not be biodegradable (Heylin, 2019).

There are various manufacturing techniques available to make engineering products or parts. These include casting, machining, powder metallurgy, metal forming, 3D printing, and 4D printing. Among these, 3D/4D printing is a popular and emerging field with the potential to create sustainable and cost-effective products for the healthcare and packaging industries. The popularity of 3D/4D printing accrues from its capability to utilize waste materials like biowaste (e.g., eggshells, marine eel skin, sheep wool, and lignocellulosic agricultural waste) as well as recycled plastics to produce medical devices and components, offering both environmental and economic benefits. Using waste materials reduces reliance on virgin materials, minimizes landfill waste, and promotes a circular economy.

The American Society of Testing and Materials (ASTM) defines additive manufacturing (AM), which was developed in the 1980s, as "the process of joining materials to make objects from 3D model data, usually layer upon layer, as opposed to subtractive manufacturing methodologies." (ASTM International [ASTM], 2013). Additive manufacturing is also commonly referred to as 3D printing, rapid prototyping (RP), or solid freeform fabrication (SFF). The ASTM classifies additive manufacturing (AM) technologies into various categories, including material extrusion, binder jetting, direct energy deposition, powder bed fusion, material jetting, photo-polymerization, and vat sheet lamination. Although each category has a number of unique processes, they are all based on the same principle of selective layer modeling. Due to the stacking of layers, components made with AM technologies exhibit some anisotropy in one direction. By choosing the right orientation when the part is being manufactured, anisotropy can be decreased. Depending on the AM technology, a wide material selection can be used, such as polymers, metals, ceramics, and composites. In a bid to widen the range of materials for AM, bioplastics have recently emerged as a suitable alternative to conventional plastics (Calignano et al., 2017; Gardan, 2016).

In terms of application, AM was first applied in rapid prototyping and tooling (Ngo et al., 2018). Although these areas of application are still being explored, there's an expansion into direct production due to the improved performance of parts made through AM technologies. The medical field, automotive, aerospace, construction, sports and recreation, among others, have been impacted by advancements in AM.

1.3 Biocomposite Development

A biocomposite material is a composite material composed of a resin matrix reinforced with natural fiber. These materials often mimic the structure of the biological components used in the process, while retaining the matrix's strength and ensuring biocompatibility. The matrix phase is composed of non-renewable and sustainable polymers. The matrix holds the fibers together, transfers stresses, and shields them from mechanical damage and environmental deterioration. (Andanje et al., 2023).

Biofibers are also the primary components of biocomposites, which are derived from biological sources, including crop fibers (sisal, cotton, or flax), crop processing byproducts, animal fibers (feathers, kenaf, silk, wool, and hemp), recycled waste paper, and regenerated cellulose fibers (rayon) (Carruthers, 2012; Pilla, 2011; Sengupta et al., 2017).

Biocomposites can be synthesized by reinforcing polymers with plant-based fillers, including various organic compounds. These fillers are used to improve properties of the biocomposites, such as their biodegradability, surface appeal, certain mechanical properties, and cost reduction (Bhagia et al., 2021).

1.3.1 Processing Methods of Biocomposites

The processing of biocomposites is influenced by several factors, including fiber type, fiber content, fiber orientation, fiber geometry (length-to-diameter ratio, long or short), and moisture content. Injection molding, sheet molding, compression molding, extrusion, and resin transfer molding (RTM) are some of the methods used to process

biocomposites. New equipment has emerged that can enhance the processing of biocomposites, including special heating systems, single or dual venting systems for in-line drying, and a range of feeding methods. The size of the product largely determines the manufacturing procedure to be used. While big components are made by open molding, small to medium–sized components are made by injection and compression molding (Faruk et al., 2012; Sengupta et al., 2017).

To determine the performance of the processed parts from biocomposites, various parameters, including tensile, bending, impact, thermal, and erosion properties, were studied. Kumar and Das developed fibrous biocomposites from nettle and poly (lactic acid) fibers using a compression molding process. It was discovered that the biocomposites' tensile, bending, and impact qualities first improved when the amount of nettle fibers was increased to 50 wt. %, after which they declined (Kumar & Das, 2017).

Porras et al. tested the mechanical properties of biocomposites made with a polylactic acid (PLA) matrix reinforced with Manicaria saccifera fibers. These properties included tensile strength and elastic modulus. Using Taguchi's L18 design of experiment, the optimal properties of the biocomposites based on the compression molding process, fiber content, and chemical treatment concentration were determined. From tensile testing, the optimized biocomposite showed improved mechanical properties compared to the untreated biocomposite (Porras et al., 2016).

Additive manufacturing has ushered in a new era in the processing of biocomposites, which were previously dominated by extrusion, injection molding, and compression processes. Incorporating plant-based materials into the plastic matrix reduces the amount of plastic in the composite and improves the utilization of inexpensive, renewable resources. Researchers are exploring additive manufacturing technologies to produce components from natural fiber biocomposites. These biocomposites address the urgent need to replace non-biodegradable plastic composites with more environmentally friendly materials.

1.4 Additive Manufacturing of Fiber-Reinforced Polymer Composites

Additive manufacturing, also referred to as three–dimensional printing (3DP), is a process that creates highly complex and precise 3D components by layer-by-layer material deposition as opposed to traditional machining or forming techniques. Typically, the process starts with a 3D computer-aided design (CAD) model of the part that needs to be produced. This model is then digitally sliced into multiple horizontal cross-sections. The AM machine receives this data and builds each cross-section one on top of the other to produce a 3D part that is represented in a 3D-CAD model. Typically, the printed parts are net-shaped or near net-shaped, mostly ready for use, or only requiring minor finishing, machining, or cleaning (Balla et al., 2019).

Additive manufacturing technologies have the potential to offer innovative methods for designing and producing new materials by mimicking the structure and content of plant cell walls. The seven AM technologies are presented in Figure 1.1, with the commonly utilized biobased materials being: material extrusion and laminated object manufacturing.

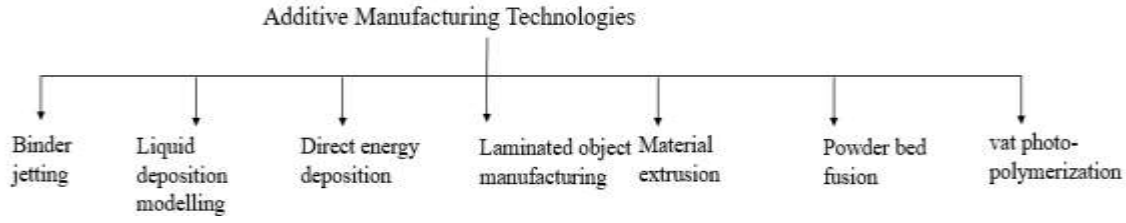

Figure 1.1: Additive Manufacturing Technologies

The processes are best suited for biobased materials due to their nature. The section below elaborates on these processes.

1.4.1 Material Extrusion Methods

This is the most common and widely used additive manufacturing (AM) technology, whereby a nozzle is used to dispense extrudable material and deposit it layer by layer to build a part from a computer-aided design (CAD) model. The popularity of this technology can be attributed to the wide variety of materials that are available for it. This encompasses processes such as fused filament fabrication (FFF), direct ink writing (DIW), liquid deposition modelling (LDM), and micro extrusion 3D bioprinting (Andanje et al., 2023).

The two most popular filament materials for the FFF technique are polylactic acid (PLA) and acrylonitride butadiene styrene (ABS). Other thermoplastic filaments include polyether ether ketone (PEEK), Polyetherketoneketone (PEKK), polyetherimide (PEI), polycarbonates (PCs), and nylon. Poor mechanical properties and low biodegradability are among the reasons limiting the applicability of parts produced by the FFF process.

Furthermore, many applications are constrained by the limited selection of available filament materials. Composite materials can serve as a suitable alternative to overcome the limitations of pure thermoplastic filaments, thereby enhancing material variety, acquiring special qualities, and improving properties (Ferreira et al., 2017). Therefore, investigating novel materials for FFF filaments is crucial for obtaining a variety of material properties to meet diverse application needs (Dey et al., 2023). Dey et al. developed biocomposite filaments from PLA and soy hulls (5 wt. %, 7.5 wt. %, and 10 wt. %) for FFF. Their research demonstrated the printability of the filaments from the biocomposites. The 5 wt. % soy hulls and PLA biocomposite resulted in an improved tensile strength, melt flow index, glass transition, and storage modulus.

1.5 Application of Biocomposites

Biocomposites are increasingly used in the medical field to develop wearable, implantable, and point-of-care devices for remote monitoring of human metabolism. In

light of sustainability efforts, there is a need to address e-waste and the environmental impacts of billions of disposable health-monitoring devices. The use of recycled and biodegradable biocomposites enables the creation of substrates from bioplastics, crop waste, or algae, as well as casings for these devices, thus reducing the ecological footprint of next-gen medical electronics (Carrara, 2025).

Biocomposite materials are used in tissue engineering and regenerative medicine to transform the healing process. These materials imitate the characteristics of genuine tissue by combining biodegradable polymers with bioactive ingredients, which promote cell adhesion and proliferation. Scaffolds guide tissue regeneration by providing mechanical support. Growth factors and stem cells are incorporated into biocomposites, which promote tissue regeneration while degrading without harm. Other applications in the medical field include: drug delivery systems and cardiovascular interventions (Al Mahmud, 2023).

Natural fiber biocomposites are used in the construction industry as building materials, such as hempcrete, concrete beams reinforced with coconut fibers, and wooden beams strengthened using flax fiber (Ahmad et al., 2022). In the automotive industry, biocomposites have gained prominence as natural fiber composites are used to reduce vehicle weight, thus improving energy efficiency (Akampumuza et al., 2017).

Other applications of biocomposites include sustainable food packaging applications (Sánchez-Safont et al., 2018), in marine and in agriculture (Roy et al., 2014).

1.6 Challenges Associated with Application of Biocomposites

The primary challenge that restricts the use of biocomposites is the inconsistencies in the properties of the natural fibers. Their characteristics primarily differ between harvesting seasons or even between plants. These variations in physical properties cause variations in mechanical properties when compared to synthetic fibers (Al-Oqla & Omari, 2017).

Secondly, natural fibers are very susceptible to moisture, making it difficult to use them for packaging, shipping, and long-term storage. Their hydrophilic nature makes them prone to decay and renders them susceptible to microbial activity. Water is absorbed by natural fibers from their surroundings. As a result, the fibers swell and become unstable dimensionally, altering the biocomposite's mechanical and physical characteristics. Surface treatment, however, may help lessen natural fibers' sensitivity to water (Jawaid & Abdul Khalil, 2011).

Incompatibility between non-polar polymeric matrices and polar natural fibers is another disadvantage of biocomposites, leading to poor fiber-matrix adhesion. Poor bonding will have a significant impact on the natural fiber reinforced polymer composites' mechanical properties (AL-Oqla and Sapuan, 2014). Chemical coupling agents can be used to enhance the bonding of fibers to the thermoplastic matrix. Surface modifications is another technique used to enhance this adhesion between the two materials (Faruk et al., 2012b).

Lastly, natural fibers have poor thermal stability, limiting their tolerance to temperatures above 200 °C. High temperatures will result in fiber degradation and subsequent shrinkage. This results in depolymerization, oxidation, hydrolysis, decarboxylation, dehydration, and recrystallization, which alter the fiber's physical and/or chemical structures in the biocomposite. This consequently lengthens the processing time to enhance the fiber's characteristics (Thakur et al., 2012).

1.7 Problem Statement

The industrial application of composites reinforced with natural fibers has gained attention due to the advantages of green technology. They are substituting conventional plastics since they can address environmental issues caused by these plastics. Despite this change in material development, the synthesis of biodegradable biocomposites remains a challenge caused by their diverse range of properties. In terms of processing, the processing of these biocomposites has long been dominated by traditional processes

such as molding, pressing, and extrusion. Additive manufacturing, an advanced production technology, has not been widely used in biocomposites due to printing issues like residual stresses, warpage, and porosity in printed parts.

This study focused on developing biocomposite filaments for additive manufacturing, specifically fused filament fabrication, by using different ratios of recycled high-density polyethylene (rHDPE) and rice husk (RH) waste to examine how these ratios affect the properties of the biofilaments. Despite its popularity, high-density polyethylene has not been extensively studied in fused filament fabrication due to issues such as warping and significant shrinkage of printed parts after solidification. It has been suggested that adding organic fillers can help address these issues. Rice husk waste was chosen as the organic filler because it is plentiful and often discarded in landfills or burned as fuel.

A design of experiments was used to identify the best biocomposite filament for fused filament fabrication by evaluating the characteristics of the fabricated biofilaments. Furthermore, the process parameters were optimized to identify optimal printing conditions that minimize residual stresses and warpage in the printed parts. The optimal process parameters for the biocomposite composition with 40 wt. % rHDPE, 30 wt. % RH and 30 wt. % MAPE was an extrusion temperature of 210 °C, bed temperature of 120 °C, printing speed of 40 mm/s and a layer height of 0.2 mm.

1.8 Objectives

The main objective of this research was to develop printable bioplastics from recycled HDPE and rice husk filler, then establish optimal printing process parameters. This was achieved by addressing the following specific objectives:

i. To develop and characterize bioplastic materials with different ratios of biomass to recycled plastic.
ii. To experimentally investigate the properties of printed parts through tensile tests, compression tests, thermal analysis, and biodegradability tests.

iii. To simulate the printing process of the developed bioplastic materials to determine the suitability for 3D printing and conduct finite element analysis on the printed samples.

iv. To optimize the printing parameters and print a biosensor substrate from the developed bioplastic material.

1.9 Justification of the Study

The development and characterization of filaments from agricultural waste and recycled plastic for fused filament fabrication is a significant step in materials innovation in materials science. It addresses sustainability challenges by reducing waste that negatively impacts the environment, while promoting cost-effective solutions compatible with current 3D printing technologies, thereby enabling circular manufacturing strategies.

By blending recycled polymers with agricultural wastes, such as rice husks, the mechanical, thermal, and physical properties of the resultant biofilaments can be tuned, resulting in customizable material properties. The ability to convert these materials into biofilaments that function effectively in conventional FFF 3D printers enables a wide range of applications, from prototypes to end-use parts. With this new development in novel blends, innovation in material science is encouraged, leading to lighter, stronger, and more sustainable alternatives to conventional filaments like PLA or ABS.

Economically, there is value added when agricultural residues and low-value recycled plastics are converted into high-value filaments. Furthermore, the cost of raw materials is significantly lowered when inputs are derived from waste, making filament production more affordable, especially in low-resource settings. This promotes decentralized production, circular economies, and job creation in developing countries with agricultural waste surpluses.

Environmentally, utilizing agricultural waste and recycled plastics as raw materials in manufacturing helps reduce the large amounts of both synthetic and organic waste that end up in landfills and incinerators. There is a significant reduction in fossil fuel reliance when bioplastics are produced from renewable resources, resulting in lower greenhouse gas emissions compared to conventional plastics. Additionally, biodegradability is significantly enhanced when renewable resources are utilized to produce bioplastics. This is because they degrade more quickly than conventional plastics, thereby reducing their negative environmental impact.

Based on the mechanical and thermal properties of the developed biocomposite, parts can be printed for non-load-bearing biomedical applications, such as casings and microfluidic substrates.

1.10 Thesis Structure

This thesis comprises five main chapters. The first chapter provides an introduction, highlighting the background on bioplastic development, additive manufacturing of biocomposites, the challenges associated with biocomposite applications, the problem statement, objectives, and justification. The second chapter is on the literature review encompassing bioplastic production, characterization methods, previous studies done, process parameters optimization for biocomposites in FFF, and gaps identified. Chapter three outlines the methodologies used to achieve each objective of this research. Chapter four presents the results and their discussions in detail as obtained from simulations and experiments. Lastly, conclusions and recommendations for further work are presented in Chapter five.

CHAPTER TWO

LITERATURE REVIEW

2.1 Overview

This chapter reviews relevant literature supporting the current work. The techniques used to develop biocomposites are elaborated, as are their characterization methods. Optimization techniques for fused filament fabrication process parameters are also discussed and compared. Past studies are also reviewed to identify gaps in these works.

2.2 Theoretical Background

Agricultural waste can be utilized to produce biocomposites, biopolymers, and other value-added products. The use of biopolymers derived from agricultural waste is motivated by environmental concerns stemming from plastic use. Due to their non-biodegradable nature, plastics in the environment cause irreversible harm (Vizureanu et al., 2025). The manufacture of plastics using petrochemical resources releases greenhouse gases that have a detrimental impact on the environment. Moreover, the limited landfill space for plastic disposal and the harmful emissions from plastics incineration have spurred global efforts to develop alternative, sustainable materials (Nida et al., 2020). As a result of all these major concerns, biodegradable plastics have emerged. The development of biobased polymers from naturally existing materials reduces the environmental carbon footprint.

Bioplastics production is still in its early stages, with a contribution of 2.11 MT as of 2019, accounting for about 1% of global plastic production (Heylin, 2019; Niaounakis, 2019). This is expected to reach 2.89 MT by 2025. The slower adoption of bioplastics can mainly be attributed to their weaker mechanical properties and higher production costs compared to traditional plastics. Additionally, other environmental factors to consider when growing plants for bioplastics include food competition and recycling challenges (Ezgi Bezirhan Arikan & Havva Duygu Ozsoy, 2015; Lamberti et al., 2020;

White et al., 2020). The market for bioplastics is projected to grow significantly in the coming years, overtaking petrochemical plastics as the world urgently seeks a sustainable alternative to petroleum-based plastics.

Efforts have been made to improve the mechanical properties of bioplastic materials as a substitute for conventional plastics (Zarna et al., 2021). The most common biopolymers include starch, polylactic acid (PLA), and polyhydroxyalkanoates (PHA). Starch and PLA are mainly used in food packaging. PLA's characteristics, such as being non-toxic, transparent, and water-resistant, make it suitable for food packaging applications (Nida et al., 2020).

Biopolymers derived from renewable resources mimic the properties of traditional polymers such as polyethylene terephthalate (PET), polypropylene (PP), and polyethylene (PE). Biocomposites are biopolymers reinforced with natural or biofiber materials. Bioplastics are plastics that are either biodegradable or bio-derived from renewable natural resources. Biodegradable bioplastics offer disposal options that reduce the amount of plastic waste entering the environment. Conversely, bio-derived bioplastics significantly decrease carbon emissions during the resource extraction phase.

Currently, the biomass used to create bioplastics comes from cellulose or starch components. The chemical composition and structure of a bioplastic determine its biodegradability; a bioplastic that is entirely produced from biomaterials may not be biodegradable (White et al., 2020). Biodegradable composites are created by the combination of two or more decomposable components. Biopolymers are considered biodegradable when microbial scission alters their composition, leading to oxidation, photodegradation, and hydrolysis. The enzymatic action of microbial attack produces inorganic chemicals, carbon dioxide, and methane. Biopolymers derived from agricultural feedstocks are used in packaging as an alternative to plastics, helping to lower environmental pollution.

In addition to packaging, composites made from agricultural materials like rice and wheat husks are also used to make architectural models because of their low density and excellent insulating properties. Natural fibers are being utilized in various green composites to enhance the material's mechanical properties (Gorrepotu et al., 2021). Whereas polymers are non-polar and highly hydrophobic, fibers are polar and hydrophilic by nature. This difference causes poor adhesion between the organic fiber and the synthetic polymer. Therefore, techniques for surface modification, such as the use of coupling agents or coatings, are employed to enhance adhesion between the fibers and the polymer, thereby increasing their strength. The surface modification techniques affect the mechanical properties of the resultant biocomposite (Satyanarayana et al., 2009).

2.3 Techniques for Developing Biocomposites

Four main techniques are used to develop biocomposites. These are: extrusion process, injection molding, compression molding, and pultrusion. Each of these techniques is briefly discussed:

2.3.1 Extrusion Process

In the extrusion process, the three main processes include mixing, compressing, and passing the thermoplastic material through the die. Using this method, fiber-reinforced polymer is extruded, as shown in Figure 2.1A. The extrusion process can be performed using either a single or a twin screw. Extrusion parameters, including temperature, screw speed, screw configuration, feed rate, and cooling temperature, influence the characteristics of the biocomposite. For efficient mixing of the filler in the polymer matrix, the screw speed needs to be high. However, shear heating during mixing can affect the mechanical strength of the biocomposite. To achieve proper mixing and adequate melt viscosity, higher temperatures are required. Care is needed to prevent temperatures from becoming too high, as thermal degradation occurs rapidly. .

2.3.2 Injection Molding

This process heats the thermoplastic polymer till it becomes flowable and mixes with the filler. Using a pump, pressure is applied, and the flow is permitted to pass through the mold (Figure 2.1B). The two main parameters influencing the characteristics of biocomposites from this process are injection pressure and temperature (Gunning et al., 2014).

2.3.3 Compression Molding

In compression molding, sheets are formed by melting and premixing the material. The sheets are pressed together by the given pressure, creating a composite, Figure 2.1 C. However, where complex geometries are to be manufactured, this process has a limitation.

2.3.4 Pultrusion

In the pultrusion process, the biocomposite development is done continuously, Figure 2.1 D. This method involves impregnating fibers in a resin solution before they are fed through a pultrusion die, which pulls the composite out of the rollers while providing constant heat flow (Gurunathan et al., 2015).

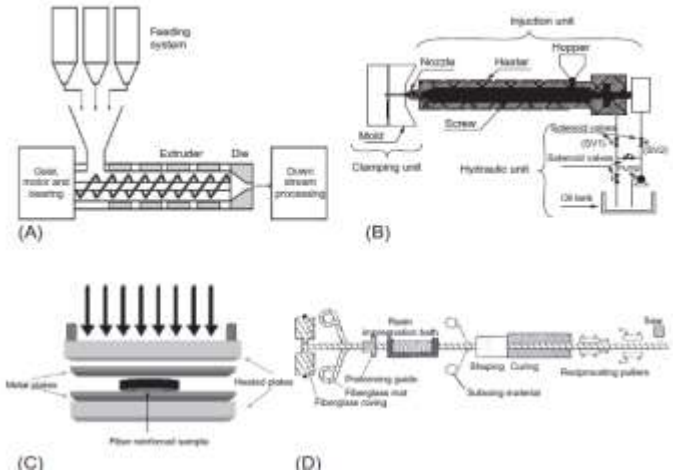

Figure 2.1: (A) The Extrusion Process. (B) The Injection Molding. (C) Compression Molding. (D) Pultrusion Process (Nida et al., 2020)

From the four methods reviewed, the extrusion process is the most appropriate for developing biocomposite filaments from polymers and agricultural fillers.

2.4 Characterization Techniques of 3D Printed Products from Biocomposites

The characteristics of 3D-printed products from biocomposites are influenced by several factors, including resin composition, biomass feedstock properties, and processing techniques. To create 3D-printed items that are competitive and financially viable, it is crucial to conduct a thorough study of their properties and understand how they relate to feedstock and processing variables. This section evaluates the most important properties of 3D printed parts from biocomposites, including physical, mechanical, and thermal properties.

2.4.1 Mechanical Properties of Biocomposite Parts

The most common mechanical properties used to evaluate the performance of 3D-printed parts from biocomposites include tensile properties, Izod impact resistance, and flexural characteristics. Significant changes in mechanical properties have been reported when commercial plastics are substituted with biomass-derived polymers. Recent

developments in printing and biomass modification techniques in the biocomposites enable the improvement of these properties, thus impacting the application of the printed parts (Feng et al., 2017; Nguyen et al., 2018).

Tensile strength and elongation are used to evaluate the mechanical properties of printed parts. The maximum stress a specimen can withstand before breaking or failing is known as its tensile strength, also called its ultimate strength. The ratio of the change in length to the original length during application of tensile force to the specimen is known as tensile elongation, also known as strain (Ma & Suhling, 2009). The equations for engineering stress (σ), Equation 2.1, and engineering strain/elongation (ε), Equation 2.2, are given by (Hertzberg, Richard W and Vinci, Richard P and Hertzberg, 2020):

$$\sigma = \frac{P}{A_0} \tag{2. 1}$$

$$\varepsilon = \frac{l_f - l_0}{l_0} \tag{2. 2}$$

Where: P is the applied load, A_0 is the original cross-sectional area, l_f is the final gauge length and l_0 is the initial gauge length.

Figure 2.2 shows the typical engineering stress-strain curve commonly used to describe the tensile properties of materials. Engineering strain and stress in the elastic region are linear, thus follow Hooke's law, which is given by Equation 2.3:

$$\sigma = E\varepsilon \tag{2. 3}$$

where E is the elastic modulus, also known as Young's modulus, which can be determined from the slope of the engineering stress-strain curve. Hertzberg et al. stated that the interatomic forces between adjacent atoms correspond to the material's modulus of elasticity (Hertzberg et al., 2020).

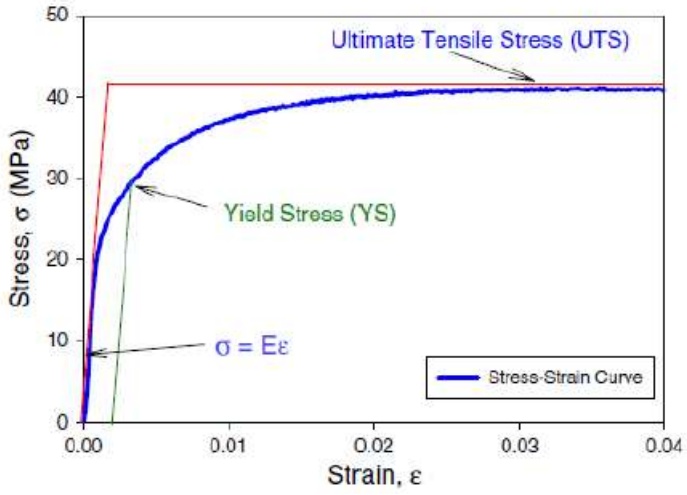

Figure 2.2: Typical Engineering Stress-Strain Curve (Hertzberg et al., 2020)

Studies have been conducted to examine the mechanical characteristics of 3D printed parts. For instance, Rodi et al. conducted a study to characterize biocomposites based on Poly(3-Hydroxybutyrate-co-3-Hydroxyvalerate) (PHBHV) and fibers from Miscanthus Giganteus modified with dicumyl peroxide (DCP) for improved fiber/matrix interface.(Rodi et al., 2018) . The fiber content ranged from 5 to 20 wt.%, and the DCP content was 0, 0.25, and 2.2 wt.%. The mechanical properties tested on FDM-printed samples included tensile modulus, tensile strength, and failure strain, measured using the Instron 5965 Universal Testing Machine in accordance with ASTM D638 standards. It was discovered that the tensile modulus increased from 889 MPa to 1074 MPa with the addition of 5 wt.% raw fibers. The biocomposites with 20 wt.% fibers exhibited a much higher increase in tensile modulus, reaching 1525 MPa.

A lower tensile modulus was observed for biocomposites with a high DCP content than their equivalent counterparts obtained with raw fibers, specifically for biocomposites with 5 wt.% of fibers. This is shown in Figure 2.3. The study attributed the decrease in tensile modulus to the decrease in molar mass when a high DCP content was present. This was verified through further chromatography analysis.

A high percentage of DCP content (2.2 wt.%) ensured that the material did not block during extrusion, thereby achieving a good balance between the crosslinking and grafting processes. For the biocomposite with 20 wt.%, an opposite observation was made, showing a slight increase in tensile modulus, as demonstrated in Figure 2.3. This could be attributed to the high fiber content, which had a positive effect on the mechanical integrity of the biocomposite sample with DCP, thereby reducing molecular chain scission and improving interactions between the fibers and matrix. The study concluded that the composition with 20 wt.% fibers and 2.2 wt.% DCP was the optimal formulation, offering the best mechanical properties.

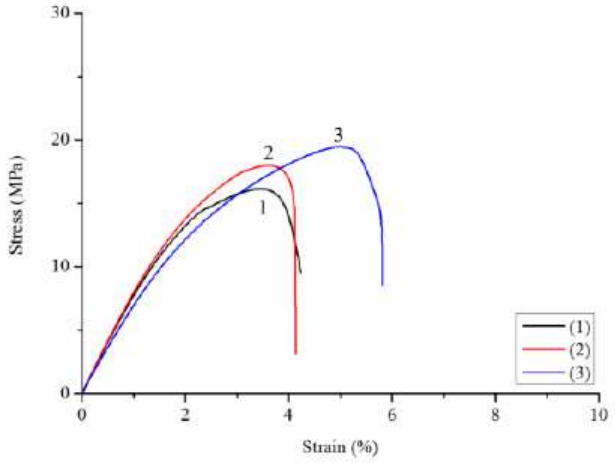

Figure 2.3: Strain-Stress Curves of PHBHV Biocomposites with 5 wt.% Fibre, Sample 1 (0 wt.% DCP), Sample 2 (0.25 wt.% DCP), and Sample 3 (2.2 wt.% DCP) (Rodi Et Al., 2018)

Nguyen et al. used the FFF printing technique to print mixtures of Nylon-12 and organosolv hardwood (HW) lignin (60:40 wt.%) with inclusion of 4 - 16% carbon fibers. They discovered that Young's modulus significantly increased with the addition of carbon fibers, rising to 7500 MPa from 1770 MPa for pure Nylon-12. They concluded that increasing the amount of carbon fibers by 4 to 16 wt.% improved mechanical stiffness and printing efficiency (Nguyen et al., 2018) .

Long et al. developed 3D printing biocomposites from modified bamboo fiber (BF - 20 wt%), polypropylene (PP-52.5 wt. %), and Polylactic Acid (PLA-22.5 wt. %) with maleated polypropylene (MAPP-5 wt. %) as a compatibilizer (Long et al, 2019). Tensile testing was conducted according to GB/T 1040-2006 standards to evaluate the mechanical properties of the biocomposite at a rate of 5 mm/min. The flexural properties of the samples were tested following GB 9341-2008 standard, by bending them at a rate of 5 mm/min. The notch impact test was conducted according to GB 10432008. The tensile, flexural, and impact strength of the biocomposites increased by 13%, 11.7%, and 23.5%, respectively, reaching 33.73 MPa, 47.18 MPa, and 3.15 KJ/m² with 5% MAPP, compared to biocomposites without MAPP. The improvement in mechanical properties was due to the BF modification creating irregular grooves and cracks, which helped the polymer infiltrate the fiber through a strong capillary effect.

According to Bi et al., the addition of 4 wt.% ethylene-propylene-dienemonomer grafted maleic anhydride (EPDM-g-MAH) to wood flour significantly increased the elongation at break from 205.26% to 591.17% in a thermoplastic polyurethane elastomer (TPU)/wood biocomposite. They explained how the esterification between the EPDM-g-MAH and wood flour, which created high interfacial adhesion, likely contributed to the increase in elongation at break. Additionally, the biocomposite's interface interaction can be improved through the physical crosslinking of TPU and EPDM, further enhancing the material's tensile properties (Bi et al., 2018).

Other mechanical properties evaluated for printed parts from biocomposites are Izod impact resistance and flexural properties. To determine the material's toughness, its impact resistance can be measured using an Izod or Charpy impact testing equipment.

2.4.2 Thermal Properties of Biocomposite Parts

Thermal characteristics analyses are crucial in 3D printing, as they influence the intended use of the printed object. Thermoanalytical methods, like thermogravimetric analysis (TGA) and differential scanning calorimetry (DSC), can be used to examine these properties, including melting temperature, glass transition temperature, crystallization temperature, and thermostability.

The inclusion of biomass impacts the thermal characteristics of commercial resins. Therefore, bioplastics have thermal properties that have a significant difference from the original polymer (Nguyen et al., 2018; Tanase-Opedal et al., 2019).

i. Thermogravimetric Analysis (TGA)

Thermogravimetric analysis (TGA) is an analytical method for measuring a material's thermal stability by measuring the mass of the material as a function of temperature and time (International, n.d.). Using a thermogravimetric analyzer, thermal stability, thermal decomposition, composition, and products of the multicomponent system can all be determined from the thermogravimetric curve. Other properties of interest in TGA analysis are oxidation and reduction. The relative thermo-oxidative stability of polymeric materials can be evaluated by comparing TGA decomposition profiles, as seen in (Sai Revanth et al., 2019).

The residual mass of materials at the thermal degradation temperature is revealed by TGA curves. Tanase-Opedal et al. used these curves to evaluate the thermal stability of both PLA and lignin polymers as well as their biocomposites containing PLA/20\% lignin and PLA/40\% lignin. The TGA curve, in Figure 2.4, shows the weight variation of the biocomposites as a function of temperature (Tanase-Opedal et al., 2019).

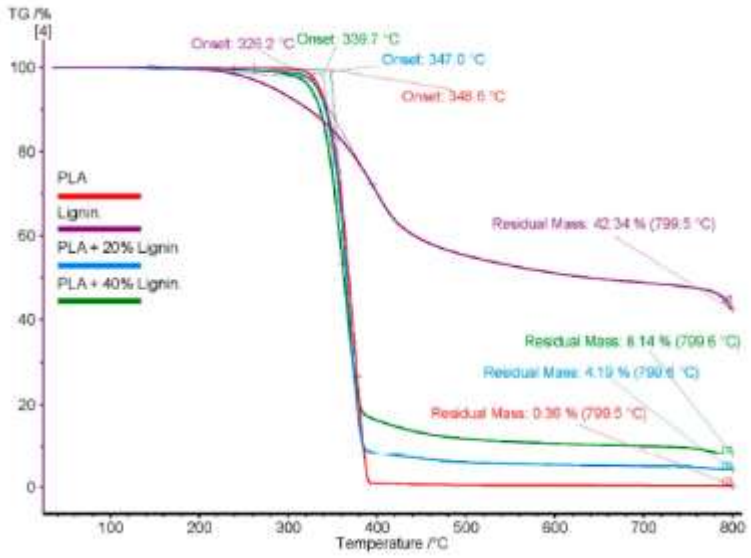

Figure 2.4: Thermogravimetric Analysis Curves of PLA, Lignin, and PLA/Lignin Biocomposites (Tanase-Opedal et al., 2019)

Click or tap here to enter text.Weight loss is indicated by a decreasing TGA thermal curve. The onset temperature is the point at which the temperature begins to decrease, indicating that decomposition has started. As shown by their lower onset temperatures, lignin and biocomposites containing lignin have less thermal stability than PLA.

The general structure of polymers and the alterations of polymer-based products can be studied by examining the degradation products at various temperatures. Low levels of components in printed items can be detected using a thermogravimetric analyzer with a mass spectrometer (TGA/MS). In comparison to TGA/MS, the thermogravimetric analyzer coupled with a gas chromatography mass spectrometer (TGA/GC-MS) may provide a more comprehensive characterization. The GC is used to first separate the gaseous chemicals emitted during thermal decomposition. Then, the MS is used to identify and quantify the compounds. This enables the distinction between overlapping events and the detection of low amounts of components in complex matrices (Boyron, Tiffany, Marre, Alain Delauzun, and Ronan Cozic, 2019).

ii. Differential Scanning Calorimetry Analysis

Schultz et al. characterized biocomposites made of Mycelium, where differential scanning calorimetry (DSC) was used to assess thermal transitions in the material. Endothermic transitions related to water absorption were observed in all samples, along with the softening of lignin. The lignin softening in the biocomposite was directly proportional to the amount of lignin present. The relationship between the enthalpy of water absorption and the sample temperatures was determined (Schultz et al., 2024).

In general, the hotter weather reduced the amount of water absorption, while the humid, colder weather had the reverse effect. Similarly, it was discovered that heat and humidity had a significant impact on lignin softening, causing the lignin chain structure to enter a glassy condition that allows for deformation and stretching.

Other characterization techniques used for biocomposites include:

- Morphological characterization using scanning electron microscopy (SEM)
- Physical characterization e.g., color, density, texture, etc
- Fourier transform infrared (FTIR) spectrometer analysis
- X-ray Fluorescence Spectroscopy analysis
- Hardness testing
- Biodegradation analysis

2.5 Fused Filament Fabrication of Biocomposites

Fused filament fabrication (FFF), also known by the trademark name fused deposition modeling (FDM), is an extrusion-based 3D printing, which is by far the most widely utilized additive manufacturing technology, both in industry and among laymen (Schirmeister et al., 2019). In fused filament fabrication, the process parameters include extrusion temperature, layer height, infill proportion, build orientation, raster angle, and air gap, among others, which are optimized. For a certain output need, some process parameters are more crucial than others. Depending on the application for which a part is

created using FFF, these process parameters must be carefully selected. The best outcomes can only be obtained by identifying and optimizing these crucial process parameters (Suniya and Verma, 2023).

To ensure most manufacturing processes run as efficiently as possible in terms of cost, quality, and time, thorough parameterization is crucial. The process parameters can range from fewer than ten to hundreds. Current methods of optimizing production process parameters require a large number of costly experiments. In some cases, real experiments can be substituted with physically accurate simulation models, such as those based on the Finite Element (FE) method.

Over the years, researchers have examined and utilized a variety of experimental and statistical design of experiments (DOE) methods to optimize the FFF process parameters, thereby improving mechanical properties and part quality. Artificial neural networks (ANN), genetic algorithms (GA), fractional factorial, fuzzy logic, Taguchi method, ANOVA, and other DOE techniques are commonly employed.

2.5.1 Process Parameters of Fused Filament Fabrication

In fused filament fabrication (FFF), the quality of fabricated parts is influenced by several process parameters. The most extensively researched FFF process parameters are as follows:

i) Extrusion temperature: This is the temperature at which the filament material is heated within the nozzle of the printer. This is influenced by the nature of the printing material and the printing speed.
ii) Print Speed: This is the speed of the printing head in the printer's XY plane, typically expressed in millimeters per second. Build time is impacted by print speed. It also has an impact on printed items' strength after a certain point (Dey & Yodo, 2019).

iii) Layer thickness/layer height: This is the thickness of the material of a layer deposited using the FFF technique, Figure 2.5. It influences the part's build time and surface finish. The printing speed, material, and tip size all affect layer thickness (Mohamed et al., 2016).

iv) Bed temperature: This is the temperature of the 3D printer platform upper surface. The temperature of the bed affects how well the initial printed layer adheres to the printing bed. Good adhesive qualities are reported to be provided by a bed temperature that is marginally higher than the printing material's glass transition temperature. To prevent part warping and increase the component's dimensional accuracy, good adhesion is necessary (Spoerk et al., 2018).

Figure 2.5: a. Large Layer Thickness b. Small Layer Thickness (Suniya & Verma, 2023)

v) Build orientation: Parts made using FFF 3D printing are intrinsically anisotropic, meaning that their strength is greater in the XY direction than in the Z direction. The orientation of the part on the print table is referred to as the build orientation, as seen in Figure 2.6. When printing a part with FFF, any orientation is possible. Nonetheless, the build orientation has an impact on the part's strength in various directions, the need for supports during printing, and the surface polish of the part's various surfaces, (Tuan D Ngo et al., 2018).

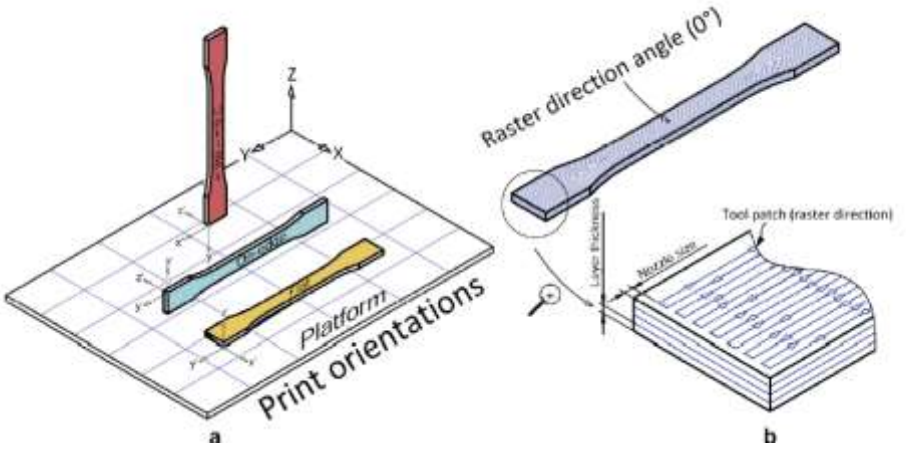

Figure 2.*6*: a. Print Orientations b. Raster Direction Angle at 0°, and Layer Thickness (Chacón et al., 2017)

vi) Raster angle: A layer in an FFF printed object consists of several linear segments of molten metal, called rasters, extruded from the nozzle. The angle from the build table's x-axis at which the printing head deposits a raster of a layer is known as the raster angle, Figure 2.7. Typically, raster angle values range between 0° and 90° in 15° increments. Adjacent layers usually have a 90° difference in raster angles. Raster angle influences the directional mechanical properties of the printed components (Mohamed et al., 2016).

vii) Raster width: This is the width of a raster, also known as a road width, and it depends on the size of the nozzle. The strength of the interior part of the printed part is directly proportional to the raster width (Dey & Yodo, 2019; Mohamed et al., 2016).

viii) Air gap: This is the distance between two adjacent rasters in a layer. The air gap is negative when two neighboring rasters overlap.

ix) Contour width: A series of molten material contours is used to create the outside solid shells of an FFF object. The width of a contour is known as its contour width, Figure 2.7. (Chohan et al., 2020).

x) Contour air gap: The space between two adjacent contours when the part fill style is chosen as multiple contours is known as the contour air gap.

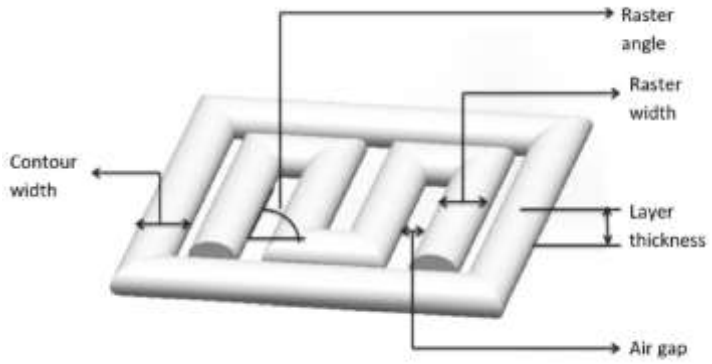

Figure 2.7: Different Process Parameters of FFF (Chohan et al., 2020)

xi) Infill Density: A 3D printed part's internal structure is filled with different types of infills, whereas the part's exterior is typically solid. The percentage of the volume of infill filament material to the overall volume of the part covered by infills is known as the infill density. Generally, pieces used solely for visualization have an infill density of 20%, but end-use parts require a greater infill density to meet the necessary mechanical qualities. An FFF printed part's mechanical strength is significantly influenced by its infill density (Dey & Yodo, 2019).

xii) Infill pattern: The shape and structure of the infill used to fill a part's interior is known as the infill pattern. Figure 2.8 illustrates the different infill patterns. Infill patterns affect a part's printing time and mechanical characteristics (Srinivasan et al., 2020).

In this study, the four main parameters considered were extrusion temperature, bed temperature, printing speed, and layer height, as they have the most significant influence on the results. Other parameters remained constant.

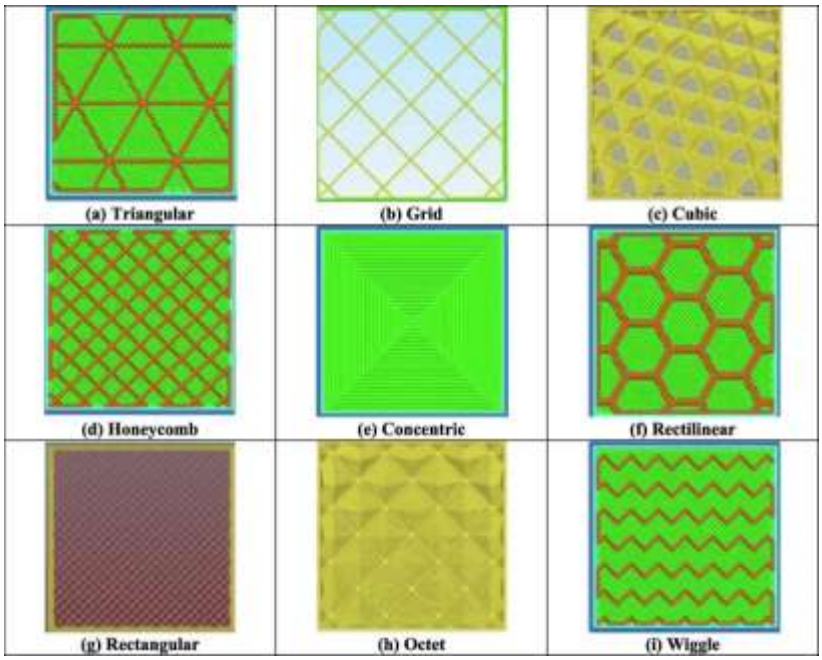

Figure 2.8: Commonly Used Infill Patterns (Srinivasan et al., 2020)

2.5.2 Optimization Techniques Used in Fused Filament Fabrication

The following optimization techniques are used to examine how different process param eters affect the quality and intended characteristics of FFF printed parts:

i) **Genetic Algorithm** – The genetic algorithm (GA) offers a global optimization solution for optimization problems with any kind of constraint (Goldberg, 1989). The technique is population-based and stochastic, searching randomly through population crossover and mutation. The algorithm begins by generating an initial population of solutions, which is thereafter subjected to frequent modifications using crossover and mutation operators, Figure 2.9. Every stage involves the genetic algorithm choosing members of the existing population to become parents and using them to create offspring for the following generation. A fitness function assesses the fitness of individual solutions (Potočnik et al., 2024). With time, the population evolves toward an optimal solution over successive generations. GA-based

techniques have been used to address several AM challenges (Jin et al., 2020; Liu et al., 2020; Vaissier et al., 2019).

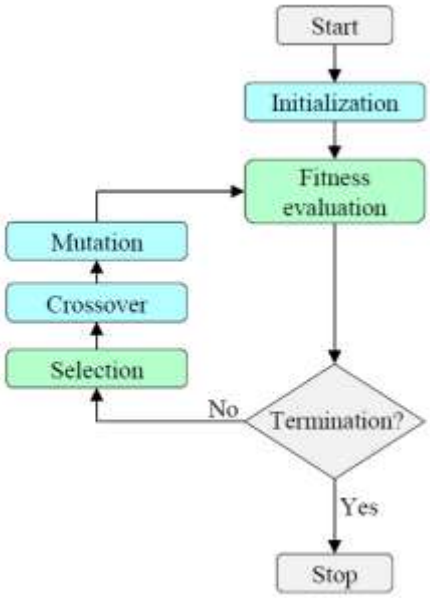

Figure 2.9: The Genetic Algorithm Process Flow

ii) **Grey relational analysis –** Several researchers have used grey relational analysis to identify the optimal set of process parameters to attain the intended performance metrics. Normalization is the initial step in preprocessing experimental data for Grey relational analysis. The Grey Relational coefficient is calculated using the normalized data from each experimental run. The grey relational coefficient for each sequence is averaged to determine the grey relation grade. The optimal process parameter setting for the intended performance parameters is provided by a highest grey relational grade (Kanchana et al., 2019).

iii) **Taguchi Methodology -** The Taguchi method is an experimental design technique used for high-quality system design and process optimization studies. Such a technique can provide process precision and consistency while reducing the overall number of experiments. It is a factorial approach that assigns the factors chosen for an experiment (i.e., variables) using the orthogonal array, which is a sequence of experiments conducted in different situations (Okolie et al., 2021).

The Taguchi method is a systematic optimization technique that is relatively simple and efficient. The Taguchi technique states that product or process optimization should be carried out in three steps, which include system, parameters, and tolerance design, Figure 2.10.

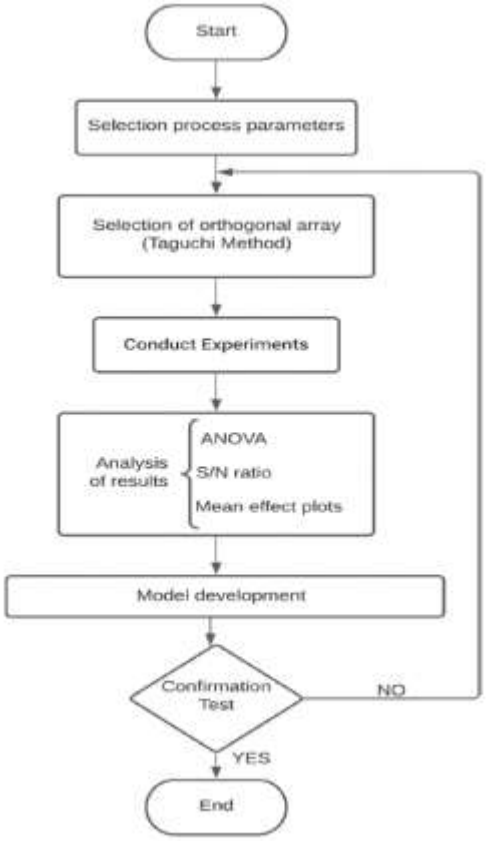

Figure 2.10: Steps in Implementing the Taguchi Method of Optimization (Shakeri et al., 2021)

It suggests using a loss function, which is subsequently converted into a signal-to-noise (S/N) ratio, to measure the deviation between the desired and experimental values. The S/N ratio is the average response value divided by its standard deviation and is used to determine the level of each parameter that could optimize the response. Three types of performance characteristics lower-the-better, higher-the-better, and nominal-the-better are inherent in the S/N ratio analysis.

By utilizing analysis of variance (ANOVA), the statistically significant variables are often evaluated. Therefore, by combining a Taguchi design with an ANOVA study, the best conditions for a process could be found (Ghosh et al., 2017). In FFF, Taguchi method has been widely used in improving mechanical properties and parts qualities (Hasanzadeh et al., 2023; Rabinowitz et al., 2023; Shakeri et al., 2021).

iv) Response Surface Method (RSM)

Response surface methodology (RSM) involves optimizing factorial variable settings so that the response approaches a specific minimum or maximum value. ANOVA and factorial approaches are used to describe the response; however, they are expanded for more detailed effect modeling. Based on the outcomes of factorial studies (screening, followed by three-level factorial), RSM is a sort of augmentation in which additional treatments are added to concentrate the effects and enhance the model's predictive ability. The extra treatments are situated both outward (star points) and within the factorial space (central point). This structure is referred to as a central composite design (Mamdouh El-Bakry and Bhavbhuti M. Mehta, 2022). Response surface methodology has been used as an optimization technique in Fused Filament Fabrication by various researchers, such as (Kandananond, 2020; Vanaei et al., 2022).

v) Artificial Neural Network (ANN)

The concept behind artificial neural networks (ANNs) is modeled after the human brain and how it uses connections between neurons and their relative strengths to process and store information. In this context, a neural network can be defined as a group of interconnected neurons, with the network's architecture determined by the number of layers (depth) and neurons per layer (width).

Each input is connected to the neuron itself by multiplying it by a weight. These weights are established using application-specific data during neural network training. An activation function then receives the data, modifies the input using non-linear functions,

and sends the output to the subsequent neuron (Oehlmann et al., 2021). A basic artificial neural network (ANN) typically consists of a minimum of three layers, as seen in Figure 2.11.

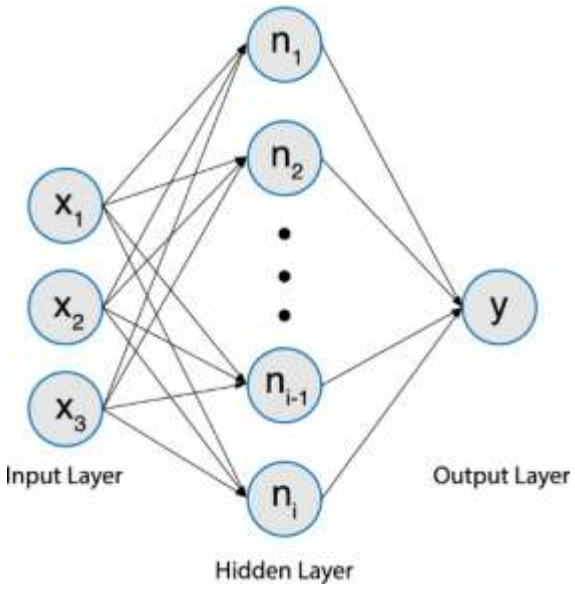

Figure 2.11: Basic Architecture of an Artificial Neural Network (Jörg Frochte, 2020)

Using experimental data sets, an artificial neural network can effectively illustrate non-linear and interaction effects, making it useful in optimization. This optimization technique has been utilized in FFF by (Oehlmann et al., 2021; Pazhamannil et al., 2021; Teharia et al., 2022).

vi) Particle Swarm Optimization (PSO)

Initially introduced by Kennedy and Eberhart, PSO is a swarm-based stochastic algorithm that is based on animal social behavior principles such as fish schooling and bird flocking. PSO views every possible solution to a problem as a particle traveling through space at a specific speed, similar to a flock of birds. Each particle then determines its next move through the search space by combining, with a few random disturbances, some component of the record of its own historical best location and present location with that of one or more swarm agents.

After every particle has been shifted, the subsequent iteration starts. As a whole, the swarm (such as a flock of birds looking for food) is likely to progressively get closer to the objective function optimum. In recent years, PSO has become very popular among researchers and has proved to perform well in a variety of application areas, such as additive manufacturing, and can specialize, hybridize, and exhibit some interesting emergent behaviors. One of PSO's primary benefits is that it requires fewer tuning parameters. PSO achieves the optimal solution through particle interaction by slowly converges to the global optimum through a high-dimensional search space (Gad, 2022). In FFF, PSO has also been applied as an optimization technique by (Shieh Em & Chee Kiong, 2023; Shirmohammadi et al., 2021).

Other optimization techniques used are in FFF are the Factorial Design Method (Rashed et al., 2022)and Teaching Learning Based Optimization (TLBO) (Alam et al., 2021; Rao & Rai, 2016).

As for the performance parameters, the following have been used:

- Mechanical properties, e.g., tensile strength, flexural strength, and compressive strength
- Dimensional accuracy / Warpage
- Surface roughness/surface finish
- Printing and building time
- Specific printing energy

Table 2.1 summarizes some research on optimizing FFF process parameters using various optimization techniques.

Table 2.1: A Summary of Research on the Optimization of FFF Process Parameters

Authors	Material	Optimization Technique	Process Parameters	Performance Parameters
(Sharma et al., 2020)	PLA	Taguchi Optimization Technique	• Printing speed • Layer thickness • Infill density	Surface roughness
(Ngo et al., 2018)	ABS	Response Surface Method	• Extrusion temperature • Infill density • First layer thickness • Other layer thickness	Warpage
(Sood et al., 2012)	ABS	Taguchi (L27) and Grey Rational Method	• Build Orientation • Layer thickness • Raster angle • Raster width • Air gap	Dimensional Accuracy
(Shieh Em & Chee Kiong, 2023)	PLA	Particle Swarm Optimization (PSO)	• Print temperature • Print speed • Layer thickness • Infill percentage	Dimensional Accuracy
(Rao & Rai, 2016)	N/A	Teaching-learning-based optimization (TLBO)	• Layer thickness • Build orientation • Raster angle • Raster width • Air gap	Pareto optimal set of solutions

2.6 Previous Research on Biocomposites from HDPE and Rice Husks

Biocomposites made from recycled high-density polyethylene (rHDPE) have been studied by several researchers. Chen et al. developed and tested biocomposites from

recycled high-density polyethylene (rHDPE) and recycled polyethylene terephthalate (rPET), reinforced with rice husk flour (RHF) at loadings ranging from 30 to 70 wt. %. These biocomposites were produced using extrusion, while the samples were fabricated through hot and cold pressing. The study focused on examining how RHF content affects the physical, mechanical, morphological, and thermal properties of the composites (Chen et al., 2015).

Regarding physical properties, higher RHF content led to increased water absorption, diffusion coefficient, solubility, and permeability, due to greater hydrophilicity and microstructural voids. In terms of mechanical properties, tensile strength increased, peaking at 30 wt. % RHF, then declined at higher loadings due to poor dispersion and fiber agglomeration. Tensile modulus showed a significant increase (up to 172%) with higher RHF content, while flexural strength remained stable. Impact strength decreased as RHF content increased, attributed to increased brittleness and inadequate fiber dispersion at higher loadings. at high loadings (Chen et al., 2015).

Azam et al. investigated the effects of rice husk (RH) filler content and surface treatments on the mechanical properties and morphology of porous recycled high-density polyethylene (rHDPE) biocomposite foams. Their goal was to develop lightweight, cost-effective, and eco-friendly materials. The filler content was varied from 10 – 50 wt. % with maleic anhydride-grafted polyethylene (MAPE) used as a coupling agent, and azodicarbonamide (ADC) as a chemical blowing agent. To improve the interfacial adhesion, UV/O_3, alkali, and acid treatments were applied. Composite foams were created through extrusion, internal mixing, and hot pressing. Thereafter, the composite foams were characterized to determine morphology, mechanical properties, and foam structure analysis. Results indicated the best foam structure was achieved at 50 wt. % RH with the smallest cell size of approximately 58 μm and the highest cell density of 7.62×10^{11} cells / cm^3. Increasing RH content improved cell uniformity and density due to enhanced nucleation, but also increased viscosity, restricting foam expansion (Azam et al., 2020).

Alkali-treated RH gave the highest tensile strength (10.83 MPa) and Young's modulus (858 MPa), whereas UV/O_3 treatment improved tensile strength by approximately 20.5% over untreated RH, showing promise as an eco-friendly alternative. On the flexural strength, chemical treatments had minimal effect, with all samples showing similar values of approximately 28 – 30 MPa, whereas UV/O_3-treated samples performed worse due to the microcellular structure impacting stress transmission. Alkali and acid treatments significantly improved impact resistance. UV/O_3 treatment had minimal benefit, potentially due to microcrack formation from weak fiber–matrix interaction. The morphological analysis demonstrated that surface treatments improved RH–polymer bonding and foam uniformity. Alkali treatment caused high viscosity and a denser, more compact structure, boosting strength but distorting foam morphology. Their study demonstrated that fiber content, foam morphology, and surface treatment all significantly influence the performance of RH/rHDPE composite foams.

Rahman et al. investigated how the size and loading percentage of rice husk (RH) filler affect the processability and impact strength of bio-composites made from recycled high-density polyethylene (rHDPE). They tested for thermal stability using a TGA, impact strength using the Gardner impact test, rheological behavior using the melt flow index (MFI), and apparent viscosity. From their findings, larger RH particles (size A) showed the highest thermal stability, whereas finer RH (size D) degraded more easily due to higher surface area and hemicellulose content. This made size A more suitable for high-temperature processing like injection molding. The melt flow rate (MFR) decreased with increasing RH content. Composites with finer RH (sizes C & D) initially flowed better at 30% content but showed poor thermal stability and agglomeration at higher loadings. An MFR > 4 g/10 min was deemed necessary for good injection molding processability. As for the impact strength, it decreased with smaller filler size (C, D) and higher filler content (40 – 50%). RH size A at 30% loading (RH30PEA) had the highest impact resistance due to better filler-matrix bonding and dispersion. From their study, it was concluded that RH Size A (250 – 500 μm) at 30% weight was optimal as it resulted

in the best thermal stability, good melt flow rate, and highest impact strength (Rahman et al., 2010) .

Shah et al. explored how incorporating rice husk biochar into recycled HDPE (rHDPE) affected its mechanical, thermal, and fire-retardant properties. Using a high-speed mixer and a manual injection molding machine, composites were made from rHDPE with 10%, 20%, 30%, and 40% rice husk biochar (labeled C10 to C40). Characterization tests conducted included tensile, flexural, and impact tests for the mechanical properties, and thermogravimetric analysis (TGA/DTG) for thermal properties. Fire retardant test was conducted using horizontal and vertical burning tests (UL-94) with limited oxygen index (LOI), and cone calorimetry (Shah et al., 2023).

Lastly, structural analysis was performed using FTIR and SEM. The best mechanical properties were exhibited by the 30% biochar (C30), with increases of 24% in tensile strength, 19% in flexural strength, 34% in tensile modulus, and 80% in flexural modulus. Impact strength decreased with biochar content due to increased rigidity. Maximum impact strength was observed at 20–30% loading, decreasing by 22.5% at 40%. Thermal stability improved with higher biochar content, with the onset degradation temperature rising from 425°C (rHDPE) to 442°C (C40). Fire retardancy improved significantly with 40% biochar (C40). Structurally, no new chemical bonds were formed; only physical bonding. Morphology analysis showed good filler dispersion at 30% loading (C30), but particle agglomeration occurred at 40% (C40), explaining the drop in mechanical properties beyond 30%. Their study showed rice husk biochar is a sustainable, effective additive for enhancing recycled plastics. The best mechanical performance was exhibited by 30% biochar (C30), whereas thermal stability and fire retardancy were optimal with the 40% biochar (C40) (Shah et al., 2023).

2.7 Summary of the Research Gaps

The following gaps were identified in the literature review:

i) Most of the fabrication processes done using composites of HDPE have included molding, extrusion, internal mixing, and hot pressing. There is limited work done on the Fused Filament Fabrication process of HDPE and its composites. This is due to challenges encountered when printing HDPE, such as adhesion to the print bed, high thermal shrinkage, and subsequent warpage.
ii) In the characterization of the new HDPE composites, thermal, mechanical, and morphological characterization have been done. Biodegradability testing has not been a common characterization technique due to challenges in accessing equipment for this test. This current study uses a different technique in determining changes in the biodegradability of biocomposites of recycled HDPE.
iii) While the most popular polymers, such as PLA and ABS, have been optimized, little study has been done on improving the FFF process parameters for HDPE manufacturing. 3D printing simulation softwares such as Simufact Additive, Digimat-AM, ANSYS Additive Print, and Flow-3D AM have not included HDPE material files in modeling the printing behaviour of HDPE. There is thus need for scientific study to develop a methodology for modelling material files for HDPE to be used for simulation, which can predict its behavior during printing and improve its performance.

In this study, all the gaps mentioned will be addressed. Biofilaments are developed from recycled HDPE and rice husk waste filler in various proportions. The biofilaments are tested for printability to determine the highest content of rice husk / rHDPE biofilament that can be printed. Characterization of the biocomposites is done, and then modelling of the material file using the experimental properties to be used for simulation and the determination of optimal printing process parameters.

CHAPTER THREE

METHODOLOGY

3.1 Overview

The methodology presented in this work is based on the objectives presented in Chapter Two of this thesis. This work's first objective involved the development of biofilaments from recycled HDPE and rice husk filler in various ratios. The biofilaments developed were tested for printability to determine the maximum rice husk filler ratio that could be printed using the Fused Filament Fabrication (FFF) process. The second objective was to characterize the biofilaments to identify their physical, mechanical, thermal, morphological, and biodegradability properties. The third objective involved simulating the developed biofilaments to assess their suitability for the FFF process by predicting warpage and residual stresses. This involved building a coupled simulation of the FFF process and a Finite Element Analysis to predict the part performance. The fourth objective entailed the optimization of the printing process from simulation, followed by validation of the printing setup. Lastly, from the findings of this work, a biosensor microchip substrate was fabricated from the developed bioplastic with the highest ratio of rice husk filler. A biosensor microchip is selected as one of the applications for the biocomposite developed, since its mechanical property requirements match those of the material. That is, low mechanical strength of approximately 8 MPa, as it is a non-load-bearing device. The biocomposite also offers improved biodegradability, enhanced stiffness, and lower costs compared to pure HDPE. Its low water absorption capabilities further makes it durable, hence suitable for biomedical casing such as that of the biosensor microchip and the breath analyzer.

3.2 Development of Bioplastics

In the development of the biofilaments, the filament extrusion process was used. Different ratios of the recycled HDPE to the rice husk filler were investigated to

determine the highest percentage of the filler that could be incorporated to the biofilament and printed with consistent material extrusion. For successful printing, the filament diameter had to be consistent at 1.75 ± 0.05 mm.

3.2.1 Materials for the Bioplastic Development

The main ingredients used in the bioplastic development were recycled HDPE, rice husk filler, and maleic anhydride functionalized polyethylene (MAPE). Recycled HDPE pellets were supplied by Mr. Green Africa (Nairobi, Kenya). The properties of the rHDPE are presented in Table 3.1. The compatibilizer, MAPE, was provided by Fine-Blend Polymer Company (Shanghai, China). It acts as a macromolecule coupling agent for polyethylene-based composites reinforced with natural fillers. Its properties are shown in Table 3.2.

Table 3.1: Properties of rHDPE

Property	**Value**
Average length	3.09 mm
Average diameter	4.46 mm
Humidity	0.045%
Melt Flow Rate	1.6 g/10min (with 5kg weight at 190℃)
Melting Enthalpy	176 J/g
Tensile Modulus	715 MPa
Tensile Strength	23.5 MPa
Tensile Strain at Break	629 %
Charpy Notched Impact Strength	20.6 KJ/m^2

Table 3.2: Properties of MAPE

Property	Value
Density	0.945 ± 0.005 g/cm^3
Melt Flow Rate	1.0 - 5.0 g/10 min (with 2.16kg at 190℃)
Volatiles	< 0.3 wt. %
Processing temperatures	150℃ to 300℃

Rice husk waste was supplied by Mwea Rice Mills Ltd (Kerugoya, Kenya). It had a bulk density of 0.45 g/cm^3.

3.2.2 Biofilament Fabrication

The rice husk waste was first ball-milled into a powder, then sieved to obtain particles less than 75 μm, the smallest achievable. According to literature and preliminary experiments, a finer particle size is preferred to reduce extrusion challenges, such as clogging of nozzles during printing (Ondiek et al., 2018). The rHDPE pellets were shredded using a plastic shredder to further decrease their size for proper mixing with the rice husk filler. A Camsizer XT by Retsch GmbH, Germany was used to analyze the cumulative distribution density, aspect ratio, and sphericity of the milled rice husks. Before mixing the ingredients, rHDPE and RH filler were oven-dried at 80 °C for 24 hours to remove any moisture in the materials. These drying conditions are based on similar studies, including those by (Cestari et al., 2013; Koffi et al., 2022). Then, the ingredients were combined in various proportions based on the compositions listed in Table 3.3.

Table 3.3: Different Compositions of the Bioplastic

Composition	Rice husk filler (%)	Recycled HDPE (%)	MAPE (%)
1	0	100	0
2	5	95	0
3	10	90	0
4	15	85	0
5	20	75	5
6	25	45	30
7	30	40	30
8	35	35	30

The bioplastic compositions were determined experimentally. The percentage of rice husk filler was increased from 0% to 35 % in steps of 5% to determine the highest percentage that could be added to the bioplastic composition without compromising the biofilament extrusion. For bioplastic compositions containing more than 15% rice husk filler, maleic anhydride functionalized polyethylene (MAPE), a compatibilizer, had to be added. This was due to the difficulty in extrusion of the material at this point hence the MAPE worked to promote adhesion between the inorganic polyethylene and the organic rice husk filler. The maximum allowable percentage for the MAPE in the bioplastic synthesis was 30% according to the guidance from the manufacturer (Fredi & Dorigato, 2023). After mixing the ingredients, the SJ35 single-screw filament extrusion system (Zhangjiagang, China) was utilized to create the biofilaments.

The biofilament extrusion became difficult, as seen from the nozzle clogging, beyond 35 % of the RH filler addition regardless of the use of the compatibilizer. The determination of the biofilament composition was done according to studies done by (Cestari et al., 2013; Lamm et al., 2020; Tran et al., 2017).

The filament extrusion system had a three-stage process that included a heating system for melting the ingredients, a water-cooled system for cooling the extruded biofilaments, and a spooling system for winding the cooled biofilament in preparation for three-dimensional printing. The extrusion system is shown in Figure 3.1. The four main process parameters identified in the filament fabrication process were: barrel temperature, denoted as heater 1; nozzle temperature, denoted as heater 2; extrusion speed, also known as screw speed; and spooling speed, also known as roller speed. The barrel temperature is the initial point of contact of the pellets with the heaters. This is where the heating starts and melting occurs. At the nozzle temperature, the temperature is higher than at the barrel to ensure that complete melting of the pellets occurs. Normal tap water maintained at room temperature was used for cooling the extruded biofilaments. Using the Taguchi design of experiments, the filament fabrication was optimized. Table 3.4 lists the extrusion process parameters studied and their levels.

Table 3.4: Extrusion Process Parameters and their Levels

Process parameter	**Level 1**	**Level 2**	**Level 3**
Heater 1 temperature ℃	150	160	170
Heater 2 temperature ℃	160	170	180
Screw speed (min^{-1})	18	19	20
Roller speed (min^{-1})	300	350	400

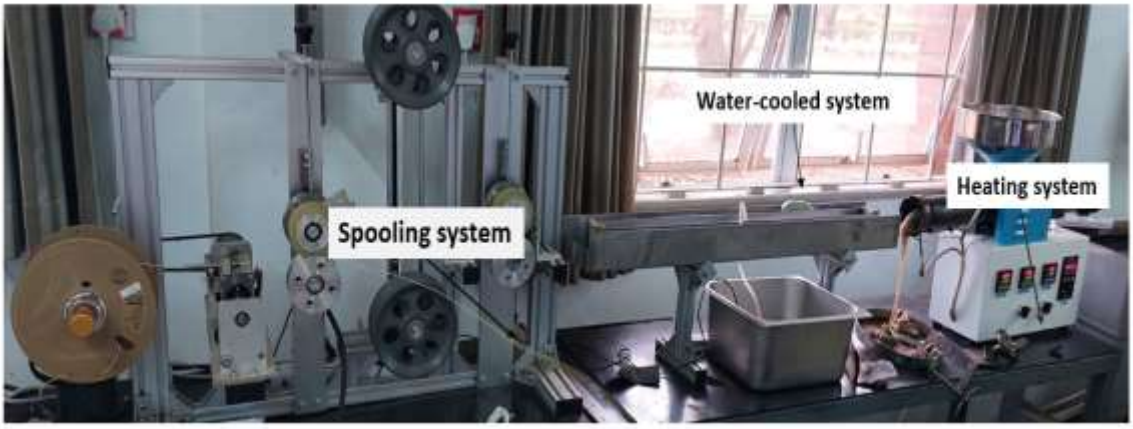

Figure 3.1: The SJ35 Single-Screw Filament Extrusion System

To minimize the number of experimental runs, the Taguchi L_9 was selected for this optimization. The experimental design is presented in Table 3.5. The desired response was a filament diameter of 1.75 mm ± 0.05 mm.

Table 3.5: L_9 Taguchi Experimental Design

Experiment	Heater 1 temp. °C	Heater 2 temp. °C	Screw speed (min^{-1})	Roller speed (min^{-1})
1	150	160	18	300
2	150	170	19	350
3	150	180	20	400
4	160	160	19	400
5	160	170	20	300
6	160	180	18	350
7	170	160	20	350
8	170	170	18	400
9	170	180	19	300

3.3 Bioplastic Characterization

The developed bioplastic was evaluated in accordance with international standards to assess its properties. The following properties were evaluated:

- Printability
- Mechanical properties
- Thermal properties
- Morphological analysis
- Surface roughness analysis
- Biodegradability analysis
- Chemical composition analysis

3.3.1 Fused Filament Fabrication (FFF) of the Developed Bioplastics

The printability of the developed biofilaments was evaluated using FFF 3D printing. The Prusa i3 MK3S+ (Prusa Research, Czech Republic) was used for this purpose, Figure 3.2. The printed samples were prepared for tensile, compression, and flexural tests. Table 3.6 provides the printing parameters for the biofilaments. These parameters were achieved through experimental investigation of printing with the developed bioplastics. A 0.4 mm nozzle diameter was effective for printing biofilaments with rice husk filler up to 10 wt.%. For higher percentages, such as over 15 wt.%, a 0.6 mm nozzle was used to prevent clogging. Printability was measured by consistency in material extrusion during printing and complete prints whose final dimensions matched the ones in the CAD designs.

For printing HPDE materials, adhesion to the print bed is always an issue. To tackle this challenge, the print bed was modified from a steel print sheet to a polypropylene (PP) print bed. When printing with HDPE or PP, a polypropylene (PP) print sheet should be placed on the 3D printer bed, as both materials have a similar semi-crystalline chemical structure that provides the adhesion required to prevent excessive warping.

Table 3.6: Printing Parameters for the Biofilaments

Parameter	Value
Nozzle diameter	0.4 – 0.6 mm
Nozzle temperature	210 – 240 ℃
Build plate temperature 1st layer	70 ℃
Build plate temperature	40 ℃
Layer thickness	0.2 mm
Infill density	100 %
Infill pattern	Rectilinear
Printing speed	45 mm/s
Fan cooling	100 %
Angle of filing pattern relative to extrusion direction	45 o

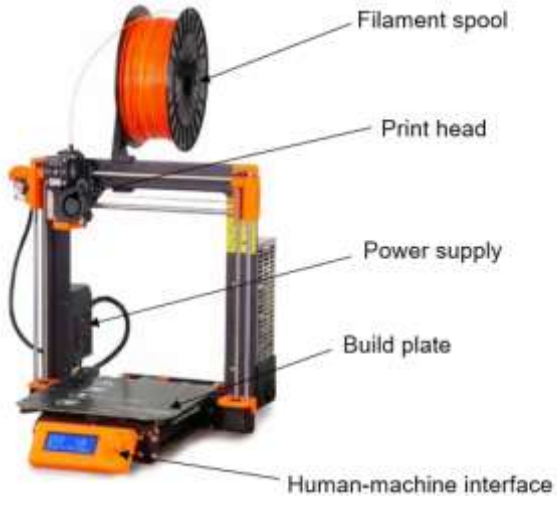

Figure 3.2: Prusa i3 MK3S+

3.3.2 Mechanical Characterization of the Developed Bioplastics

Mechanical characterization was conducted to determine the tensile, compressive, and bending/flexural properties of the developed bioplastics. The universal testing machine AGS-X series (Shimadzu Corporation, Japan) was utilized. For these tests, three samples were 3D-printed following the American Society for Testing and Materials (ASTM) standards. Tensile testing was done according to ASTM D638 standard, compression testing was done according to the ASTM D695 standard, and the flexural/bending test was done according to ASTM D790 standard for the three-point bending test. The experimental setup is presented in Figure 3.3.

The loading condition for the tensile testing was 10 mm/sec, whereas compression and flexural tests were done at a loading condition of 5 mm/min.

The tensile testing expressed in terms of mechanical strength or stress, σ, is given by force, *F,* per unit area, A, Equation 3.1, and strain, ε, is given by the change in length, ΔL, of the loaded sample divided by the original sample length, L, Equation 3.2.

$$\sigma = \frac{F}{A} \qquad (3.1)$$

$$\varepsilon = \frac{\Delta L}{L} \qquad (3.2)$$

For the tensile testing of the biofilaments, the force measurements were divided by the sample's cross-sectional area. Strain was determined by dividing the change in length (or extension) by the initial length of the sample. These values were then presented on an X-Y plot known as a stress-strain curve.

Equation 3.3 is for the determination of the three-point flexural strength, σ, which is:

$$\sigma = \frac{3 * F * L}{2 * w * d^2} \quad .. \quad (3.3)$$

Where σ is the flexural strength, *F,* is the loading force, *L,* is the sample length, *w,* is the sample width, and *d,* is the sample thickness.

The maximum flexural strain, ε, occurs at the mid-span and is calculated using Equation (3.4):

$$\varepsilon = \frac{6 * \delta * d}{L^2} \quad (3.4)$$

Where ε is the maximum flexural strain at the outer surface in mm/mm, hence dimensionless, δ is the mid-span deflection, *L* is the sample length, and *d* is the sample thickness.

The flexural modulus, *E,* is the slope of the linear elastic line and is given in Equation (3.5):

$$E = \frac{\Delta \sigma}{\Delta \varepsilon} \quad (3.5)$$

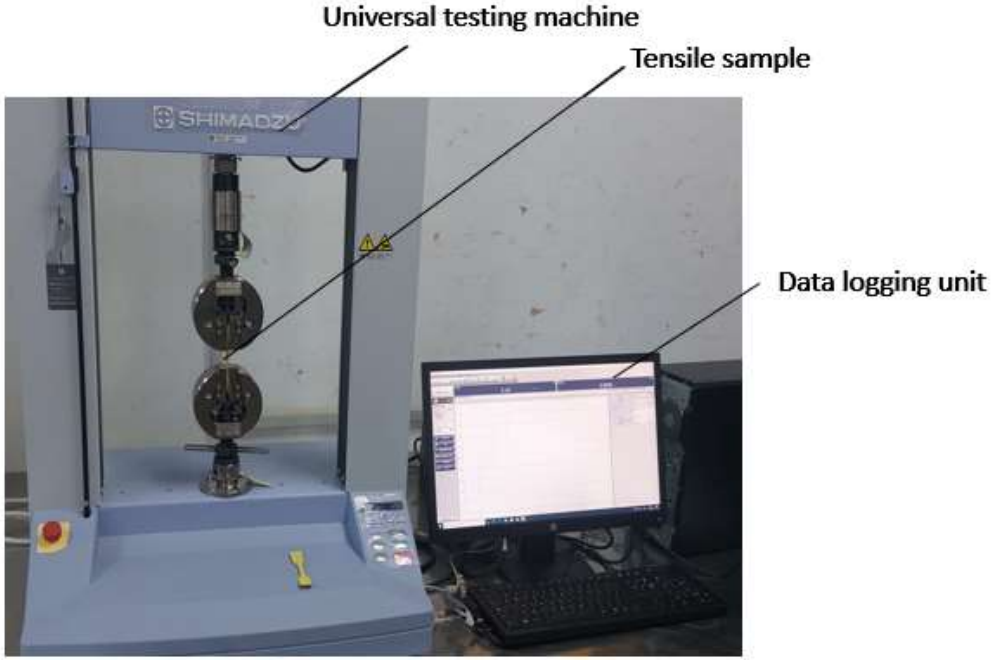

Figure 3.3: Experimental Set-Up of the Tensile Test

3.3.3 Thermal Properties

Thermal analysis was conducted to determine the bioplastics' melting temperatures, crystallinity, glass transition temperatures, and enthalpy. This was done using the differential scanning calorimetry, DSC (Mettler Toledo, United States of America), in accordance with the ASTM E1952 standard. The samples were prepared from the biofilaments by cutting cross-sections with a sharp surgical blade to a mass of 2.00 mg-5.00 mg. They were then placed inside aluminum sample pans, sealed, and put in the DSC for testing. In the DSC, the samples were heated in a nitrogen atmosphere at 10 °C/min to 170 °C, then cooled to 50 °C at the same rate. The Star e-DB V.17 software was used to study the behavior of materials as a function of temperature or time.

3.3.4 Morphological Analysis of the Developed Bioplastics

The morphology was conducted to determine RH filler dispersion within the matrix of the rHDPE and check for porosity. This was done using the Neoscope™ Scanning

Electron Microscope, SEM, (Japan Electron Optics Laboratory, Japan) at an acceleration voltage of 15 kV.

3.3.5 Surface Roughness Analysis of the Developed Bioplastics

Three surface roughness characteristics of the produced biofilaments were measured using the MarSurf PS10 surface roughness tester (Mahr GmbH, Germany). These included mean roughness depth (Rz), roughness average (Ra), and root mean square roughness (Rq). The European standard DIN EN ISO 4287 was followed for taking the measurements.

3.3.6 Biodegradability Analysis of the Developed Bioplastics

Biodegradability analysis was performed according to the methodology presented in (Moscicki, 2009) where the change in mass of the sample is used as the measurement index. This methodology was done according to the ASTM D5988-18 and ISO 17556: 2019 standards for analyzing the biodegradability of plastics in soil. Tensile test samples were used for this analysis, similar to those used for mechanical characterization. The samples were dried to a moisture level not exceeding 4% then placed in special porous baskets and placed in a plastic container to a depth of 15 cm. These were then covered with red soil acquired from a farm in Kahawa Sukari, Kenya. The soil had a pH of 6.5. The soil humidity had to be maintained at 70% by supplementing water loss at least twice a week. The plastic container was stored in an environment having relatively stable temperature and humidity. This was analyzed for a period of 24 weeks which were divided as 2, 4, 8, 12, 16, 20 and 24 weeks. The schematic is illustrated in Figure 3.4.

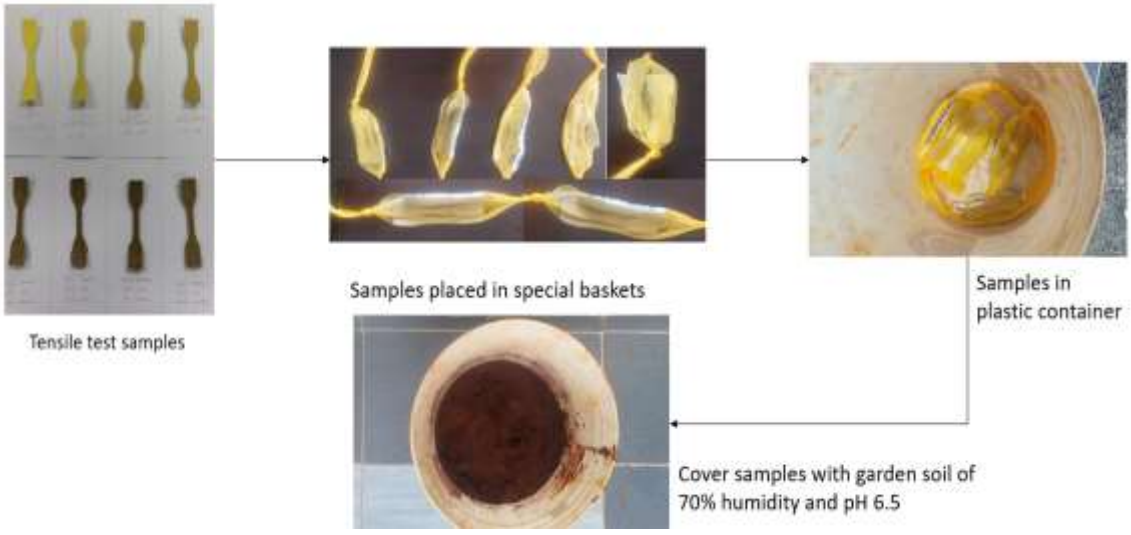

Figure 3.4: Experimental Set-Up for Biodegradability Analysis

During each period of analysis, the samples were cleaned, weighed, and dried to their original humidity of less than 4%. Finally, the samples were weighed on a digital scale to determine the final mass loss, Equation (3.6):

$$\%\ mass\ loss = \frac{m_f - m_i}{m_f}\ x\ 100\ \% \qquad (3.6)$$

Where m_f is the final mass of the sample at week 24, m_i is the initial mass of the sample at the onset of the test. The biodegradability was then related to the change in tensile strength by testing the samples for tensile strength. Additionally, the biodegradability was related to the initial moisture content of the samples, as measured using the DAB 200–2 (Kern & Sohn GmbH, Germany) moisture analyzer. This was done by measuring 3 g of the biofilament and analyzing for moisture at a temperature of 80°C.

3.3.7 Chemical Composition Analysis of the Developed Bioplastics

A Fourier transform infrared (FTIR) analysis was performed to investigate the chemical interaction between the RH filler, rHDPE, and MAPE in the resultant biofilaments. For this purpose, the Bruker Alpha II Fourier Transform Infrared Spectrometer (Portable Spectral Services, China) was used. The scanning range was varied from 4000 cm^{-1} to 400 cm^{-1} with a scanning resolution of 4 cm^{-1} and a scan time of 24 scans per sample.

3.4 Simulation of the Printing Process

The third objective involved simulating the printing process using the developed bioplastic to determine its suitability for the FFF printing process. Finite element analysis was also conducted to predict part performance, accounting for the manufacturing process. Digimat 2024.1 software was used for multiscale material modeling in both simulations. The software comprises several modules, as illustrated in Appendix C.

This study focused on the development of bioplastic materials from rHDPE and RH filler; hence, the material was not available in the Digimat MX database. This, therefore, required that new material files be developed and stored in the database. For this purpose, Digimat MF and Digimat MX were used.

3.4.1 Generation of Digimat-AM Material Cards

In this work, four bioplastic cards were created: the first material card was the unreinforced rHDPE, the second material card was the 85% rHDPE + 15% RH without any compatibilizer, the third material card was the 45% rHDPE + 25% RH + 30% MAPE, and the fourth material card was the 40% rHDPE + 30% RH + 30% MAPE. The third and fourth material cards were to study the effects of the highest percentage of rice husk filler in the developed biocomposite, since they utilized the highest amount of compatibilizer.

To generate the Digimat-AM material cards, the properties of the main matrix and the inclusion, such as the filler, must be known. These properties were obtained from experimental investigation, as explained in the second objective of this study. The three main property types used were physical, thermal, and mechanical properties. The properties of the bioplastics are shown in Table 3.7, while those of the RH filler are shown in Table 3.8. The properties of rice husks are according to (Bisht, 2020; Singh, 2018).

Table 3.7: Experimental Properties of the Developed Bioplastics

Test	**Properties**	**100% rHDPE**	**85% rHDPE + 15% RH**	**45% rHDPE + 25% RH + 30% MAPE**	**40% rHDPE + 30% RH + 30% MAPE**
PVT	Density	924 – 995 kg/m³	893 kg/m³	823 kg/m³	789 kg/m³
Uniaxial static tensile	Young's Modulus	159.00 MPa	121.06 MPa	136.05 MPa	126.42 MPa
	Poisson's ratio	0.40 – 0.45	0.42	0.43	0.45
TMA	Coefficient of linear thermal expansivity	120 µm/m-°C	110 µm/m-°C	96 µm/m-°C	83 µm/m-°C
Thermal conductivity	Thermal conductivity of printed material	0.480 W/m-K	0.40 W/m-K	0.35	0.28
	Specific Heat Capacity	2250 J/kg*K	2124 J/kg*K	2010	1850
DSC	Melting temperature	120.83 °C	125.98 °C	120.79 °C	119.80 °C
	Crystallization temperature	99 °C	87 °C	79 °C	76 °C

Table 3.8: Properties of the Rice Husk Filler

Property	Value
Young modulus	0.3 – 2.6 GPa
Poisson ratio	0.2
Density	1.64 g/cm³
Coefficient of thermal expansion (mm/mm) /˚C)	6.67 (µm/m) / °C
Specific heat capacity	1.1502 - 2.1464 kJ/kg°C
Thermal conductivity ((mJ/s)/(mm*C))	0.584 - 0.637 W/m K
Fiber aspect ratio	1.4732
Fiber Orientation	A11=0.9 to 1; A22=A33, trace = 1

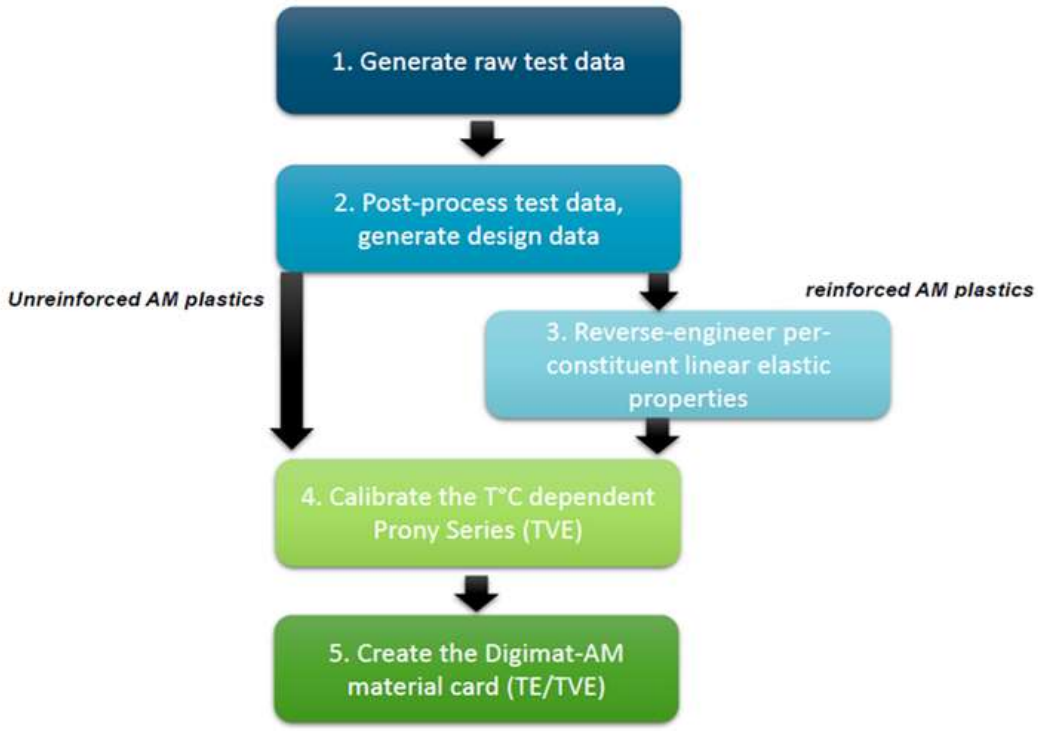

Figure 3.5: Process Flow from Test Data to Digimat-AM Software Cards

Figure 3.6 shows the general steps undertaken in generating material cards from experimental data. The first step involves generating raw test data, which is obtained from experiments conducted to determine the properties of the biocomposites and the filler reinforcements (Tables 3.7 and 3.8).

From the test data, the design data is generated through post-processing. This involves analyzing the statistical variability of the measurements and discarding any outliers. Average data from test samples is generated, and material behaviour is analyzed by studying trends in graphs to determine their validity. They should represent the main trends expected to fit the calibrated material card. This is checked through comparison with other materials and with the datasheet if it's available. For this case, the comparison was done by checking with other materials.

For unreinforced materials, after the post-processing of the test data to design data, the material properties can be defined in Digimat-AM to generate the thermo-elastic (TE) card. Step four is an optional step that can be performed in case one has thermomechanical analysis (TMA) data, and it applies to thermo-viscoelastic (TVE) cards. This step requires generating the Prony series and a shift function. In the case of unreinforced rHDPE, the fourth step was not performed. The test data was post-processed to generate the design data, which was later input into Digimat-AM to create the TE card.

For reinforced materials, the third step is performed, which involves reverse engineering to match the experimental properties of the biocomposites to the two-phase materials, that is, the phase matrix and the fiber matrix. This reverse engineering was carried out in Digimat MF, using earlier versions of Digimat up to version 2023.3. In this step, we deduce the material microstructure, such as fiber orientation relative to filament orientation and the aspect ratio. The matrix properties are also defined during this step. The reverse engineering of each linear elastic material property is performed in the following order:

- Specific volume
- Young's modulus
- Poisson's ratio
- Coefficient of thermal expansion, CTE
- Specific heat capacity
- Thermal conductivity

The reverse engineering of the constituent linear elastic property is done according to the steps outlined below:

Step 1: Determination of the matrix/resin density

In the determination of the matrix density, the rule of mixtures formula, Equation 3.7, was used:

$$\rho_{composite} = \rho_{filler} \; x \; f + \rho_{matrix} \; x \; (1 - f) \qquad (3.7)$$

Where: $\rho_{composite}$ is the density of the composite, ρ_{filler} is the density of the filler, f is the filler fraction and ρ_{matrix} is the density of the matrix/resin.

Since the densities of the composite and the rice husk filler are known from experimental investigation, the density of the matrix, ρ_{matrix} , can be determined using the Rule of Mixtures.

Step 2: Creation of a Digimat-MF thermo-elastic template material card

This step involved defining a single layer to account for the calibration of material properties from test data generated on perfectly aligned toolpaths. It is taken that the printing orientation of the layers does not change. For this case, 45° was chosen.

Step 3: Iterate the resin and filler variables until they match the composite properties obtained experimentally.

MF analyses are done, and the E-modulus and CTE of the resin, filler orientation, and aspect ratio are iterated until there is a fit to the target biocomposite moduli and CTE.

Step 4: Creation of a Digimat-MF thermal template material card.

Step 5: Iterate the resin's thermal conductivity and specific heat capacity until they match the experimentally obtained composite properties.

In steps 4 and 5, the fiber properties selected in previous steps are fixed, and MF analyses are performed. Iterations of the resin's thermal conductivity and specific heat capacity are done until there is a fit to the target biocomposite's thermal conductivity and specific heat capacity, as highlighted in Figure 3.6 and Figure 3.7.

The final stage, involves creating the Digimat-AM material card after the reverse engineering stage. This process is conducted within the Digimat-AM module. The manufacturing method is specified as FFF, and the high-fidelity warpage analysis type is selected. The material name is defined, the type is selected as reinforced fibers for the reinforced biocomposites, or unfilled for the unreinforced material. The rest proceeds in the solver, where the values of the physical, thermal, and mechanical properties of the three phases (matrix, filler, and composite) of the material are entered as obtained in the calibrated data in stage four.

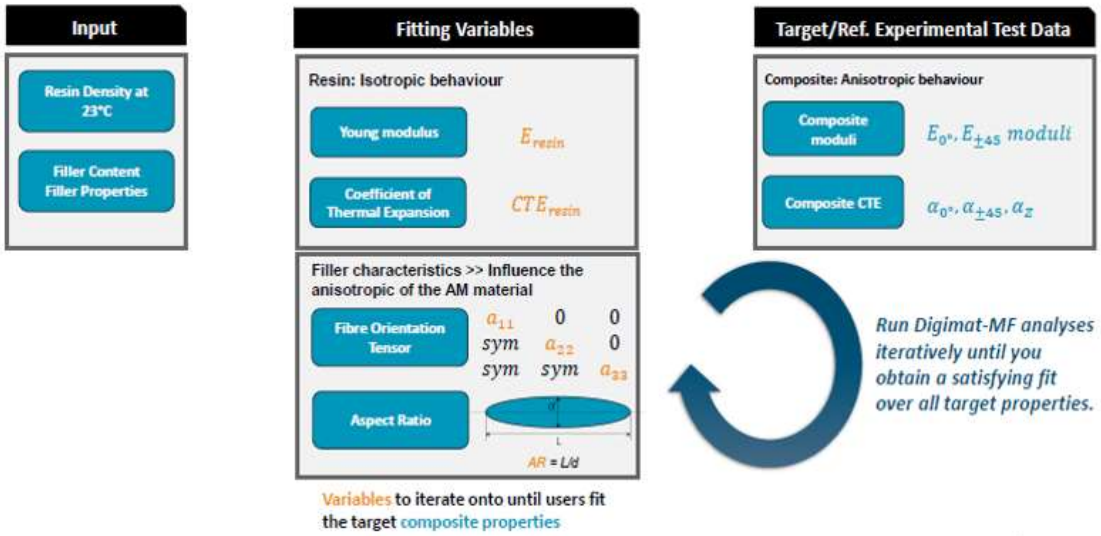

Figure 3.6: Calibration of the E-Modulus and Filler Properties on the Thermo-Elastic Material Card

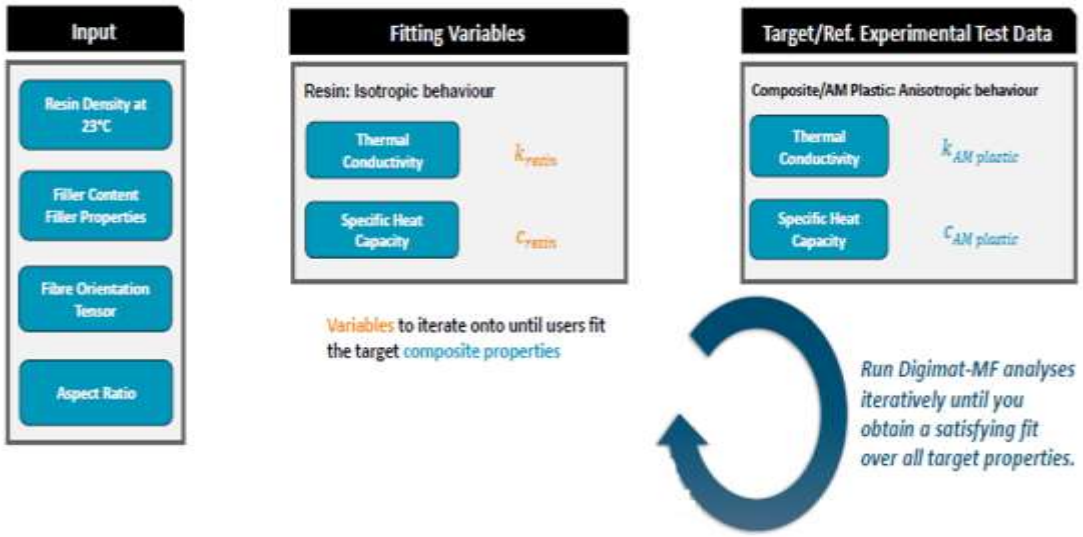

Figure 3.7: Calibration of the Thermal Conductivity and Specific Heat Capacity of the Resin on the Thermal Material Card

The material model is then stored in the database and can be selected during analysis. Figure 3.8 displays the material database in Digimat-AM, showing the created material files under the supplier's name, JKUAT, where they were generated. These material files are accessible for analysis within the Digimat-AM process simulation.

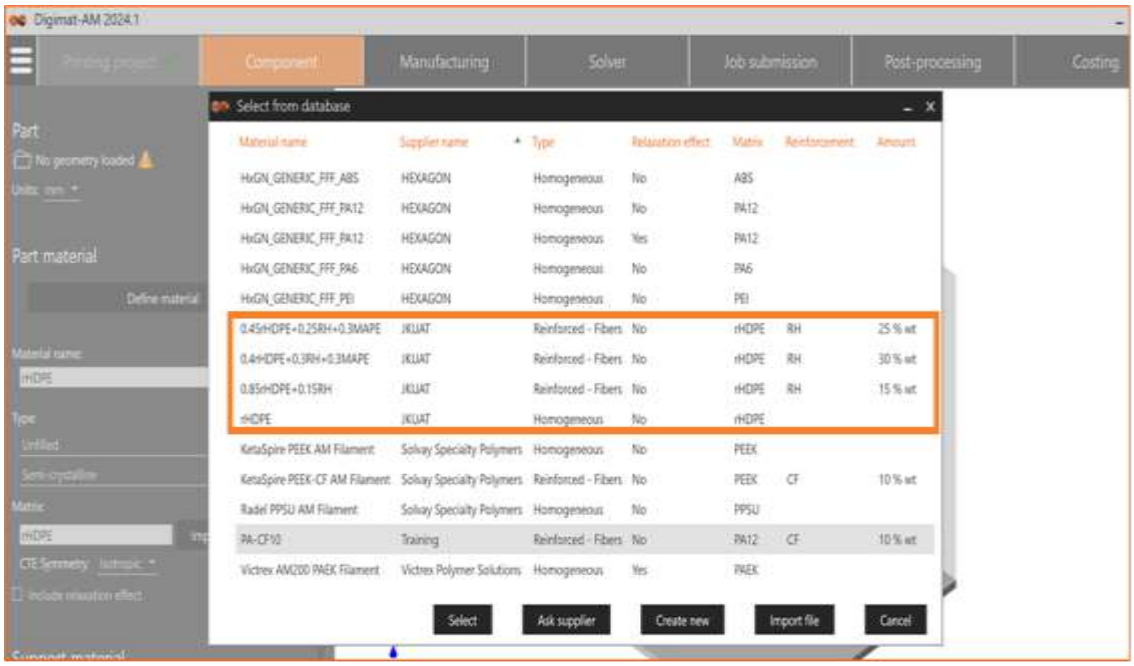

Figure 3.8: Digimat-AM Database Displaying Created Material Files

3.4.2 Reverse-Engineering in Digimat-MX

Reverse engineering in Digimat-MX is used to align the material model's properties with the experimental data. The above process is a manual workflow carried out in Digimat-MF and completed in Digimat-AM, where the phase properties are specified. This manual reverse-engineering workflow in Digimat-MF was used in earlier versions of Digimat, up to version 2023.3. From 2023.4 onwards, the reverse engineering stage was implemented in Digimat-MX. This module is more streamlined and semi-automatic. The thermo-elastic template file created in Digimat-MF is reverse-engineered in Digimat-MX. The steps in reverse-engineering in Digimat-MX are:

- Step 1: Loading the Digimat-MF thermo-elastic template material card in Digimat-MX.
- Step 2: Loading the tensile experimental data in Digimat-MX. The tensile data include stress-strain values and Poisson's ratios.
- Step 3: Loading the coefficient of thermal expansion (CTE) experimental data in Digimat-MX. These are the temperature values against CTE.
- Step 4: Select all the experimental files for analysis in the personal database. This excludes other files from the public database.
- Step 5: Reverse engineering workflow:

    i. Reverse-engineering of the matrix density based on the composite's density
    ii. Reverse-engineering of the matrix stiffness and material microstructure
    iii. Reverse-engineering of the matrix coefficient of thermal expansion (CTE)
    iv. Fine-tuning of all the calibrated parameters.

Figure 3.9 shows the reverse-engineering of the matrix density, where the composite's density and the filler density are entered. This automatically computes the matrix density based on the rule of mixtures. Figure 3.10 shows the reverse-engineering of the matrix stiffness and material microstructure, i.e., aspect ratio and orientation tensor. The three components of the orientation tensor, i.e., A11, A22, and A33, should sum to one. The ranges of the Young's modulus, Poisson's ratio, aspect ratio, and orientation tensor are defined, and the optimization is performed.

The dotted line in Figure 3.10 represents the experimental data, whereas the continuous lines represent the model data. Three sets of lines are seen, which represent the different orientations of the tensile sample during printing, i.e., x, y, and z orientations. In

calibrating, the goal is to fit the continuous lines to the dotted lines, which translates to fitting model data to the experimental data.

Digimat-MX has integrated an optimizer known as the Dakota, which was developed by Sandia National Laboratories. (Sandia National Laboratory, 2022). In this optimization technique, an objective function has been defined to minimize the difference between the experimental data and the simulation prediction. The error estimator, e, is defined as

Equation (3.8) and (3.9):

$$e = \frac{\sum_{i=1}^{n} \left(\frac{Y_c(i)}{Y_r(i)} - 1\right)^2}{n} \quad (3.8)$$

$$e = \sum_{j=1}^{m} w_j e_j \quad (3.9)$$

Where:

- X_r, Y_r point on the reference curve
- $Y_c\ (i)$ point on the computed curve, interpolated at $X = X_r$
- w_i the weight of the curve

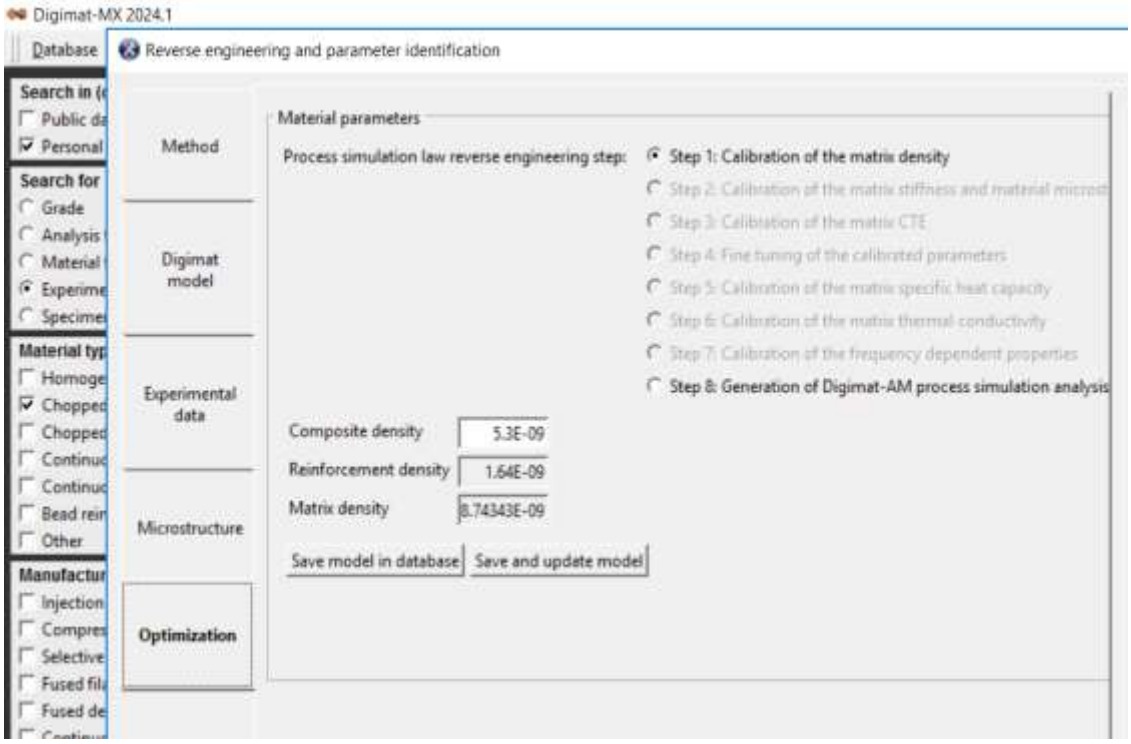

Figure 3.9: Reverse-Engineering to Calibrate the Matrix Density

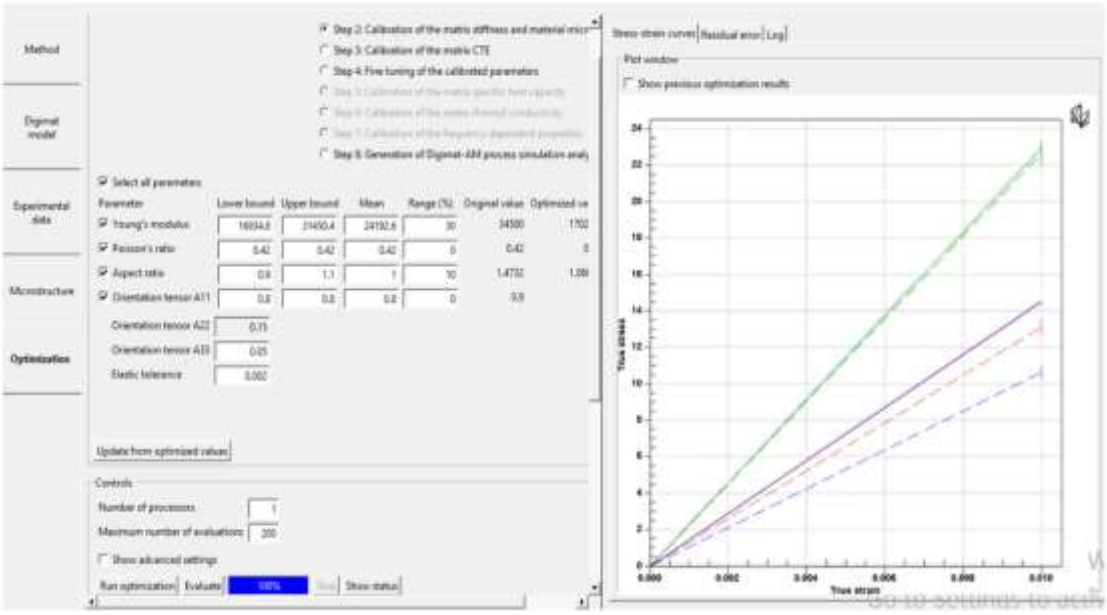

Figure 3.10: Reverse-Engineering of the Matrix Stiffness and Material Microstructure

Figure 3.11 shows the matrix calibration of CTE, in which CTE was computed at three temperatures, as recommended by the Digimat software developers for composite materials. The range is set to the default value of 80, which generates the lower and upper CTEs. From the defined material microstructure in previous steps, the matrix CTE is deduced for each temperature, which explains the composite's behavior in terms of temperature and anisotropy. The lower curve represents the CTE in the x-direction, where the fibers are highly aligned, resulting in the composite's lowest thermal expansion. This is followed by the y-direction CTE, appearing as the middle curve and the uppermost curve with the lowest orientation to A33 and closer to the matrix CTE.

Fine-tuning of the parameters is performed if a discrepancy is found between the stiffness, CTE, and the material microstructure defined in step 2. This further improves the calibrated parameters. These parameters are selected, and a global optimization is conducted. If the fine-tuning is not necessary, the model is then saved in the database, and the workflow is completed. After the reverse-engineering, the material cards are converted into Digimat-AM material cards for process simulation. The material card is now stored in Digimat-AM's database and can be used for process simulation. In this database, additional thermal properties, such as specific heat capacity and thermal conductivity, can be included.

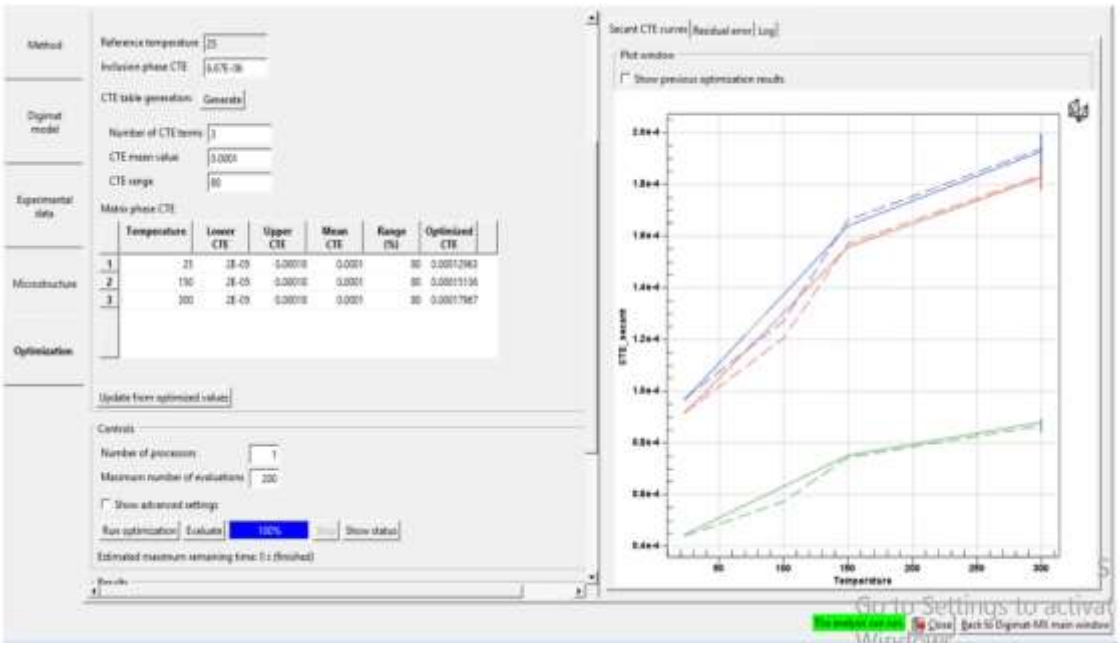

Figure 3.11: Reverse-Engineering of the Matrix Coefficient of Thermal Expansion (CTE)

3.4.3 Fused Filament Fabrication Process Simulation

Digimat-AM was used to simulate the FFF process and study warpage, residual stresses, and the effect of selected printing parameters. The simulation environment allowed various parameters to be varied and tested at minimal cost compared to experimental testing, enabling their effects to be studied. In this work, a tensile test sample was used to simulate and predict structural performance. For each test, three samples were considered. The sample is illustrated in Figure 3.12. In terms of applicability, a breath sampler casing was selected because its mechanical strength matches that of the developed bioplastic. This is illustrated in Figure 3.13, which was also designed to study its printability with the developed materials. The analyzer adapter was selected for testing.

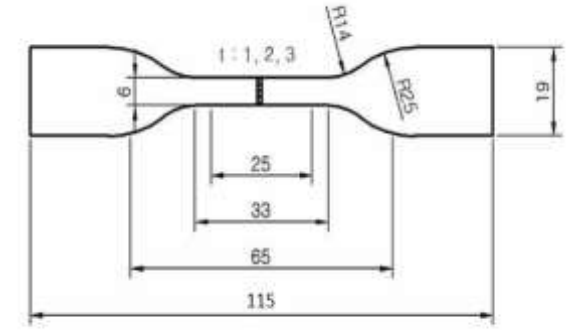

Figure 3.12: ASTM D638 - Type IV Tensile Specimen (Dimensions in mm)

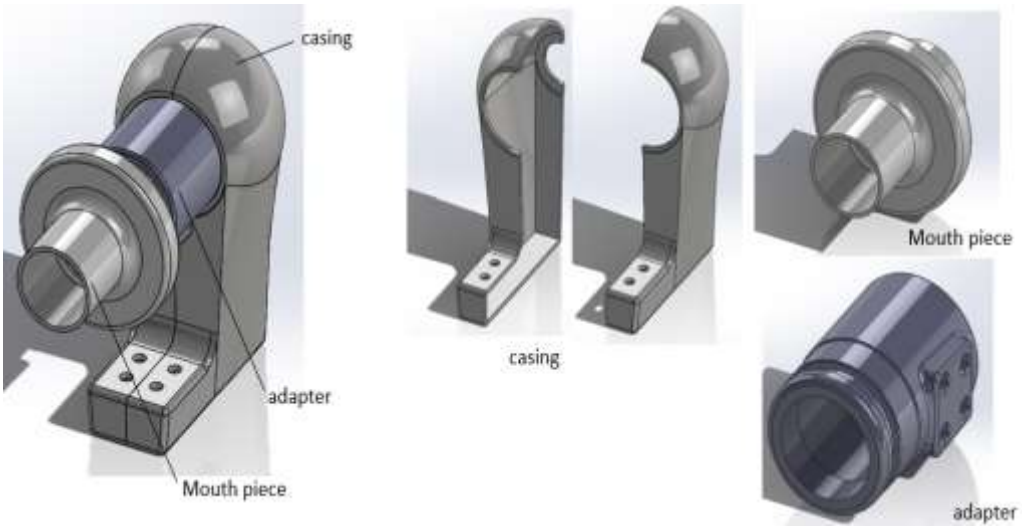

Figure 3.13: CAD Drawings of the Breath Analyzer

Figure 3.14 illustrates the FFF process simulation used to predict warpage and optimize process parameters. The printer was defined, and the analysis type was set to “Warpage low-fidelity”. The part geometry was imported as an .STL file, and the material was chosen. The simulation was conducted for four different materials modeled in the Digimat-MF and Digimat-MX modules.

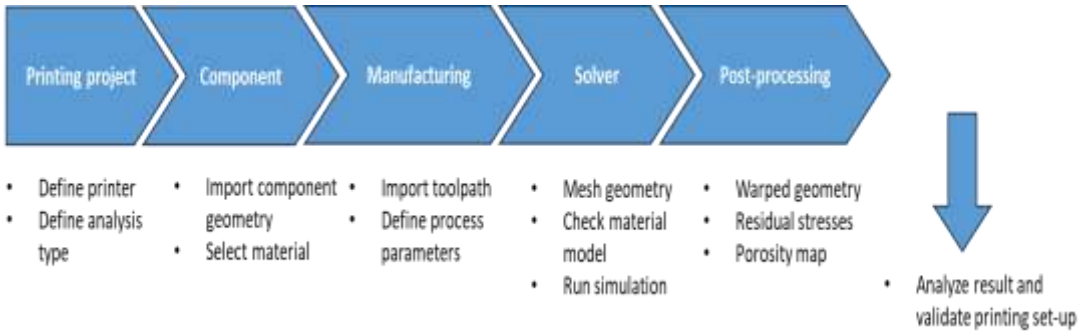

Figure 3.14: Workflow for the Prediction of Warpage and Residual Stress in FFF Simulation

After selecting the material, the toolpath was imported, generated from slicing software—specifically, the Prusa Slicer—and then process parameters were defined. Although some parameters were set within the toolpath, they could be adjusted in the simulation environment. The four main parameters considered in this simulation were extrusion temperature, bed temperature, printing speed, and layer height, as these have the most significant influence on the results. Other parameters remained constant. In the solver, the geometry was meshed with a 0.25 mm mesh size, and the simulation was run to determine residual stresses and warpage. During postprocessing, a warpage compensation geometry is available, which can be exported for use. Table 3.9 presents the selected parameters and their corresponding levels, which were chosen based on experimental investigations. The factors kept constant are listed in Table 3.10. Figures 3.15 and 3.16 illustrate the meshed geometries of the two designs in the Digimat-AM simulation environment.

Since the simulation results gave the final part dimensions, showing the warpage, the warpage was calculated using Equation (3.10):

$$Warpage = \frac{Highest\ point - Lowest\ points}{Original\ height} \quad (3.10)$$

Table 3.9: Input Factors for the FFF Simulation and their Levels

Factor	Level 1	Level 2	Level 3
Extrusion temperature, °C	210	220	230
Bed temperature, °C	60	90	120
Print speed, mm/s	20	30	40
Layer height, mm	0.1	0.15	0.2

Table 3.10: Factors Kept Constant for the FFF Simulation

Chamber temperature	Infill percentage	Print pattern	Build orientation	Nozzle diameter
50˚C	100%	Rectilinear	Flat	0.4 mm

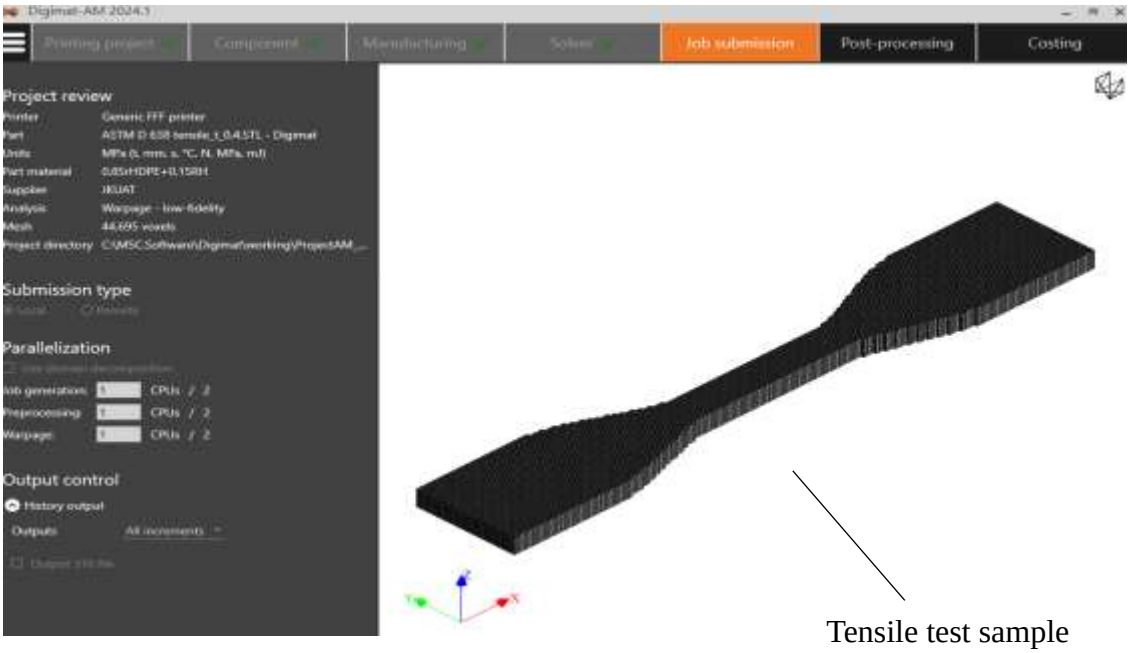

Figure 3.15: Screenshot of the Tensile Test Sample in Digimat Software

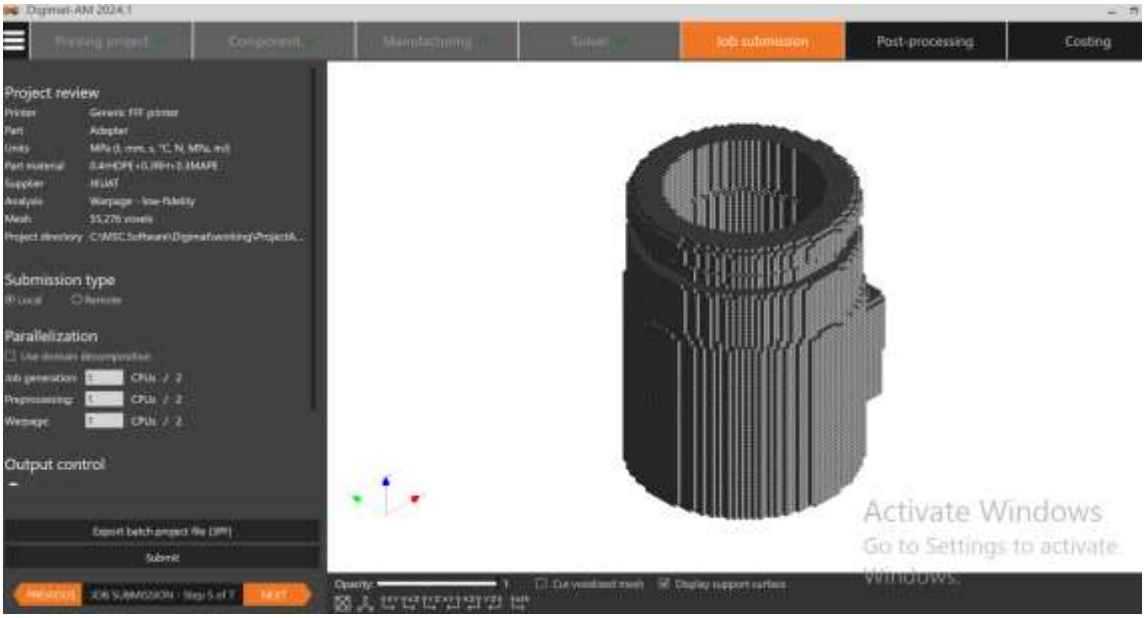

Figure 3.16: Screenshot of the Meshed Geometry of the Breath Analyzer Adapter

3.4.4 Taguchi Design of Experiment and Optimization using Grey Relational Analysis

The Taguchi design of experiment approach was employed to determine the experimental design, which was conducted using Minitab Statistical Software 22. Taguchi introduced the concepts of orthogonal arrays and signal-to-noise ratios to help designers develop a robust process that relies less on noise factors. Taguchi's methods focus on reducing variability in responses, unlike traditional DOE techniques that emphasize average responses and specifications (Srivastava & Rathee, 2018).

In this study, warpage and residual stresses were selected as the response variables to be minimized. Taguchi's orthogonal array technique was employed to determine the combinations for the experimental runs. Table 3.11 displays the combinations of the four input parameters at three levels listed using the L_9 Taguchi orthogonal array. These combinations were used in simulations to determine the one that yielded the best results in terms of minimum residual stresses and warpage. For each run, slicing was performed to generate the tool path, which was then loaded for the printing process.

Table 3.11: Taguchi L_9 DoE for the FFF Simulations

Experiment	Extrusion Temperature, °C	Bed temperature, °C	Printing Speed, mm/s	Layer height, mm
1	210	60	20	0.1
2	210	90	30	0.15
3	210	120	40	0.2
4	220	60	30	0.2
5	220	90	40	0.1
6	220	120	20	0.15
7	230	60	40	0.15
8	230	90	20	0.2
9	230	120	30	0.1

The Grey Relational Analysis (GRA) was employed to optimize process parameters, as it enables multi-response optimization when there are two or more responses to be optimized. The goal was to minimize residual stresses and warpage. In this analysis, a grey relational grade (GRG) was used, where a single value represented all related responses. The process for calculating the GRG is described in studies by (Lin et al., 2002; Wojciechowski et al., 2018). The procedure begins with normalizing responses within a range of 0 to 1, as presented in Equation (3.11), i.e.

Normalized response:

$$= \frac{Max\ (y_{ij}, i=1,2,\ldots,n) - y_{ij}}{Max\ (y_{i,j,}\ i=1,2,\ldots,n) - Min\ ((y_{i,j,}\ i=1,2,\ldots,n)} \qquad (3.\ 11)$$

Where:

- n is the maximum number of experimental runs from the DOE
- $y_{i,j,}$ is the simulated response with j = 1,2,…,n; i = 1, 2,…,n.

To minimize the responses, the "smaller the better" characteristic was chosen in this analysis. Therefore, normalization aimed to reduce the variability of the results.

The absolute value of the difference (Δ) was then calculated by subtracting each normalized value from the most significant normalized value. The difference is shown in Equation (3.12). The calculation is based on:

$$\Delta = 1 - Z_{i\ j} \qquad (3.\ 12)$$

Where:

- Z_{ij} - is the jth response after normalization

The grey relational coefficient (GRC) is calculated as shown in Equation (3.13):

$$GC_{ij} = \frac{\Delta min + \lambda \Delta max}{\Delta_{ij} + \lambda \Delta max} \quad (3.13)$$

Where:

- GC_{ij} is the GRC for the *i*th experiment and the *j*th response

- λ is a unique coefficient whose value ranges from 0 to 1

The GRG was calculated as the mean of the GRC for each performance property. It was used to convert the multiple responses into a single final determinant for the optimal responses and factor levels. The GRG reduces randomization and enhances the consistency of data. The GRG (*Gi*) for the *i* th experimental run and *n* responses was calculated as shown in Equation (3.14):

$$G_i = \frac{1}{n} \sum_{i=1}^{n} GC_{ij} \quad (3.14)$$

3.4.5 Structural Modeling

The ASTM D638 Type IV tensile test sample was designed using SolidWorks software for structural simulation. The Ansys 2023 R2 software was used for structural modeling and simulation, where finite element analysis (FEA) was performed. A static structural

analysis was performed, generating a fine mesh. As for the boundary conditions, one end was fixed, and a load of 10,000 N was applied to the other end.

3.4.6 Structural Analysis - Coupled Simulation

A structural analysis was conducted to determine the part performance that is influenced by the manufacturing process and the material model. This analysis was performed in Digimat-MS, which accurately predicts part performance by building a coupled simulation. The coupled simulation was done on the tensile test specimen, which included the developed Digimat material models from Digimat-MX, the manufacturing model (tool path) from Digimat-AM, and the structural model developed in Ansys. The material models defined the material's mechanical properties, thermal properties, and microstructure. The manufacturing model defined the printing process parameters, resulting in residual stress, temperature gradients, and warpage. The structural model defined the part geometry, boundary conditions, and the loading forces. The three coupled models are illustrated in Figure 3.17.

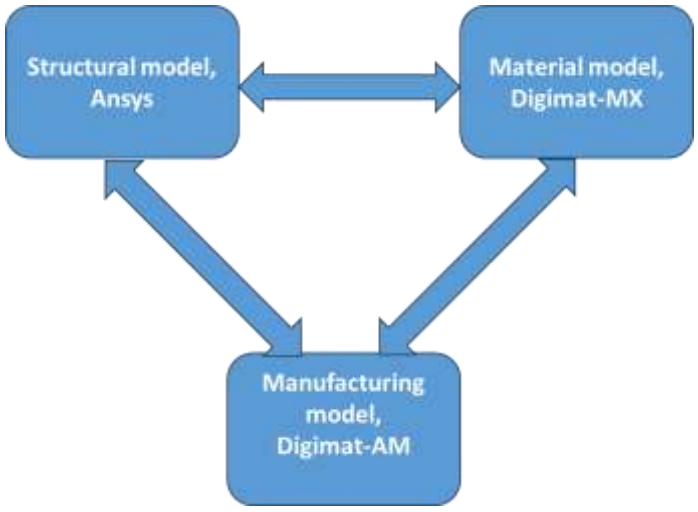

Figure 3.17: Illustration of the Coupled Models

The process of building a coupled simulation is summarized in Figure 3.18 below.

Figure 3.18: Steps in Building a Coupled Simulation

- Step one involved loading the FEA model / structural model from Ansys into Digimat MS.
- Step two involved loading the Digimat material from Digimat MX.
- Step three involved mapping of the tool path, residual stresses, and printing direction, i.e., automatic superposition of the structural (FEA model) and the manufacturing model, as shown in Figure 3.19.
- Step four was to perform the coupled analysis. In this study, a hybrid solution was chosen because it's suitable for both linear and nonlinear materials and enables strong coupling.

From the analysis, the outputs included accumulated plastic strain, a failure indicator, and damage. Figure 3.20 illustrates the Digimat-MS setup, indicating the orientation of the fibers (inclusions).

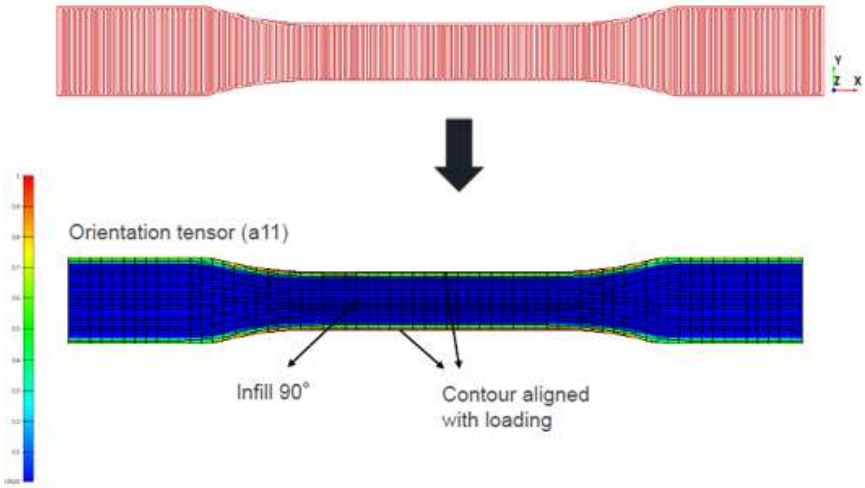

Figure 3.19: Illustration of the Mapping of Toolpath Information to the FEA Mesh

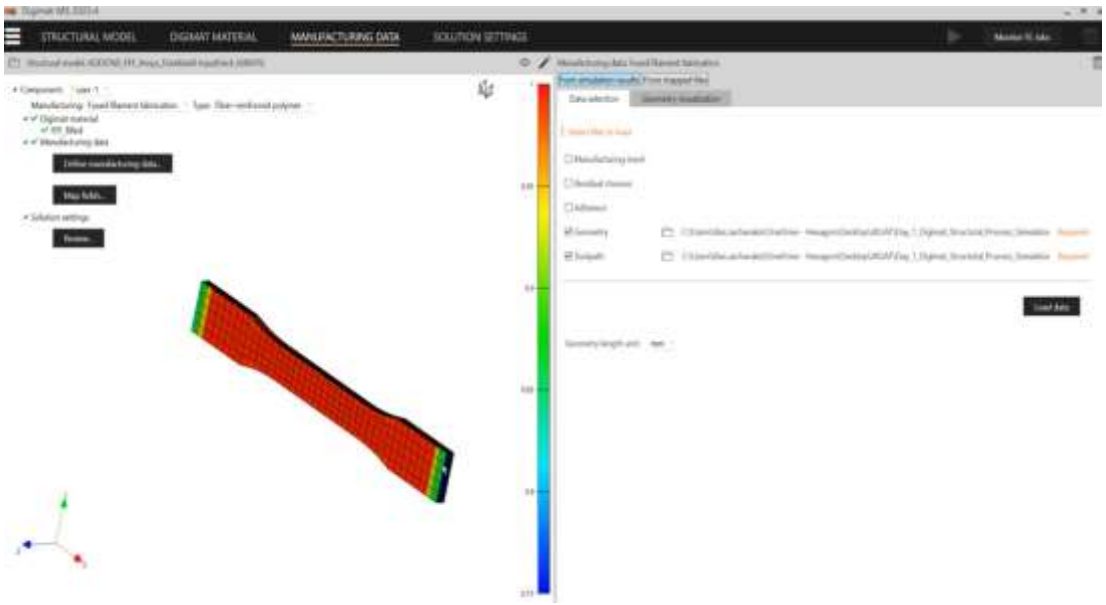

Figure 3.20: Illustration of the Orientation Tensor after Mapping

3.4.7 Experimental Validation of the Fused Filament Fabrication

The Creatbot F430 was used for experimental validation. This is a closed chamber printer. The technical specifications are indicated in Table 3.12. The Creatbot features a fully enclosed chamber that can maintain a temperature of up to 70°C, thereby preventing printed parts from warping and deforming.

Table 3.12: Technical Specification Creatbot F430

Parameter	Value
Volume	400 x 300 x 300
Maximum Nozzle Temperature	420°C
Maximum Bed Temperature	140°C
Maximum Chamber Temperature	70°C
Maximum Printing speed	180 mm/s
Best Printing speed	55 mm/s
Nozzle diameters	0.4mm (0.3 0.5 0.6 0.8 1.0mm)
Filament Diameter	1.75 mm

The tensile samples were printed at the optimal parameters and tested for warpage and residual stresses.

3.4.8 Experimental Validation of Warpage Measurement

The VK-X1000 series laser confocal microscope by Keyence was used to measure the warpage of samples. It offers a non-contact method for assessing surface profiles by analyzing height data from scans and calculating deviations from a flat plane, thereby quantifying warpage. The confocal microscope uses a 404 nm laser with a 20 nm vertical resolution over areas up to 50 mm x 50 mm. Figure 3.21 shows the scanned image of the printed part used to analyze warpage. In the analysis, the microscope captured an accurate 3D model of the scanned surface. Using the VK-X Multifile Analyzer software, deviations from the flat surface reference are identified, and the values of these deviations are presented. Three samples were analyzed for each of the modeled bioplastics.

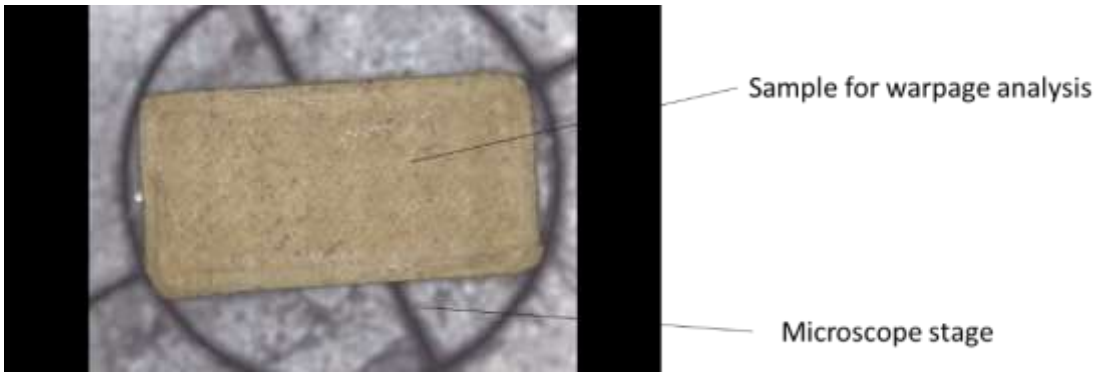

Figure 3.21: Navigation Image of the Printed Part

3.4.9 Experimental Validation of Residual Stress Measurement

Residual stress was measured using X-ray diffraction, a non-destructive method that assesses the material's strain by analyzing diffraction patterns of the X-rays. It employs high-energy light to determine the distance between atoms in a specific direction of the sample. From these atomic distances, the stored strain within the crystal structure can be calculated and converted into residual stress. The X-ray diffraction measurements were performed on a Panalytical Empyrean X-ray polycrystalline diffractometer in Bragg-Brentano geometry, equipped with a long-focused sealed Cu X-ray tube ($\lambda K\alpha$ = 1.5418 Å), and PIXcel 1D X-ray detector. The patterns were collected in continuous mode between 5° and 140° (2θ), with a step size of 0.02626 °. In Bragg-Brentano geometry, the incident angle/tilt angle is always half of the 2θ. The Bragg's Law shown in Equation 3.15 relates the X-ray wavelength, the diffraction angle, and the interplanar spacing:

$$n\lambda = 2\,d\sin\theta \qquad (3.\ 15)$$

Where:

- λ is the wavelength of the X-rays, which was 1.5418 Å
- d is the interplanar spacing (d-spacing)
- θ is the diffraction angle

The measurement of the residual stress is based on the $sin^2\psi$, which is the most common technique. The different geometries are illustrated in Figure 3.22, where:

– X-rays are directed onto a sample's surface at different tilt angles ψ.

– The diffraction peak position (2θ) is recorded at each tilt ψ

– The strain ε_ψ , is calculated from the shift in the *d*-spacing at different angles. The strain is shown in Equation (3.16):

$$\varepsilon_\psi = \frac{d_\psi - d_0}{d_0} \qquad (3.16)$$

Where:

- d_ψ is the interplanar spacing at the tilt angle
- d_0 is the stress-free spacing, 3 mm, for the case of the samples used in this analysis

– A plot of strain ε_ψ vs $sin^2\psi$ is drawn, according to Equation (3.17), and the slope of this plot is proportional to the residual stress.

$$\sigma = \frac{E}{1+\nu} \cdot \frac{d_\varepsilon}{d(sin^2\psi)} \qquad (3.17)$$

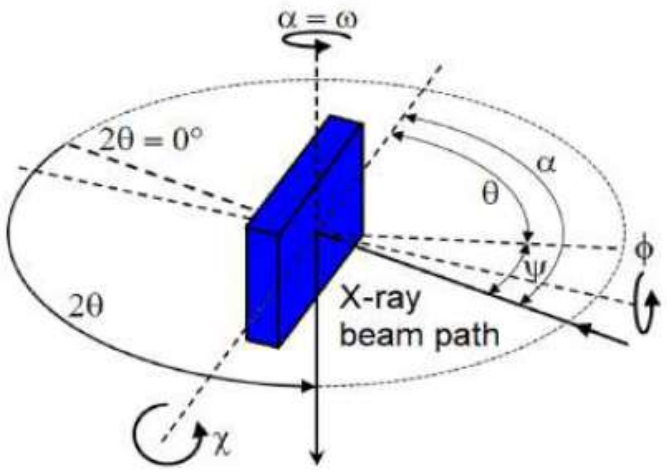

Figure 3.22: X-Ray Diffraction Geometries during the Investigation

3.4.10 Building of Biosensor Substrate from Developed Material

A rigid microfluidic substrate was designed and 3D printed using the developed biofilament. The design is as shown in Figure 3.23. The substrate is a part of a biosensor for analyzing biomedical fluids.

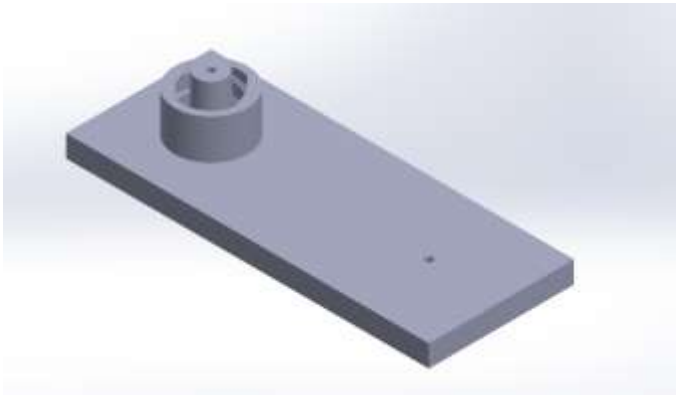

Figure 3.23: Microfluidic Substrate

CHAPTER FOUR

RESULTS AND DISCUSSION

4.1 Overview

This chapter presents the results for each objective that was set. The fabricated biofilaments are shown, and their properties are discussed based on the characterization techniques employed. The results of the modelled materials and their printability, as simulated, are discussed. Key trends and findings are highlighted and discussed according to prior literature and theoretical concepts.

4.2. Properties of Milled Rice Husks

The milled rice husks were analyzed to determine their particle size distribution, aspect ratio, and sphericity. Information on these parameters helps predict the mechanical properties, thermal properties, filler dispersion, processability, and shrinkage of the resulting bioplastics.

The cumulative particle size distribution is represented by two curves, as shown in Figure 4.1. The blue curve displays the particle size, d, in the classified rice husks, while the black curve indicates the percentage of particle distribution, Q3(d). Approximately 96 % of the particles were less than 75 µm in size. A peak at 10 µm particle size is observed, indicating a low cumulative distribution of approximately 10 %, which suggests a low percentage of very fine particles in the rice husks.

A low cumulative distribution helps achieve uniform dispersion within the polymer matrix. A second peak appears at approximately 52% of particles with a 30 µm size. This indicates that about half of the rice husk particles are smaller than 30 µm. At around 60 µm, a final peak is seen, with roughly 85% of the particles being 60 µm or less. These curves show how the rice husk filler is distributed within the polymer matrix. These fine

particles improve filler packing within the main matrix, increasing loading without affecting processability.

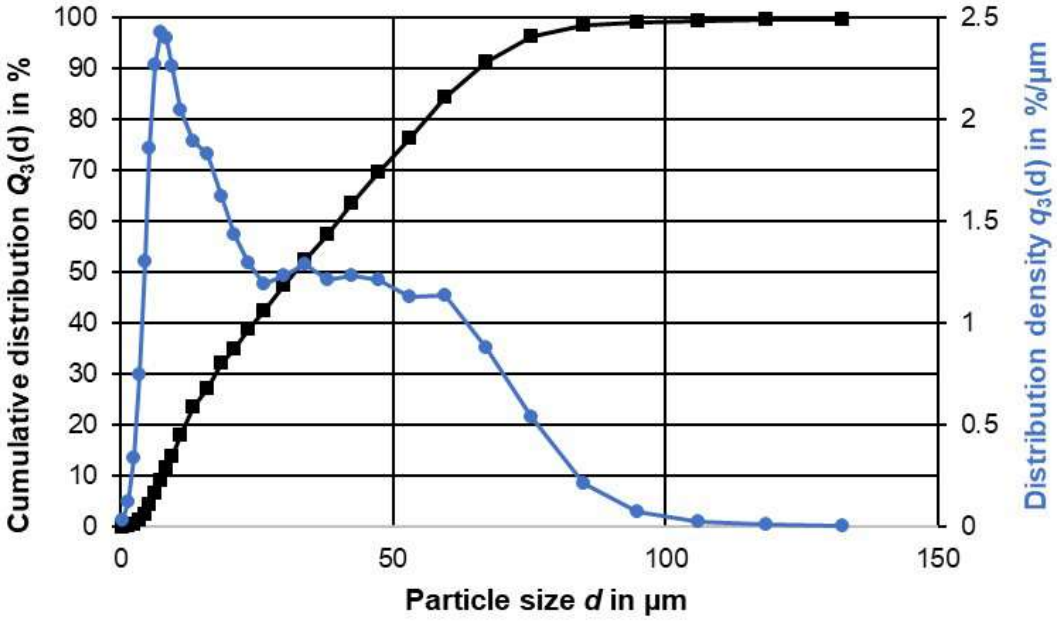

Figure 4.1: Cumulative Distribution of the Milled Rice Husks

The aspect ratio, which is the ratio of the length to the width of the particles, of the milled rice husks ranged from 1.1 to 1.5, as shown in Figure 4.2. At particle sizes less than 75 µm, the aspect ratio was below 1.47, qualifying the milled rice husks as short fibers (Kenny & Nicolais, 1989). As fillers, short fibers improve the processability of the biocomposite material during extrusion (Avient Corporation, 2024).

The sphericity of the milled rice husks ranged from 0.73 to 0.93, as shown in Figure 4.3. At approximately 75 µm, the sphericity was 0.84. This high sphericity ensures high flowability and low viscosity during product mixing and extrusion, compared to irregular particles, thereby minimizing wear and tear on the equipment. The tap density of the rice husks was measured at 0.626 g/cm3, and the Hausner's number was 1.385, suggesting good flowability.

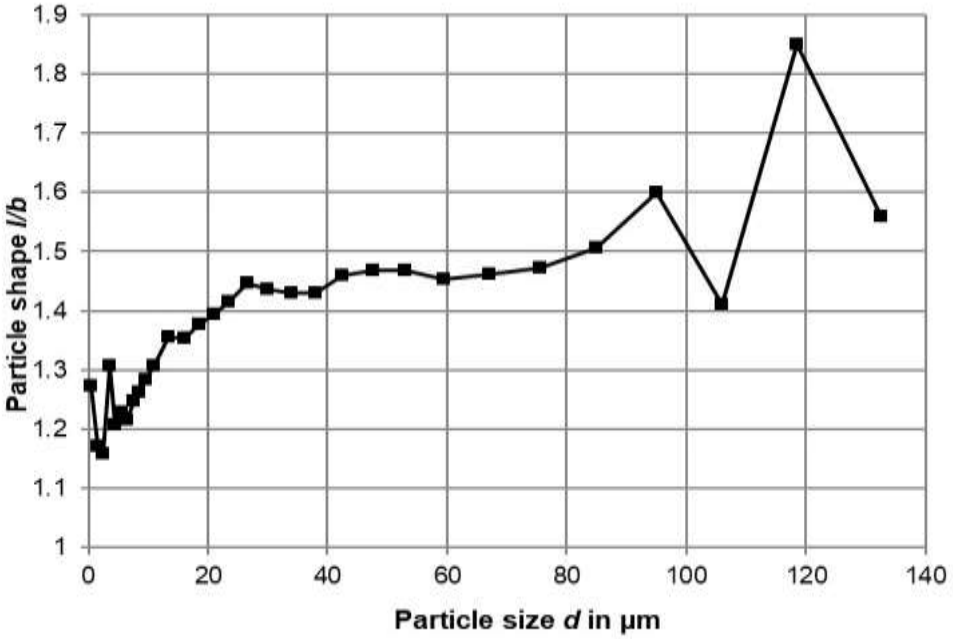

Figure 4.2: Aspect Ratio of Milled Rice Husks

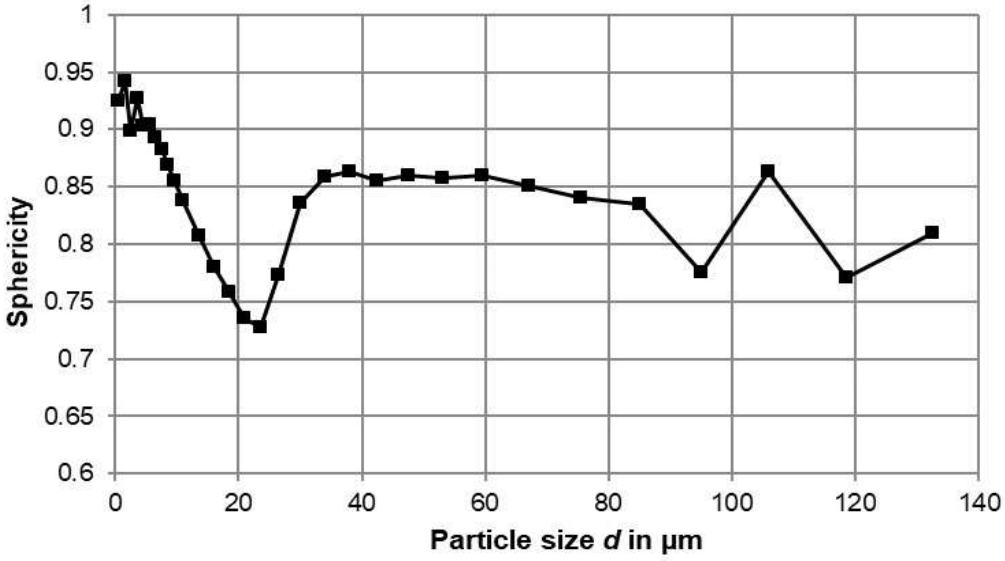

Figure 4.3: Sphericity of the Milled Rice Husks

4.3 Fabricated Biofilaments

The biofilaments were produced using a filament extrusion system by melt-mixing recycled high-density polyethylene with rice husk filler at various ratios listed in Table 3.3. The resulting spooled biofilaments are shown in Figure 4.4. Spooling was successful up to 30 wt.% RH filler in the mixture. At 35 wt.%, the biofilament could not be spooled because it broke due to increased brittleness. This brittleness was caused by poor bonding between the matrix and fibers at high fiber content. The hydroxyl groups in the natural fibers of RH are polar and hydrophilic, while the rHDPE is non-polar and hydrophobic. This mismatch created a weak interface bond between the matrix and the fibers, reducing ductility and flexibility.

The material extrusion remained consistent with a composition of up to 15 wt.% rice husks. Beyond 15 wt.%, extrusion became inconsistent, and material flow was hindered, leading to nozzle clogging. This issue required adding a compatibilizer, specifically maleic anhydride-functionalized polyethylene. The compatibilizer acted as a solid surfactant to improve interfacial adhesion and compatibility between the polar rice husks and the non-polar recycled high-density polyethylene.

To achieve better flowability with 20 wt.% rice husk filler in the biofilament, 5 wt.% Maleic anhydride functionalized polyethylene was used, as recommended by the manufacturer. To increase the rice husk content beyond 20 wt. and improve the filament's flowability, the amount of maleic anhydride functionalized polyethylene had to be raised to the maximum allowed level of 30 wt.%.

The primary mechanisms for interaction between the rHDPE matrix and the organic fibers from the rice husks at the interface include physical bonding or interlocking, where the molten matrix flows within the pores of the rice husk powder. An interdiffusion occurs between the rHDPE matrix and the organic rice husk particles, forming a strong physical bond upon cooling. On the addition of the MAPE plasticizer, there was the introduction of covalent bonds between the hydroxyl group in the rice

husk filler and the polymer chains of rHDPE, since the plasticizer acts as a coupling agent.

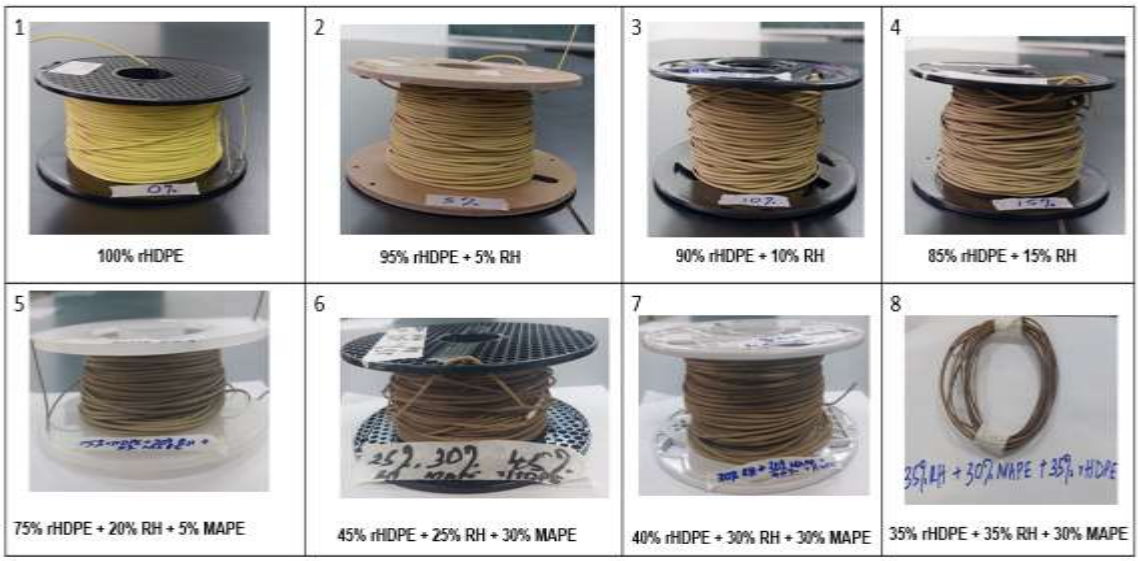

Figure 4.4: Fabricated Biofilaments with Different Compositions

The maximum percentage of rice husk filler that could be added to the biocomposite was 35 wt.%. Adding more rice husk filler caused nozzle clogging due to increased melt viscosity, which hindered the extrusion of the material. Commercial biofilaments contain up to 40 wt.% of fiber (T. C. Yang et al., 2017). Increasing the fiber content beyond this in biofilaments leads to uneven swelling or shrinking of the fibers, roughening of the surface, and an increased risk of voids and shape variations (Kariz et al., 2018; Lamm et al., 2020).

The Taguchi experimental design analysis, conducted using Minitab 18 software, revealed that the heaters had the most significant impact on filament diameter, followed by screw speed and then roller speed, as shown in Figure 4.5. In this design analysis, the level of significance is expressed in terms of rank, where the parameter with the most significant contribution will have a rank value of ‘1’. The contribution of the other parameters will have their ranks follow in that order.

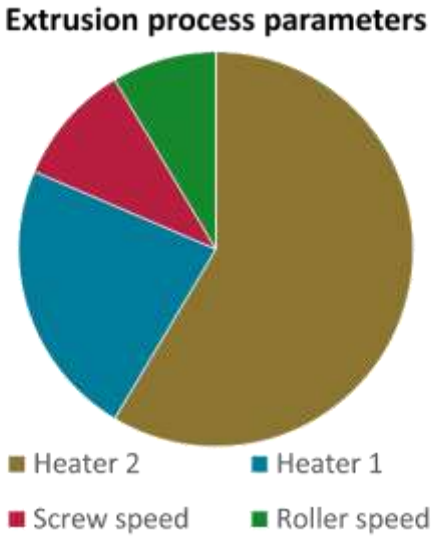

Figure 4.5: Fabrication Parameters According to Rank

Table 4.1: Response Table for Means for 100 wt.% rHDPE

Level	**Heater 1**	**Heater 2**	**Screw speed**	**Roller speed**
1	1.710	1.740	1.650	1.640
2	1.620	1.643	1.723	1.683
3	1.700	1.647	1.657	1.707
Delta	0.090	0.097	0.073	0.067
Rank	**2**	**1**	**3**	**4**

Table 4.1 presents the response means for 100 wt.% rHDPE of the four parameters at the three levels. This is summarized in the "Main Effect Plot for Means" plot shown in Figure 4.6, which highlights the response at different parameter settings.

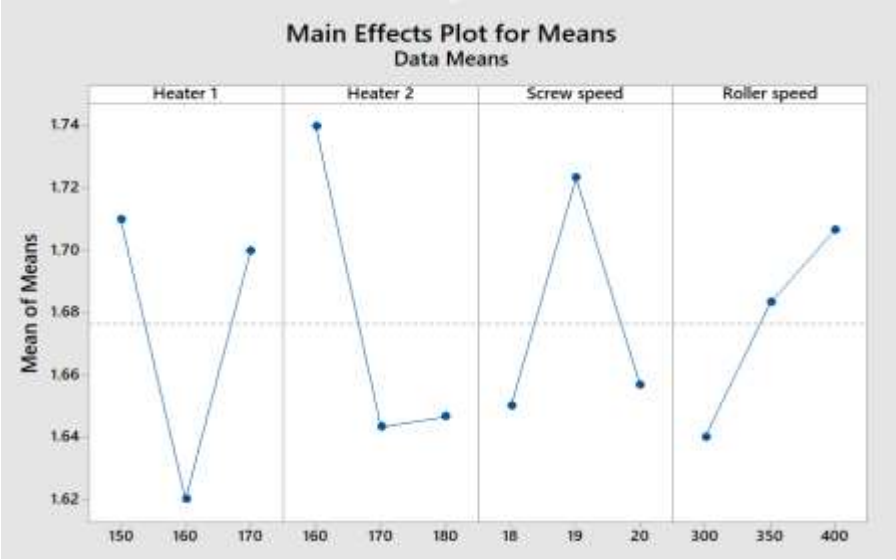

Figure 4.6: Main Effect Plot for Means -100 wt. % rHDPE

The best settings for the 100 wt.% rHDPE filament extrusion process parameters were identified as heater 1 temperature at 150 °C, heater 2 temperature at 160 °C, screw speed at 18 revolutions per minute, and roller speed at 300 revolutions per minute.

As seen in Table 4.2, the 95 wt. % rHDPE + 5 wt. % RH biofilament, heater 1 had the greatest impact on filament extrusion, followed by roller speed, then heater 2, and finally, the screw speed. This change in the ranking of the parameters was due to the addition of rice husk waste, which affected the thermal and rheological behavior of the biocomposite.

Table 4.2: Response Table for Means for 95 wt.% rHDPE + 5 wt.% RH

Level	Heater 1	Heater 2	Screw Speed	Roller Speed
1	1.637	1.743	1.733	1.767
2	1.773	1.733	1.720	1.680
3	1.730	1.663	1.687	1.693
Delta	0.137	0.080	0.047	0.087
Rank	1	3	4	2

The best settings for extruding the biofilament with 95 wt.% rHDPE and 5 wt.% RH composition, according to Figure 4.7, were heater 1 temperature at 160 °C, heater 2 temperature at 160 °C, screw speed at 18 revolutions per minute, and roller speed at 300 revolutions per minute. The temperature of heater 1 was increased from 150 °C to 160 °C to combat the increase in viscosity caused by the addition of the organic filler. These values were determined through experimental investigation.

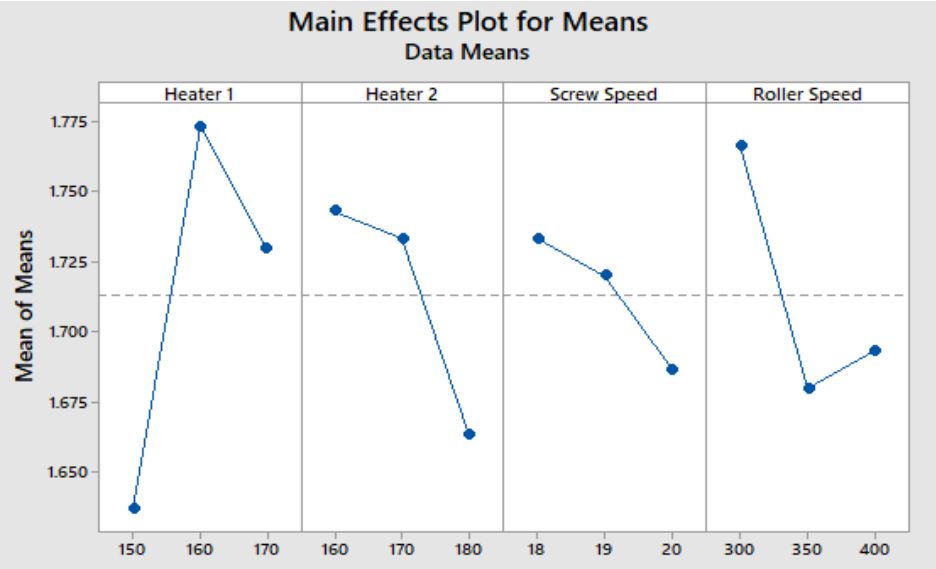

Figure 4.7: Main Effect Plot for Means - 95 wt. % rHDPE + 5 wt. % RH

The organic filler caused an increase in the material's viscosity, leading to decreased flowability, which in turn reduced the biofilament's sensitivity to heater temperature and increased its sensitivity to roller speed, influencing the rate at which the biofilament is wound at the final stage of extrusion.

From Table 4.3, the biofilament with a composition of 90 wt.% rHDPE and 10 wt.% RH had heater 2 as the parameter with the highest contribution to filament diameter consistency, followed by roller speed, then heater 1, and lastly screw speed. Again, the heater temperatures had the most significant impact, as they affect the viscosity of the biofilament. There was a switch where now heater 2 was higher in ranking than heater 1,

though this switch has minimal impact since the heaters can also be treated as the same parameter.

Table 4.3: Response Table for Means for 90 wt.% rHDPE + 10 wt. % RH

Level	Heater 1	Heater 2	Screw speed	Roller Speed
1	1.683	1.780	1.640	1.723
2	1.717	1.650	1.700	1.703
3	1.647	1.617	1.707	1.620
Delta	0.070	0.163	0.067	0.103
Rank	**3**	**1**	**4**	**2**

The best settings for extruding this, according to Figure 4.8, were heater 1 temperature at 160 °C, heater 2 temperature at 160 °C, screw speed at 20 revolutions per minute, and roller speed at 300 revolutions per minute. The increase in the screw speed from 18 to 20 meant that a high speed was required to maintain the extrusion rate due to the increased viscosity.

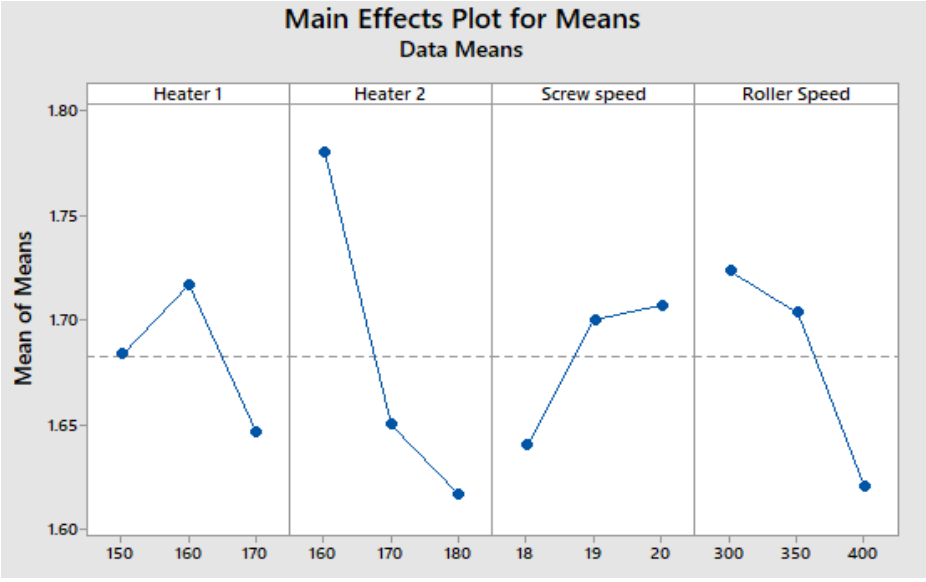

Figure 4.8: Main Effect Plot For Means – 90 wt.% rHDPE + 10 wt.% RH

Table 4.4 presents the responses for the means of biofilament with 85 wt.% rHDPE + 15wt.% RH. As previously seen, the heater temperature had the greatest impact on the biofilament extrusion. This was followed by screw speed and, lastly, roller speed. The best extrusion settings according to the analysis in Figure 4.9 were, heater 1 temperature at 160 °C, heater 2 temperature at 160 °C, screw speed at 19 revolutions per minute, and roller speed at 300 revolutions per minute.

Table 4.4: Response Table for Means for 85 wt.% rHDPE + 15 wt.% RH

Level	Heater 1	Heater 2	Screw speed	Roller speed
1	1.630	1.777	1.753	1.723
2	1.783	1.680	1.753	1.710
3	1.740	1.697	1.647	1.720
Delta	0.153	0.097	0.107	0.013
Rank	1	3	2	4

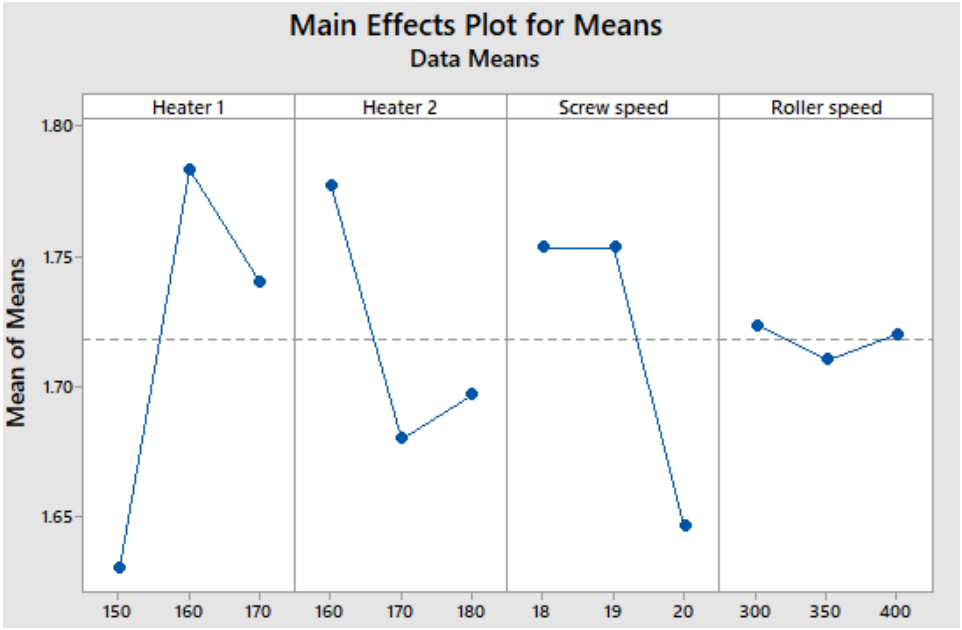

Figure 4.9: Main Effect Plot for Means – 85 wt.% rHDPE + 15 wt.% RH

For 100 wt.% recycled high-density polyethylene, the predicted response was 1.71 mm, which was experimentally validated to 1.73 mm. The difference between the predicted and the experimental was due to the fact that it is difficult to replicate the ideal conditions of a simulation environment. Regarding the biofilaments, the average diameter was 1.74 mm with a standard deviation of 0.013 mm for biofilaments up to 15 wt.% of rice husks. For higher rice husk compositions that required the use of a compatibilizer—namely 20 %, 25 %, 30 %, and 35 wt.% of rice husks—the average diameter was 1.56 mm with a standard deviation of 0.066 mm.

It can be concluded that organic fillers, such as rice husk waste, increase the viscosity of biocomposites, thereby reducing the material's flowability. The heating temperature of the biofilaments has the most significant effect on the resulting biofilament's diameter because heating influences the melting of the biocomposite, which lowers its viscosity. The addition of organic fillers changes the thermal and rheological behavior of the biocomposites due to their lower thermal conductivity compared with that of the main polymer matrix. This causes uneven heating or reduced heat transfer, resulting in decreased polymer elasticity. Therefore, maintaining consistency in filament diameter requires optimizing the main process parameters, which are heating temperature, roller/screw speed, and filler ratio.

4.4 Characterization of Biofilaments

By printing samples, the biofilaments were characterized to determine mechanical, thermal, morphological, and biodegradability properties. A minimum of 3 samples were printed for characterization, and the average was determined.

4.4.1 Fused Filament Fabrication of Developed Biofilaments

Consistent biofilament extrusion from the FFF printer's nozzle, resulting in fully completed prints, served as the success criterion for the printability assessment. The printability of tensile test samples made from the developed biofilaments was successful

up to a 30 % rice husk filler content. Subsequently, nozzle clogging occurred, affecting printability. This necessitated changing the printer's nozzle from 0.4 mm to 0.6 mm. The printed tensile samples from the developed biofilaments are shown in Figure 4.10. Material deposition on the print bed remained highly consistent up to 15 wt.% rice husk filler. Beyond this percentage, inconsistencies in material extrusion were observed, resulting in surface pores on the samples.

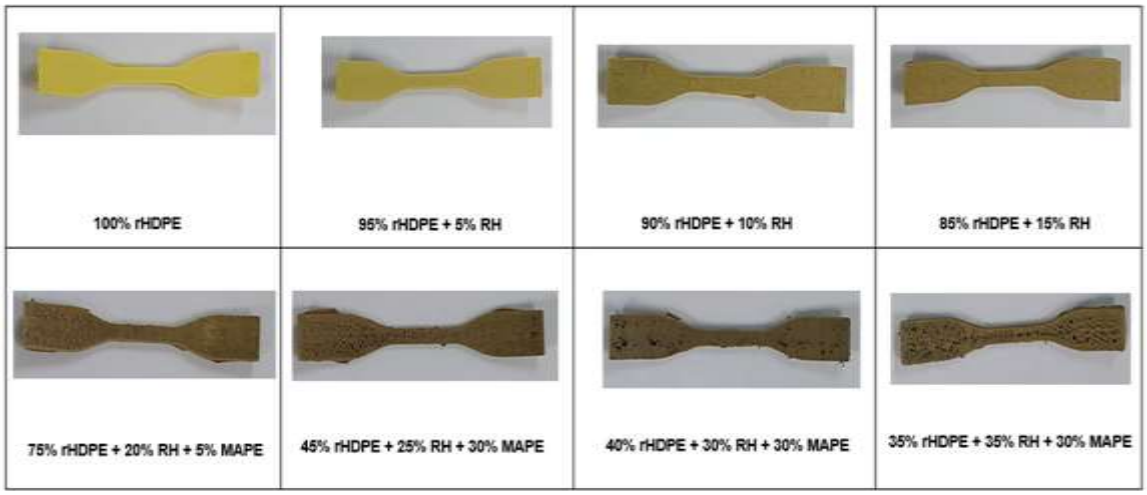

Figure 4.10: Printed Tensile Test Sample

The extrusion or nozzle temperature, printing speed, nozzle diameter, and layer thickness influenced the printability of the biofilament. The choice of extrusion temperature was based on literature regarding the biofilament matrix (Schirmeister et al., 2019). A smooth flow of extruded filament was achieved at 200°C for pure recycled high-density polyethylene. For higher percentages of rice husk filler, the temperature had to be increased to maintain a smooth flow. The biofilament with 30 % rice husks was printed at 240°C. The temperature could not be increased above 240 °C because fumes were released from the print-head, indicating degradation of the biofilaments above 240 °C. Similarly, at 20 wt.% rice husks in the biofilament, required a nozzle change from 0.4 mm to 0.6 mm to address nozzle clogging.

A printing speed of 45 mm/s was identified as the optimal to achieve good printability. Although biofilament fabrication was successful with rice husk filler at up to 35%, this filament could not be printed due to difficulties in material extrusion. The high organic filler content in the polymer matrix caused nozzle clogging because the particles were unable to flow through the nozzle. This challenge was caused by the higher viscosity of the melted biofilament and the weak interfacial adhesion between the organic filler and the polymer matrix.

Hence, consistent material extrusion, resulting in complete prints, was achieved with biofilaments containing up to 30% rice husk filler. This was an improvement compared to previous studies (Koffi et al., 2022; Tao et al., 2017).

4.4.2 Mechanical Properties of the Bioplastics

The mechanical properties of the printed parts studied included tensile, flexural, and compressive properties, as presented in Figures 4.11 – 4.14. The tensile properties included maximum tensile strength (maximum stress), maximum tensile strain, and tensile elastic modulus.

The pure rHDPE biofilament had a tensile elastic modulus of 159 MPa, with a standard deviation of 13 MPa. It gradually decreased with the addition of rice husk filler, reaching 121 MPa for the biofilament containing 15 wt.% rice husks. Adding the compatibilizer to the biofilaments with rice husk content greater than 20 wt.% led to a notable increase in the tensile elastic modulus, reaching 136 MPa for the biofilament with 20 wt.% rice husks. This value decreased to 129 MPa for the biofilament with 30wt.% rice husks.

The compatibilizer enhanced interfacial adhesion between the polymer matrix and fiber particles, thereby improving stress transfer. The tensile strength ranged from 9 MPa to 24 MPa (with a standard deviation of 1.32 MPa), with the highest strength observed in 100 wt.% recycled high-density polyethylene, decreasing with the addition of rice husk filler.

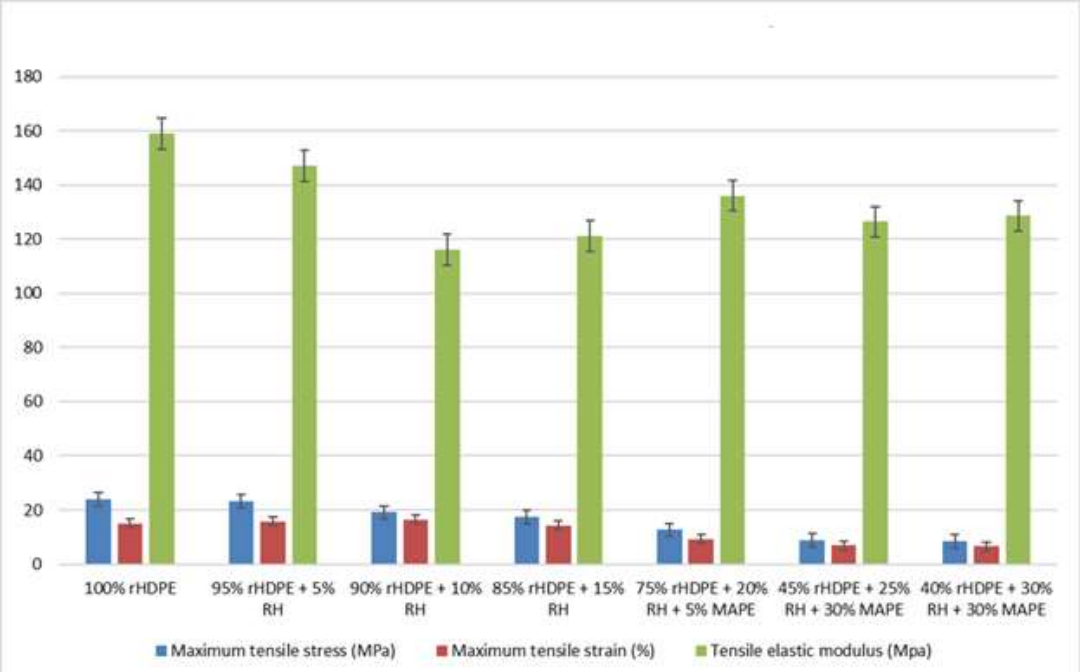

Figure 4.11: Mechanical Properties of the Biofilaments

Figure 4.12 displays the stress-strain curves. Although there was a slight decrease in tensile properties, the addition of short-fiber rice husk fillers enhanced printing directionality and improved biodegradability, as explained in later sections.

Short-fiber fillers are randomly oriented in the polymer matrix because their low aspect ratio limits energy transfer when the material is under load, leading to a decrease in mechanical strength. Regarding applications, the mechanical property values fell within the range of virgin high-density polyethylene and could be used for non-load-bearing applications such as food packaging, casings, and medical devices in biomedical applications.

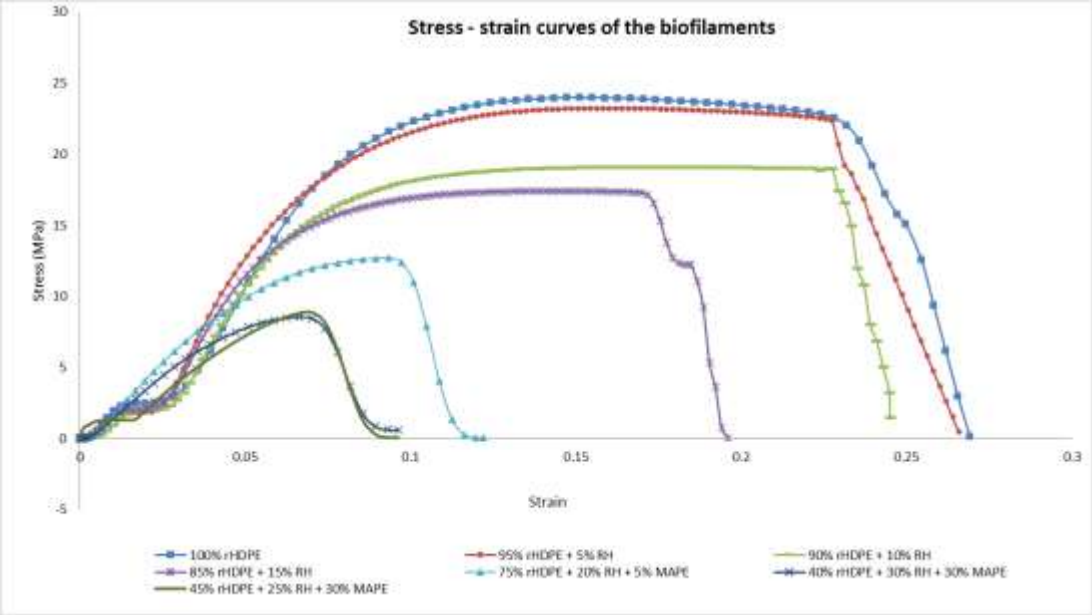

Figure 4.12: Stress-Strain Curves of the Biofilaments

Regarding flexural properties, the biofilament with the highest amount of rice husk filler had a flexural modulus of 87 MPa, compared to 301 MPa for the pure recycled high-density polyethylene filament, as seen in Figure 4.13. The maximum flexural strength decreased from 21 MPa to 5 MPa with the addition of rice husk filler.

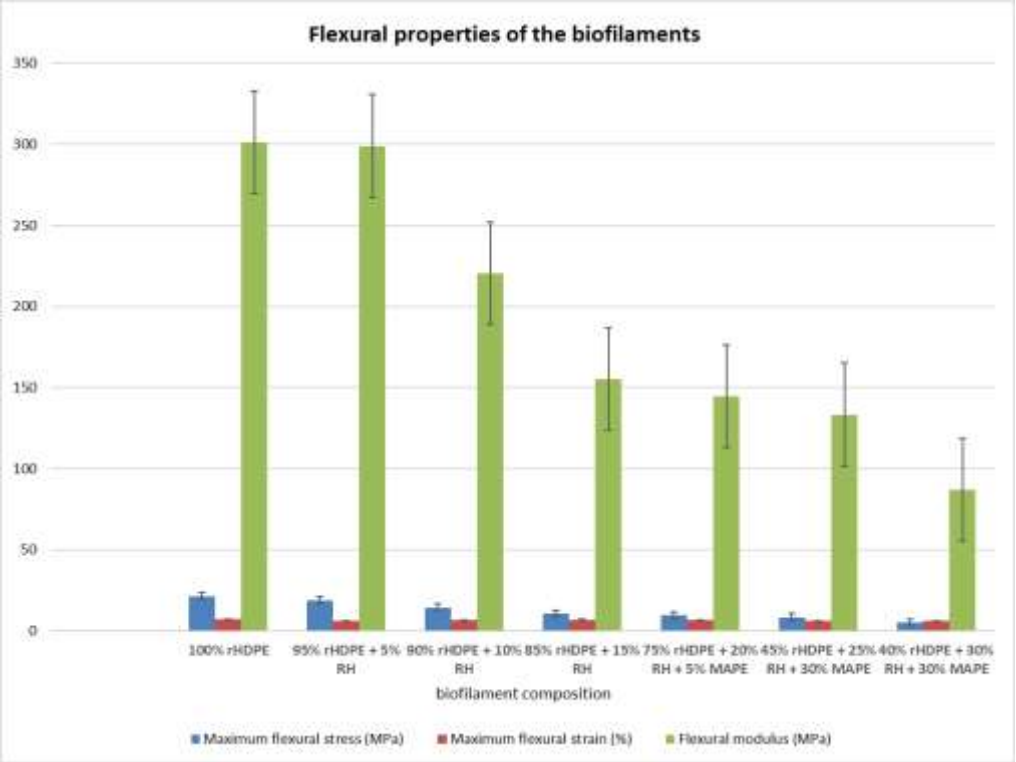

Figure 4.13: Flexural Properties of the Biofilaments

The highest compression stress was for the 100% rHDPE at 18.89 MPa. This value gradually decreased to 5.34 MPa for the biofilament containing 30% rice husks, as shown in Figure 4.14.

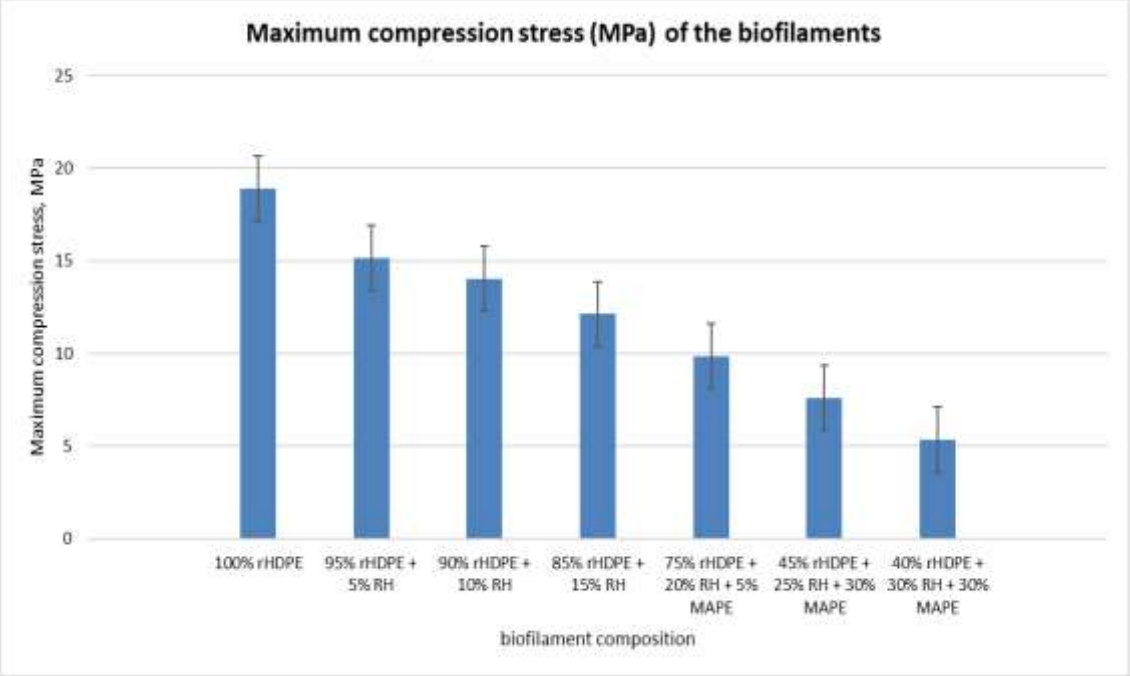

Figure 4.14: Maximum Compression Stress of the Biofilaments

The decrease in mechanical properties is due to poor interfacial bonding between the hydrophobic polymer and the hydrophilic rice husk fibers, as well as thermal degradation of the fibers during extrusion. Rice husk fibers can be made hydrophobic through heat treatment, thereby enhancing interfacial adhesion between the polymer and the fibers. The stress can be transferred smoothly between the two faces, resulting in improved tensile strength and flexural properties (Harper & Wolcott, 2004; T. C. Yang et al., 2017).

Several surface modifications that can be applied to fibers to improve their interfacial adhesion with polymers have been introduced in (Han et al., 2023) . These include chemical oxidation treatment, surface coating modification, plasma treatment, irradiation surface treatment, and corona discharge treatment.

4.4.3 Thermal Properties of the Bioplastics

Thermal analysis evaluated the properties of the developed biofilaments, including melting temperatures (T_m), glass transition temperatures (T_g), enthalpy, and crystallinity (%).

A decrease in crystallinity from 54.91% to 43.45% was observed with the addition of rice husk filler, resulting in reduced mobility of the polymer chains, as shown in Table 4.5 and Figure 4.15.

The values presented in Table 4.5 were from the Star e-DB V.17 software used in DSC. This led to greater water absorption, thereby enhancing biodegradation. The reduction in crystallinity also improved the biofilament's thermal shrinkage. (D. Yang et al., 2021).

A decrease in enthalpy was observed, as shown in Figure 4.16, with the addition of rice husk filler, indicating that less energy was required to melt the biofilament. Adding the compatibilizer, maleic anhydride-functionalized polyethylene, decreased the brittleness of biocomposites due to their low molecular weight. The compatibilizer, at room temperature, maintains a free state between the polymer molecules, thus increasing the mobility of the polymer chains (El-Hadi, 2014). Raising the temperature further enhances the mobility, which improves the processability of the biofilament during its development and fused filament fabrication.

Table 4.5: Thermal Properties of the Biofilaments

Biocomposite composition	Crystallinity (%)	Enthalpy at 100% (J/g)	Glass transition (midpoint ASTM)	Onset Tm (°C)	Peak Tm (°C)
100% rHDPE	54.91	2836.70	50.06	120.83	133.26
95% rHDPE + 5% RH	48.16	2731.06	50.17	121.4	131.43
90% rHDPE + 10% RH	45.98	2629.64	50.00	121.79	132.77
85% rHDPE + 15% RH	45.22	2124.71	50.80	125.98	133.85
75% rHDPE + 20% RH + 5% MAPE	45.35	1097.69	123.42	123.29	130.74
45% rHDPE + 25% RH + 30% MAPE	37.70	984.16	121.27	120.79	131.05
40% rHDPE + 30% RH + 30% MAPE	45.57	1579.46	120.17	119.80	128.84
35% rHDPE + 35% RH + 30% MAPE	43.45	1255.74	120.84	120.37	130.73

The glass transition temperature defines the temperature range at which biofilaments can be extruded and fused into layers, as illustrated in Figure 4.17. If the heating temperature of the biofilament were too low, it would not flow properly, resulting in prints that are weak and brittle. If it is too high, the material would degrade and produce surfaces with poor adhesion. Slower cooling rates increase the glass transition temperature, while faster cooling rates decrease it. This is because slower cooling allows molecular chains more time to align and form stronger bonds, raising the glass transition temperature.

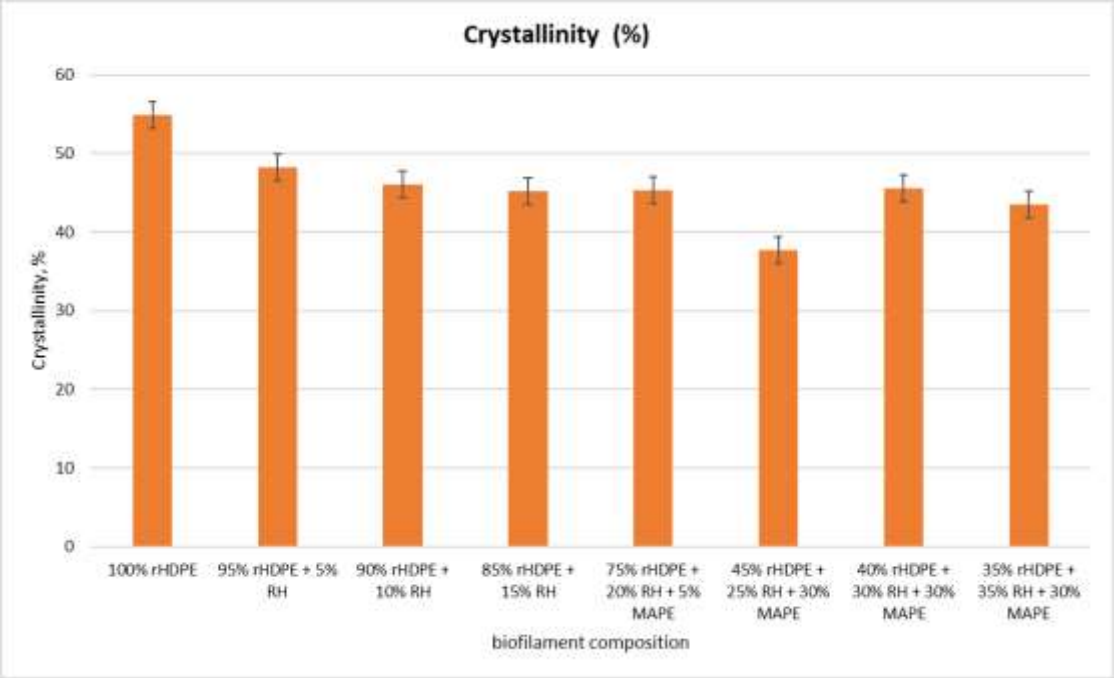

Figure 4.15: Crystallinity of the Developed Biofilaments

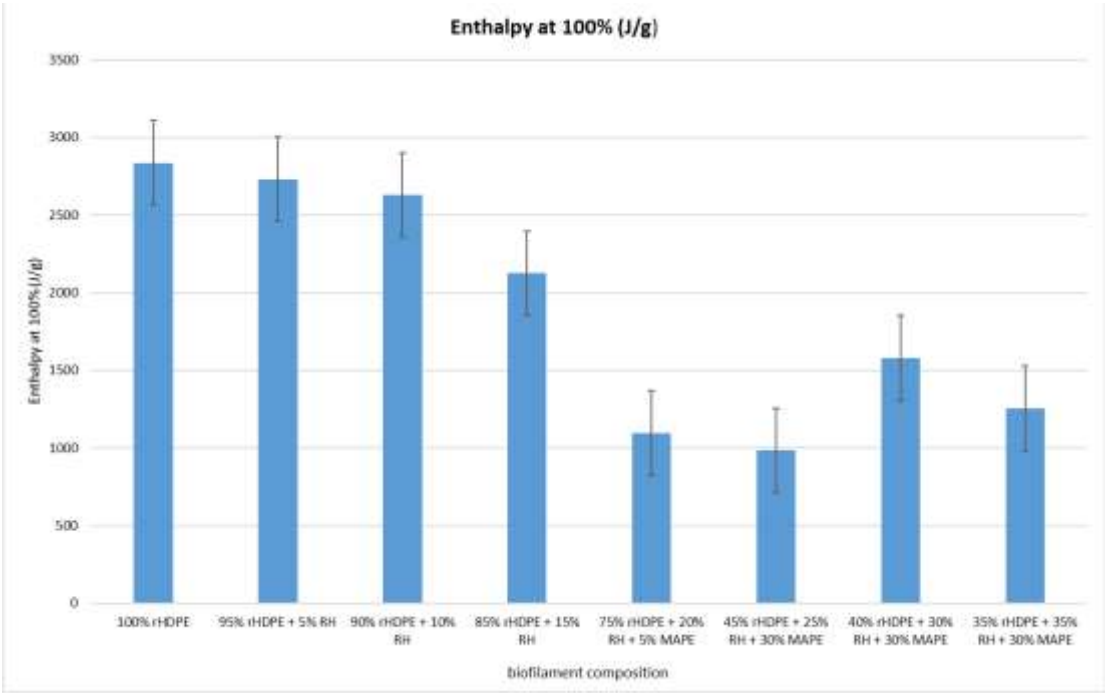

Figure 4.16: Enthalpy of the Developed Biofilaments

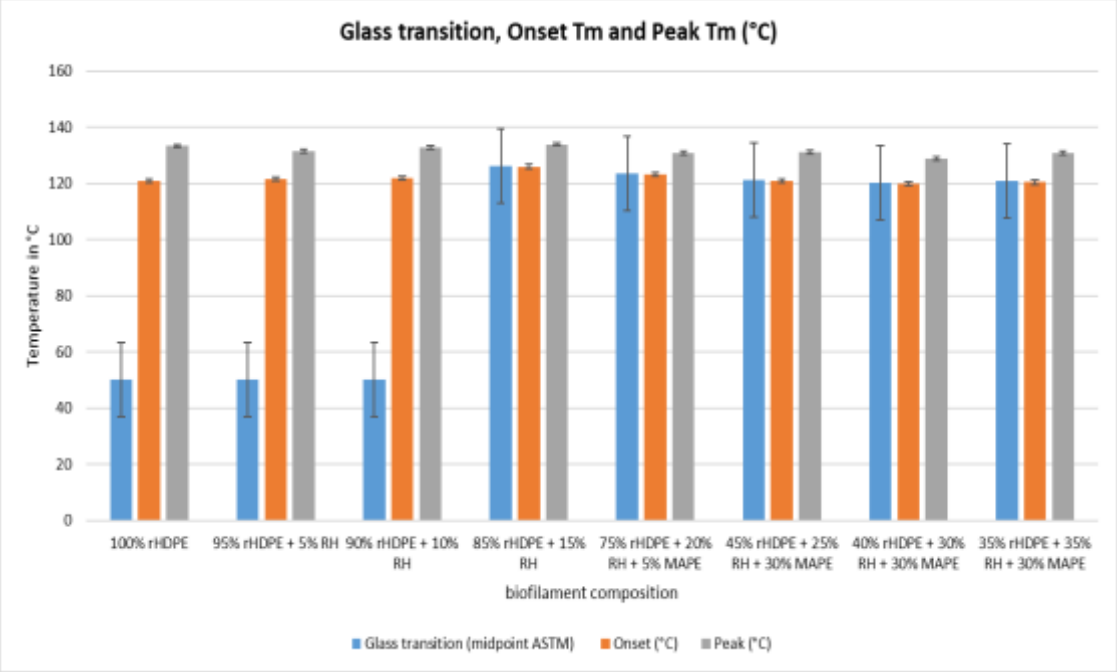

Figure 4.17: Glass Transition Temperature, Onset of Melting, and Peak Melting Temperature

4.4.4 Morphological Properties of the Bioplastics

The first part of the morphology analysis was conducted on the external surfaces of the biofilaments and their cross-section, as shown in Figure 4.18.

The 100 wt. % recycled high-density polyethylene displayed a smooth, non-porous external surface, ensuring easy printability without interruptions. During printing, material extrusion was consistent with no instances of nozzle clogging. However, warping of printed samples was evident due to the material's significant thermal shrinkage and difficulty in sticking to the printer's build plate.

One method that has been reported for addressing these issues is blending polyethylene with short fibers at levels between 10 wt.% and 30 wt.%, along with coupling agents (Koffi et al., 2022). In this study, the addition of rice husks as filler significantly reduced

warping and thermal shrinkage. This was confirmed through the measurement of the samples' dimensions, which were compared with those of the computer-aided design.

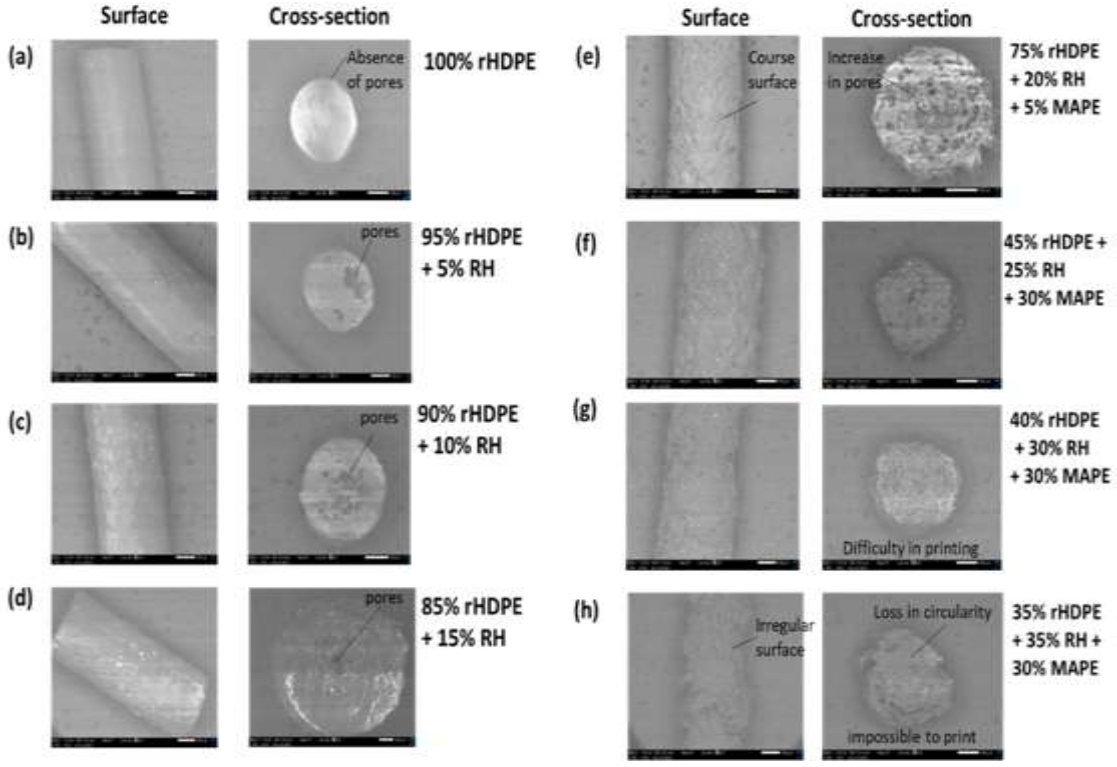

Figure 4.18: SEM Images of the Biofilaments' External Surface and Cross-Section

To address the adhesion issue on the print bed, a slight modification was made by adding a polypropylene print sheet to the print bed. An increase in rice husk filler from 15 wt.% to 35 wt.% caused the external and cross-sectional morphologies to become coarser, as shown in Figures 4.18 e - h. There was also a rise in pore presence and a decrease in filament circularity, which affected printability.

The second stage of the morphology analysis examined the internal microstructure of the fractured tensile samples, revealing filler dispersion and layer formation during printing, as shown in Figure 4.19. The scale was 500 µm with a scan magnification of x27. Uniform printing layers demonstrated consistent material extrusion during printing

(Figure 4.19 a.). Adding 5 wt.% Rice husks in the biocomposite resulted in sparse filler dispersion, leading to pore formation in the polymer matrix (Figure 4.19 b).

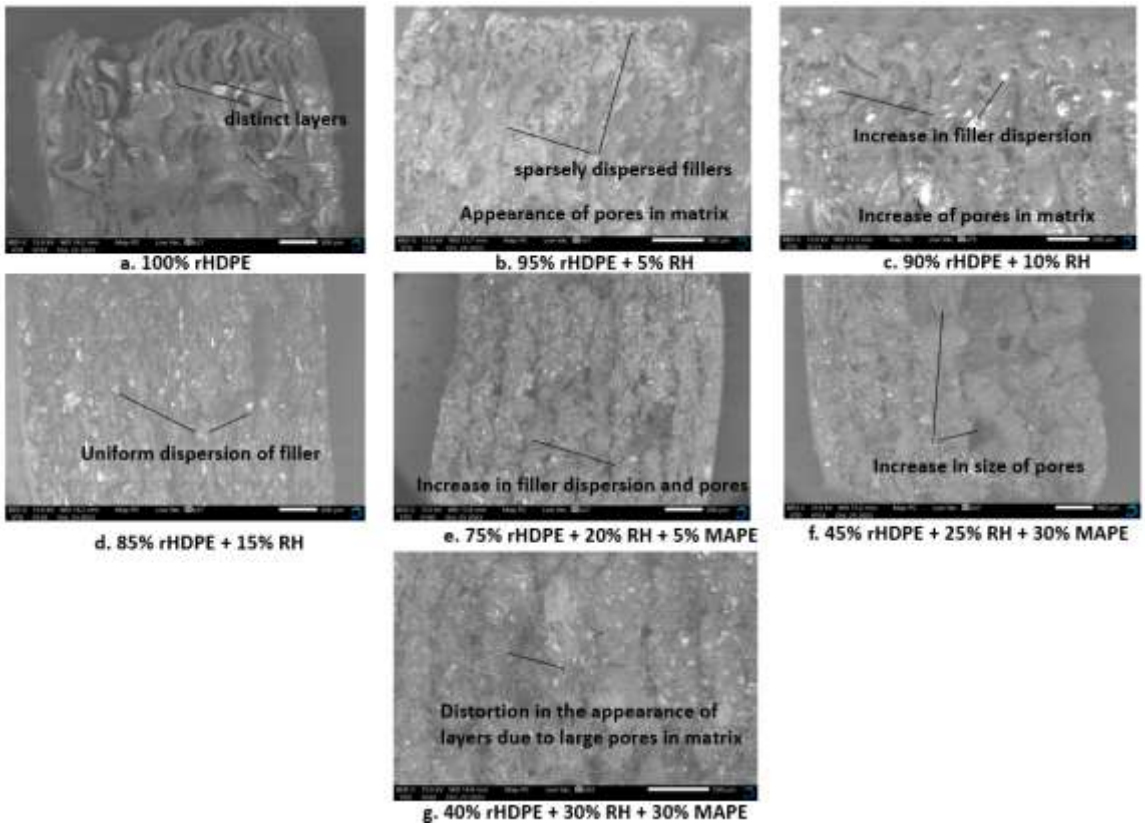

Figure 4.19: SEM Images of the Fractured Tensile Sample

Increasing the rice husk content to 10 wt.% and then to 15 wt.% resulted in a relatively good dispersion of the rice husk filler in the polymer matrix. Although pores were evident in the matrix, the biocomposite's printability improved, resulting in reduced warpage of the printed part.

At 20 wt. %, the addition of rice husks in the biocomposite necessitated the incorporation of a compatibilizer, maleic anhydride-functionalized polyethylene, which improved material flowability and enhanced adhesion between the recycled high-density polyethylene and the rice husk filler. There was also a reduction in pores, as shown in Figure 4.19 e. Above 20 wt.% of the rice husk filler, dispersion improved further;

however, a significant increase in pores was observed, as shown in Figures 4.19 f - g. At this composition, the mechanical properties of the developed biocomposite were compromised. Although printability was successful up to 30 wt.%, the material extrusion was inconsistent, causing dimensional loss in the printed part.

The degree of filler dispersion in the polymer matrix depends on a number of processing parameters, including the shear rate during mixing, interfacial interactions, and the viscosity ratio of the blend components (Utracki, 2002). In most blend systems, the dispersed phase comprises the minor component, while the continuous phase comprises the major component. However, phase inversion can happen in some compositions where the phases take on opposite roles. This occurrence could happen when polymers are present at high loadings of the minor phase or in roughly equal concentrations.

In this study, the interfacial interactions influenced the degree of dispersion. The polymer matrix and the filler had different properties, resulting in weak interactions. This was enhanced by adding maleic anhydride functionalized polyethylene, which improved interactions and increased dispersion during melt mixing. Melt mixing can generate a variety of morphologies, including spherical, co-continuous, lamellar, and fibrillar structures.

From the microscopic images, co-continuous morphologies were observed during the melt mixing of the RH filler and the rHDPE polymer. In co-continuous morphologies, the networks of both phases interpenetrate. This structure is especially beneficial because it allows both components to fully contribute to the properties of the blend, resulting in improvements (Imre et al., 2019).

4.4.5 Surface Roughness Properties of the Bioplastics

The roughness parameters were highest in the biofilament with the greatest amount of RH filler and lowest in the filament made of 100% rHDPE, as presented in Figure 4.20. The mean roughness depth, Rz, was the most prominent roughness parameter, which

increased with the amount of rice husk filler. The enlarged graph of the roughness average, denoted as Ra, shows that the highest value was in the biocomposite with the highest rice husk filler content, Figure 4.21. Although fiber reinforcements in filaments can enhance the strength of a 3D-printed part, their rough fiber surfaces and inadequate fiber-matrix interphase can sometimes lead to voids. These voids may also increase the surface roughness of the filaments.

The higher the roughness parameter, the more difficult it is to print with the material. Rz is always higher than Ra and Rq since it is the mean roughness depth, Ra is the roughness average, and Rq is the root mean square roughness. The recommended value should be less than 0.66 µm. Therefore, it is important to minimize roughness values through surface treatment processes (Fadillah et al., 2023). Surface treatment processes are recommended to improve the surface roughness of 3D printing filament, which subsequently improves printability.

Compatibilization is one method to address these challenges by physically or chemically modifying interfacial interactions, thereby creating uniform mixtures, stable microstructures, and a synergistic combination of the complementary qualities of the biopolymers(Fredi & Dorigato, 2023; Utracki, 2002). This study employed maleic anhydride-functionalized polyethylene as a compatibilizer to reduce interfacial tension, thereby enhancing interfacial adhesion between phases and maintaining a fine morphology against coarsening. In other cases, adding macromolecular ‘surfactants’ easily lowers interfacial tension and produces finer dispersed phases. To keep a fine morphology and enable effective stress transfer, improving adhesion in the solid state is more crucial. (El-Hadi, 2014).

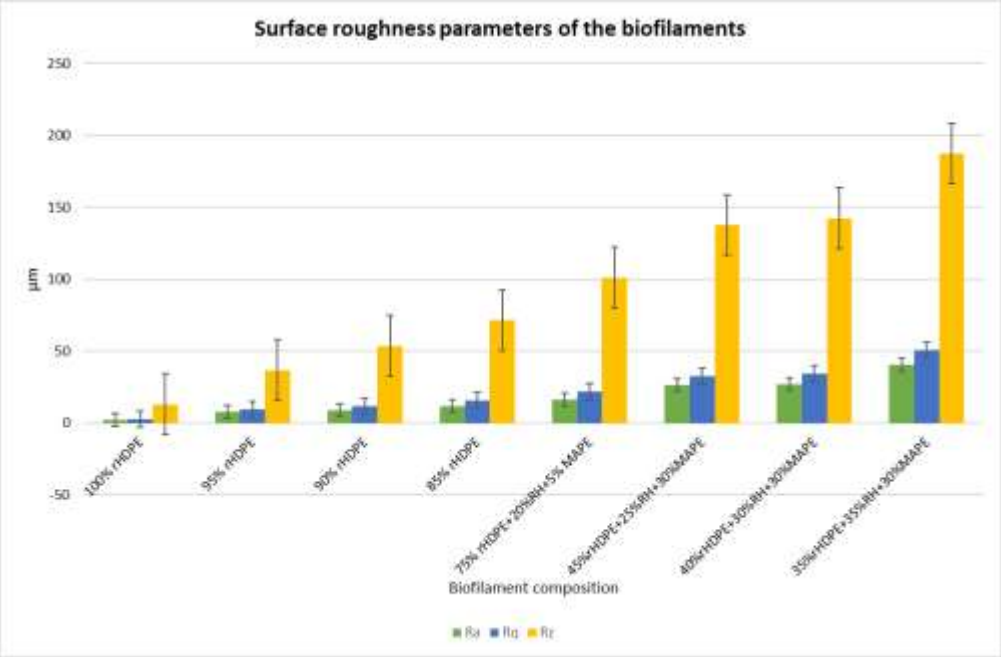

Figure 4.20: Surface Roughness of the Developed Biofilaments

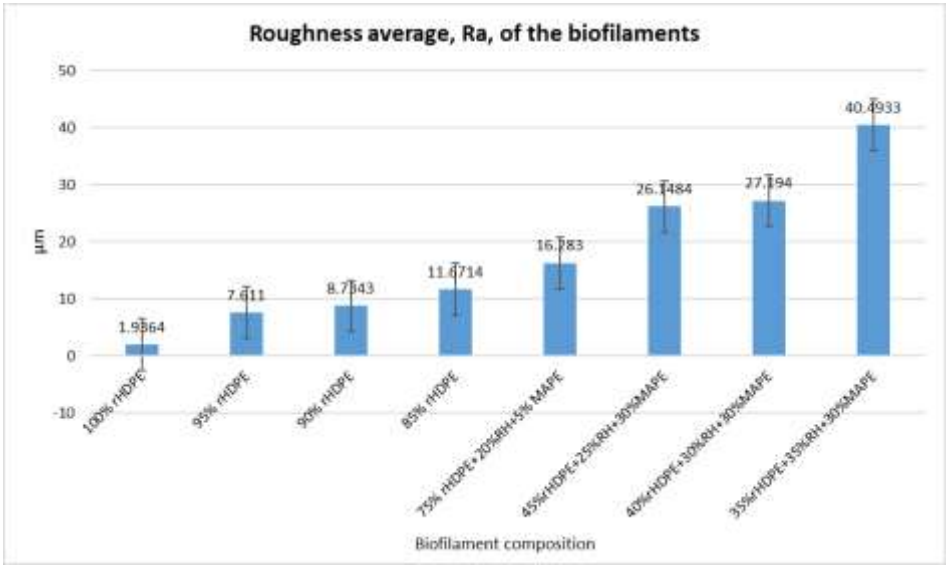

Figure 4.21: Roughness average (Ra) of the Developed Biofilaments

4.4.6 Fourier Transform Infrared Spectroscopy Analysis

The Fourier transform infrared (FTIR) spectroscopy was conducted to determine the chemical composition of the developed biofilaments. Figure 4.22 displays the FTIR spectrum of the biofilaments.

The first prominent peak was observed between 1400 cm^{-1} and 1500 cm^{-1}, indicating the presence of the methylene functional group in the biofilaments (Donelli et al., 2010). The presence of rice husks, an organic compound, was observed at the second peak between 1000 cm^{-1} and 1200 $cm^{-1,}$ indicating the presence of carbonyl and carbo-hydroxyl functional groups (Hidayat et al., 2023). The third and final peak appeared between 600 cm^{-1} and 800 cm^{-1}, indicating the presence of methanediyl in the polyethylene group (Mouallif et al., 2024.).

The absorbance units increased with higher rice rusk content, indicating greater energy consumption and deformation of carbonyl functional groups related to the organic matter in the rice husks. Different bands for various functional groups have been reported by different researchers, as shown in Table 4.6. This analysis verified the presence of specific functional groups in the developed biocomposite and the anticipated deformations. The addition of rice husk filler resulted in a spectrum that confirmed the decline in mechanical properties observed during mechanical characterization.

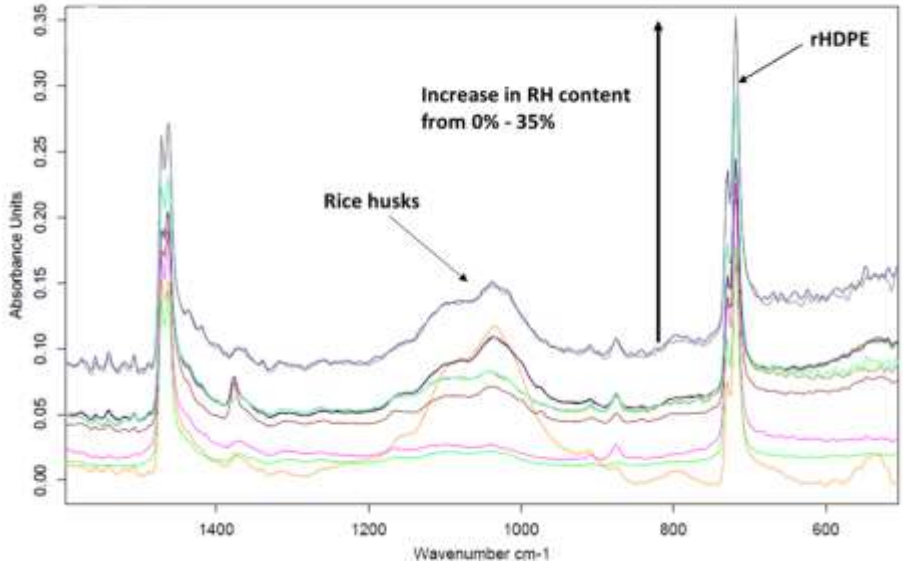

Figure 4.22: FTIR Spectrum of the Developed Biofilaments

Table 4.6: FTIR Wave Number for Various Functional Groups

Wave number (cm^{-1})	Functional groups	Type of vibration	Ref.
700 - 800	CH_2	Rocking deformation	(Mouallif et al., 2024)
1000 - 1200	C=O	stretching vibrations	(Donelli et al., 2010)
1400 – 1480	$-CH_2-$	Bending deformation	(Donelli et al., 2010)
885, 815, 750	C-H	bending	(Keiluweit et al., 2024)
2500 - 3700	O-H	Water molecules	(Hidayat et al., 2023)
1700 - 1500	C=C	Stretching vibrations	(Keiluweit et al., 2024)

4.4.7 Biodegradation Properties of the Bioplastics

The biodegradability rate was demonstrated by the reduction in sample mass after four weeks of burial in soil. The external surfaces of the samples degraded faster after contact with humid soil than their internal structures. The initial samples used to initiate degradation were those containing the compatibilizer, which demonstrated its facilitation

of the degradation process. The biodegradability was highest in samples containing the highest percentages of rice husks and maleic anhydride functionalized polyethylene, attaining a mass loss of 10% of the original mass.

This was due to the matrix's increased organic filler, which improved biodegradability, and its percentage decrease in the primary polymer. It was observed that incorporating maleic anhydride-functionalized polyethylene into the biocomposite's constituents improved interfacial adhesion, enhanced workability, and encouraged biodegradation.

The pure recycled high-density polyethylene degraded at a minimal rate, losing only 0.55% of its mass. This negligible change in mass resulted from the lack of organic content in the pure recycled high-density polyethylene. Additionally, the impurities in the recycled high-density polyethylene, which is known to be chemically inert and to have a high hydrophobicity, may be the cause of the slight mass change. This makes it resistant to the action of microorganisms' enzymes and acids.

Incorporating organic matter, that is, the rice husks, into the recycled high-density polyethylene matrix enabled biodegradation to occur, as shown in Table 4.7.

Table 4.7: Mass Decrement of Biocomposites during Biodegradability Analysis

Composition:	Mass decrement (%)						
rHDPE/RH/MAPE (%)	2 weeks	4 weeks	8 weeks	12 weeks	16 weeks	20 weeks	24 weeks
100 / 0 / 0	0	0	0	0	0	0.17	0.55
95 / 5 / 0	0	0	0.30	0.40	0.68	0.71	0.78
90 / 10 / 0	0	0	0.60	1.01	1.43	1.52	1.55
85 / 15 / 0	0	0	0.91	1.11	2.09	3.11	3.67
75 / 20 / 5	0	0.41	1.21	2.46	3.66	4.68	5.43
45 / 25 / 30	0	0.80	2.04	3.63	6.19	7.84	8.22
40 / 30 / 30	0	1.03	2.46	4.38	6.82	8.23	10.54

Microorganisms and oxygen reacted with the biocomposites during biodegradation, releasing extracellular enzymes that broke down the molecules into carbon dioxide and water as byproducts. The discharge of these byproducts led to a decrease in the mass of the biocomposite. This biodegradability measurement was carried out in accordance with ASTM standard D5988-18, which states that the mass decrement as a function of time of the plastic buried in soil is used to calculate the aerobic biodegradation by measuring the carbon dioxide evolved.

Therefore, during the biodegradability testing in this investigation, the mass loss was tracked. As illustrated in Figure 4.23, a change in the mass and composition of the biocomposites was confirmed by the considerable decrease in the maximum stress and maximum tensile modulus for all samples following the testing period. For instance, during the 24-week course, the tensile modulus of the sample containing 30% rice husks decreased from 128 MPa to 50 MPa, with a standard deviation of 12 MPa. Similarly, its tensile strength decreased from 8.5 MPa to 4.7 MPa, with a 2.45 MPa standard deviation of. This pattern was observed with all the other tested samples. The biodegradation in this study is attributed to the hydrophilic and organic nature of the rice husk filler in the biofilament.

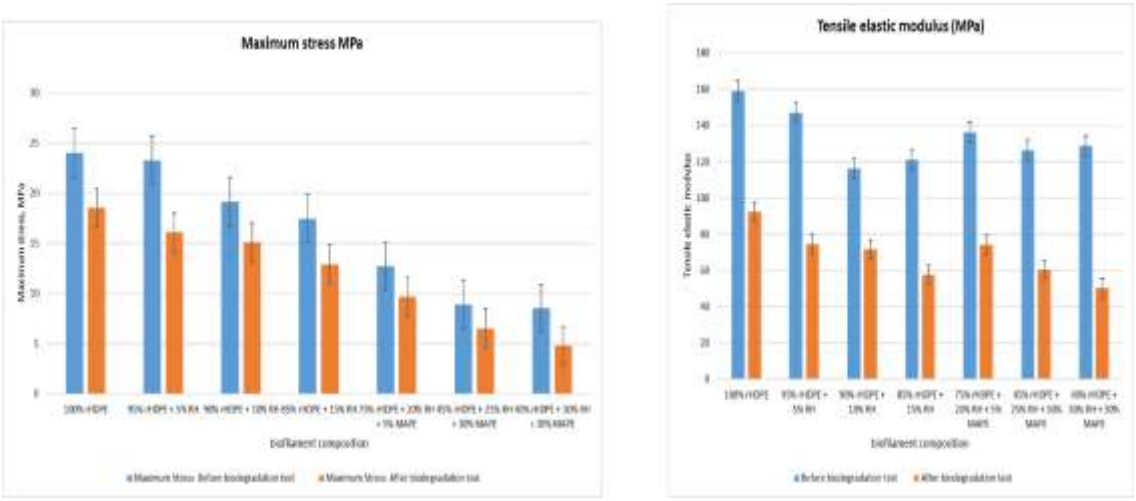

Figure 4.23: Mechanical Properties Before and After Biodegradability

To determine how the moisture content of the produced biofilaments relates to their biodegradability, a moisture analysis was performed. As shown in Figure 4.24, the results demonstrated that the moisture content was directly proportional to the rice husk filler content in the biofilaments. The rate of biodegradability increased with the amount of moisture present. This was because the types of intermolecular interactions in polymer chains determine their biodegradability.

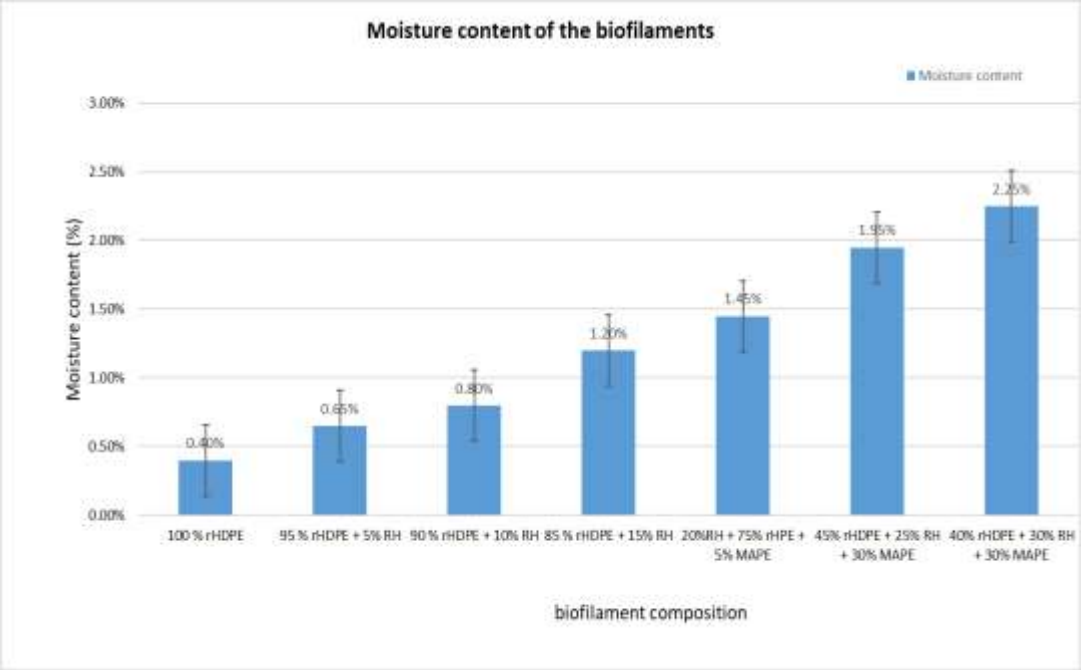

Figure 4.241: Moisture Content in the Biofilament

The presence of polar bonds within a polymer promotes its biodegradation, while non-polar bonds make it non-biodegradable. Using rice husks as a filler in recycled high-density polyethylene caused the biofilaments to become hydrophilic due to the presence of polar bonds. Introducing these polar bonds into the biofilaments' structure allowed them to be hydrolyzed by microorganisms' acids or bases, which broke the bonds and led to degradation (Bisht, 2020).

While polar interactions enhance biodegradation, they can also weaken the bonds between the organic filler and the polymer matrix, decreasing the mechanical strength of the biofilament. This is why excessive moisture absorption in a biofilament is undesirable. For short-term packaging applications where significant strength is not required, such a material could be useful. This analysis shows that adding organic fillers to the polymer matrix is an effective and environmentally friendly way to enhance plastic biodegradation and reduce pollution.

4.5 Simulation Results of the Fused Filament Fabrication Process

A simulation of the printing process was performed on a standard tensile test sample using nine different input parameter combinations, as presented in Section 3.3.3. Residual stresses and warpage were the outputs analyzed, and the results for three different material models are presented in Tables 4.8, 4.9, and 4.10. The plots of warpage and residual stresses of the first experimental run are presented in the subsequent sections.

Minitab software was used in the analysis of the responses, that is, residual stresses and warpage to determine the best parameters. Minitab develops a regression model and then performs the optimization. Equation (4.1) presents the objective function used in Minitab for optimization:

$$\hat{y} = \beta_0 + \sum \beta_i x_i + \sum \beta_{ii} x_i^2 + \sum \beta_{ij} x_i x_j \qquad (4.1)$$

Where:

- $\hat{y}$ = predicted response (what you want to optimize)
- β_0 = intercept
- β_i = linear coefficients
- β_{ii} = quadratic coefficients
- β_{ij} = interaction coefficients
- x_i = factors (extrusion temperature, printing speed, layer height, etc.)

Adding rice husk filler to rHDPE lowered the residual stress from 2.683 MPa to 1.883 MPa on the bioplastic with 15 wt.% RH and reduced warpage from 4.337 mm to 3.656 mm. This improvement resulted from better thermal behavior caused by adding organic filler to the polyethylene matrix, as explained in Section 4.3.4. When the compatibilizer, MAPE, was added, the residual stress decreased to 2.446 MPa from 2.683 MPa. However, warpage slightly increased to 4.518 mm due to the addition of pure MAPE, which contains the polyethylene group.

4.5.1 Warpage and Residual Stress for the 100 wt. % rHDPE

Table 4.8: Residual Stress and Warpage for the 100 wt. % rHDPE

Test	Extrusion Temperature, °C	Bed temperature, °C	Printing Speed, mm/s	Layer height, mm	Warpage,	Residual Stress, MPa
1	210	60	20	0.1	1.368	2.683
2	210	90	30	0.15	1.369	2.684
3	210	120	40	0.2	1.368	2.684
4	220	60	30	0.2	1.448	2.854
5	220	90	40	0.1	1.448	2.853
6	220	120	20	0.15	1.448	2.854
7	230	60	40	0.15	1.527	3.024
8	230	90	20	0.2	1.527	3.024
9	230	120	30	0.1	1.527	3.023

The simulation results of 100 wt.% rHDPE printed at 210 °C, bed temperature of 60 °C, printing speed of 20 mm/s, and layer height of 0.1 mm are illustrated in Figure 4.25.

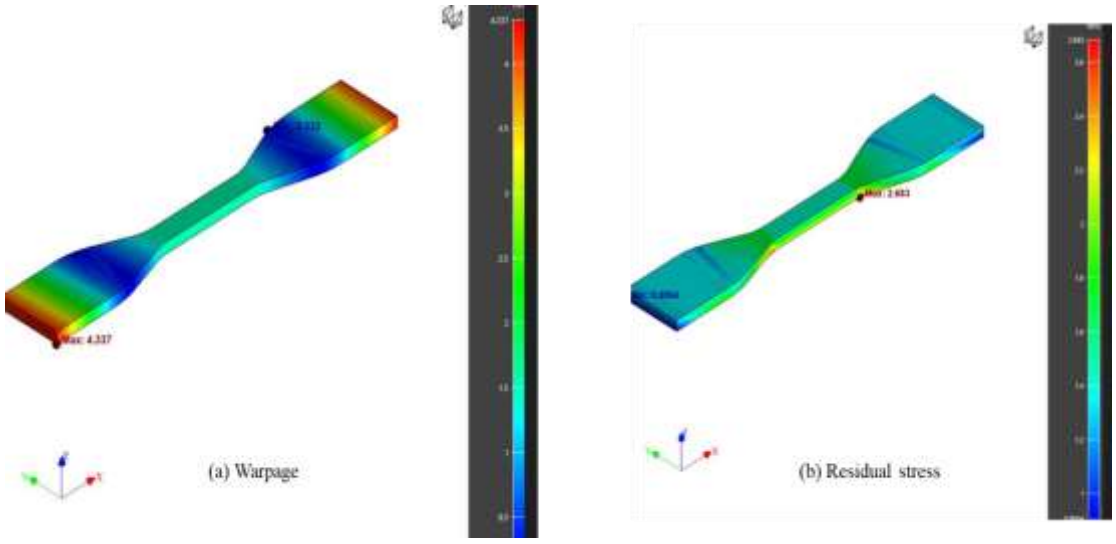

Figure 4.25: Simulation Results of 100 wt.% rHDPE

a. Warpage of 100 wt.% rHDPE

Figure 4.26 shows the "Main effects plot for means and signal-to-noise ratio" for warpage of the 100 wt.% rHDPE. Table 4.9 presents the response table for means, including the rank positioning of all the parameters considered. For the 100wt.% rHDPE, the extrusion temperature had the most significant influence, followed by the other three parameters, all with equal ranks.

Table 4.9: Response Table for Average Warping of the 100% rHDPE

Level	Extrusion Temperature, °C	Bed temperature, °C	Printing Speed, mm/s	Layer height, mm
1	1.368	1.448	1.448	1.448
2	1.448	1.448	1.448	1.448
3	1.527	1.448	1.448	1.448
Delta	0.159	0.000	0.000	0.000
Rank	1	3	3	3

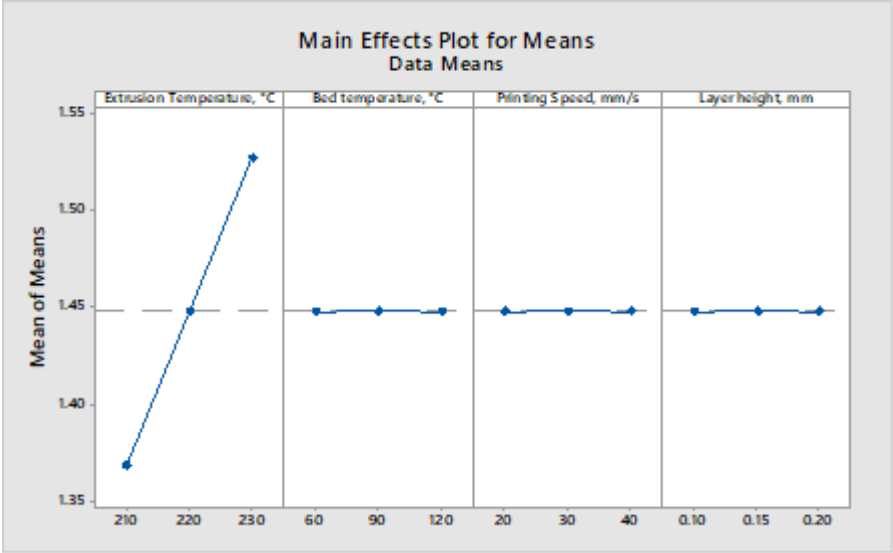

(a)

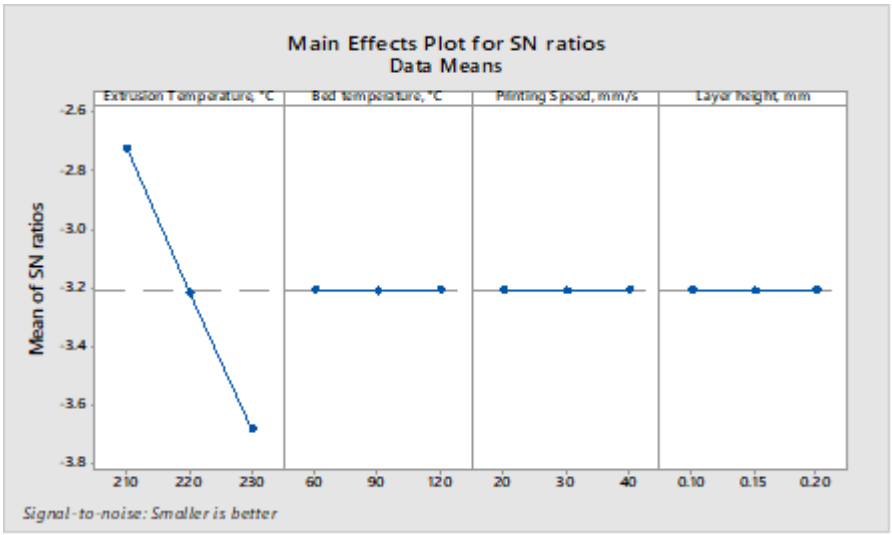

(b)

Figure 4.26: Main Effect Plot for Warpage of 100 wt.% rHDPE (a) Means (b) SN Ratio

Table 4.10: Response Table for Signal-to-Noise Ratios of the 100% rHDPE Warpage

Level	Extrusion Temperature, °C	Bed temperature, C	Printing Speed, mm/s	Layer height, mm
1	-2.724	-3.205	-3.205	-3.205
2	-3.215	-3.207	-3.207	-3.207
3	-3.677	-3.205	-3.205	-3.205
Delta	0.953	0.002	0.002	0.002
Rank	1	3	3	3

From the delta values, the other parameters had very minimal influence on the warpage compared to extrusion temperature. In this study, "the smaller-is-better" was the desired goal for the responses since the aim was to minimize the part warpage. The response table for signal-to-noise ratio is shown in Table 4.10. The lowest value of the signal-to-noise ratio represents the best value selection; hence, the best extrusion temperature was 210 °C.

b. Residual Stresses of 100 wt.% rHDPE

A similar trend is observed in the residual stresses, whereby the extrusion temperature has the most significant effect, as shown in Tables 4.11 and 4.12. The heating and cooling cycles that the printed item undergoes determine how residual stresses develop and accumulate. This is followed by the layer height, which determines the total number of layers required to complete the part and thereby the temperature gradient between layers. Lastly, both the bed temperature and printing speeds had the same effect on the residual stresses, with minimal impact, as illustrated in Figure 4.27. Extrusion temperature was the most significant parameter affecting warpage and residual stresses because it determines how well the biofilament material flows, bonds, and forms a strong structure. The temperature influences most of the material's properties, such as melt viscosity, interfacial adhesion, layer bonding, and void formation.

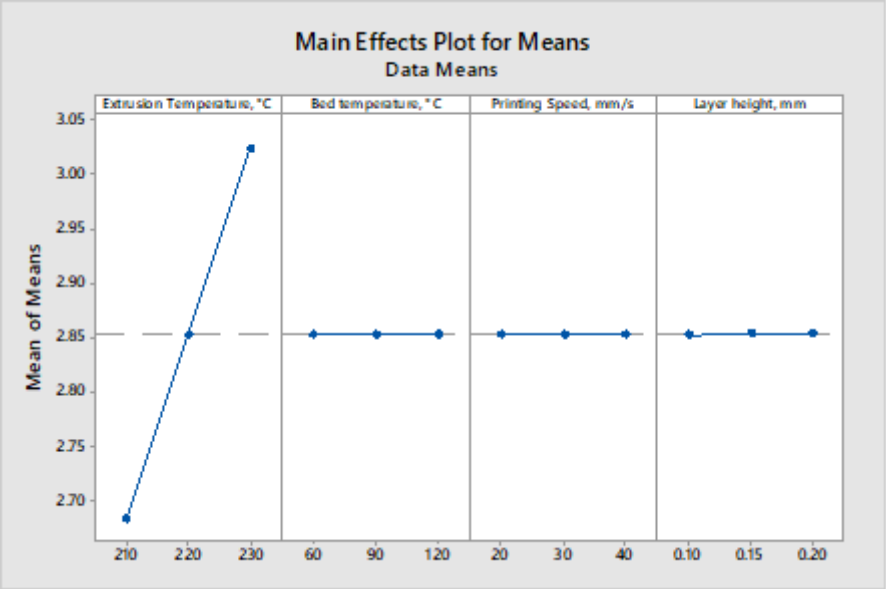

(a)

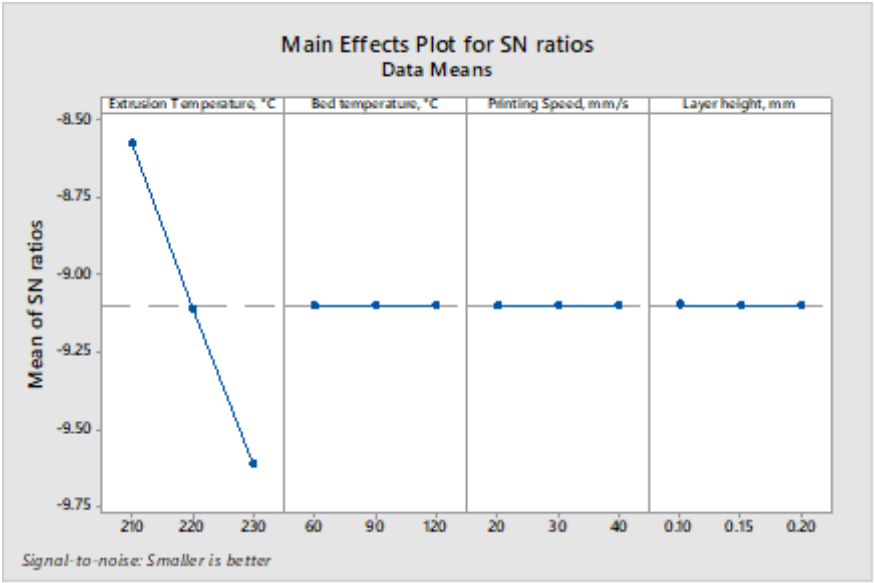

(b)

Figure 4.27: Main Effect Plot for Residual Stresses of 100 wt.% rHDPE (a) Means (b) SN Ratio

Table 4.12 gives the best parameter where the signal-to-noise level has the lowest value. Thus, the best parameter selection to minimize residual stress for the 100 wt.% rHDPE was extrusion temperature of 210 °C, and layer height of 0.1 mm.

Table 4.11: Response Table for Average Residual Stresses of the 100% rHDPE

Level	Extrusion Temperature, °C	Bed temperature, C	Printing Speed, mm/s	Layer height, mm
1	2.684	2.854	2.854	2.853
2	2.854	2.854	2.854	2.854
3	3.024	2.854	2.854	2.854
Delta	0.340	0.000	0.000	0.001
Rank	1	3.5	3.5	2

Table 4.12: Response Table for Signal-to-Noise Ratios of the 100% rHDPE Residual Stresses

Level	Extrusion Temperature, °C	Bed temperature, °C	Printing Speed, mm/s	Layer height, mm
1	-8.575	-9.098	-9.098	-9.096
2	-9.108	-9.098	-9.098	-9.099
3	-9.611	-9.098	-9.098	-9.099
Delta	1.036	0.000	0.000	0.003
Rank	1	3.5	3.5	2

Higher extrusion temperatures result in more residual stress and subsequently warpage because they cause reheating to occur more extensively on the previously deposited layer, leading to higher temperature gradients within the material. Warpage is a direct result of residual stresses, which occur when different sections of the printed part cool at different rates, leading to differences in shrinkage and internal stresses that cause the part to deform.

4.5.2 Warpage and Residual Stress for the 85 wt. % rHDPE + 15 wt.% RH

An improvement in the residual stress and warpage was noted with the 85 wt. % rHDPE and 15 wt.% RH bioplastic. This is attributed to the improvement in thermal behaviour of the biofilament with the addition of filler to the recycled polymer. As shown in Table 4.13 and Figure 4.28, during the first test, the addition of rice husk filler resulted in a decrease in residual stress from 2.683 MPa to 1.883 MPa, representing an improvement of 29.8%. The warpage also decreased from 1.368 to 1.160, for the first experimental run representing an improvement of 15.2 %.

a. Warpage of the 85 wt. % rHDPE and 15 wt.% RH Bioplastic

Figure 4.28 illustrates the simulation results of 85 wt. % rHDPE + 15 wt.% RH bioplastic printed at 210 °C, bed temperature of 60 °C, printing speed of 20 mm/s and layer height of 0.1 mm. Figure 4.29 shows the mean effect plots for the average responses and the signal-to-noise ratio. Table 4.13 tabulates the warpage and the residual stresses for each simulation run. From Table 4.14 and Table 4.15, the “smaller is better” objective is chosen, ranking the extrusion temperature as the most significant parameter, followed by bed temperature, then layer height, and lastly printing speed. The best parameter selection is the one that gives the smallest signal-to-noise ratio. Hence, according to Table 4.14, the best parameters were extrusion temperature of 210 °C, bed temperature of 90 °C, printing speed of 20 mm/s, and layer height of 0.1 mm.

Table 4.13: Residual Stress and Warpage for the 85 wt. % rHDPE + 15 wt.% RH Bioplastic

Test	Extrusion Temperature, °C	Bed Temperature, °C	Printing Speed, mm/s	Layer height, mm	Warpage,	Residual Stress, MPa
1	210	60	20	0.1	1.160	1.883
2	210	90	30	0.15	1.160	1.883
3	210	120	40	0.2	1.160	1.883
4	220	60	30	0.2	1.227	2.004
5	220	90	40	0.1	1.218	2.001
6	220	120	20	0.15	1.227	2.003
7	230	60	40	0.15	1.297	2.120
8	230	90	20	0.2	1.288	2.116
9	230	120	30	0.1	1.289	2.116

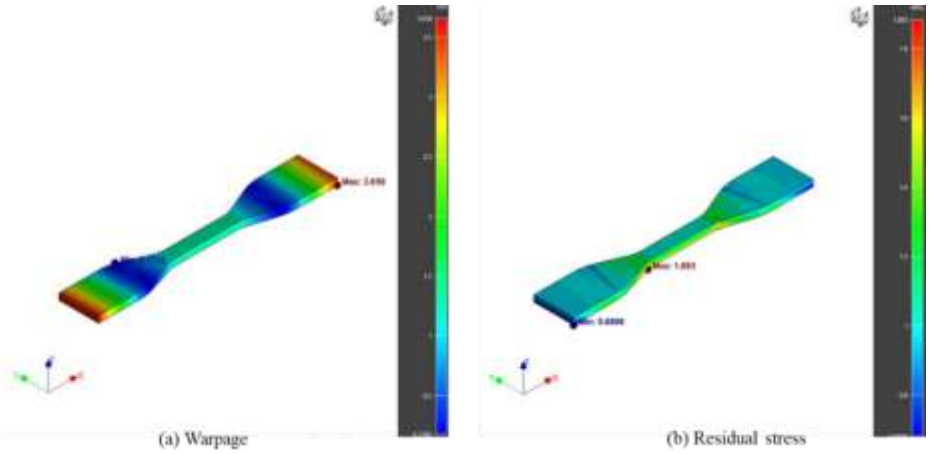

Figure 4.28: Simulation Results of 85 wt. % rHDPE + 15 wt.% RH Bioplastic

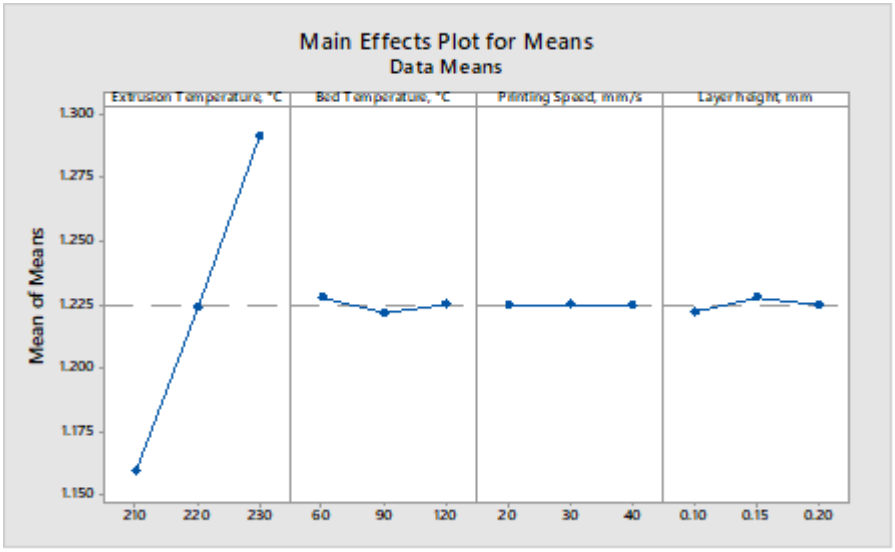

(a)

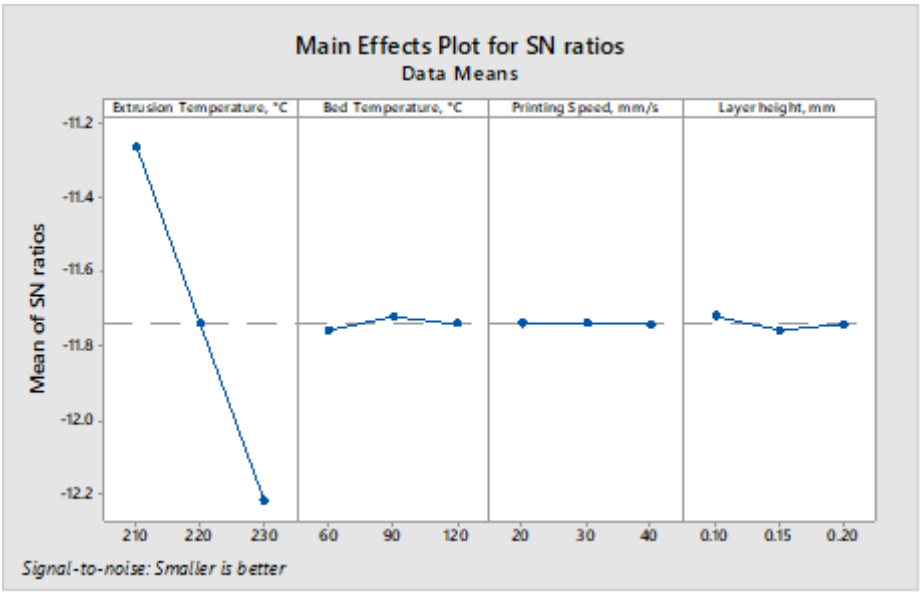

(b)

Figure 4.29: Main Effect Plot for Warpage (a) Means (b) SN Ratio of 85 wt. % rHDPE + 15 wt.% RH Bioplastic.

Table 4.14: Response Table for the Signal-to-Noise Ratio of the 85 wt.% rHDPE + 15 wt.% RH Bioplastic's Warpage

Level	Extrusion Temperature, °C	Bed Temperature, °C	Printing Speed, mm/s	Layer height, mm
1	-1.289	-1.775	-1.755	-1.736
2	-1.756	-1.733	-1.757	-1.775
3	-2.221	-1.757	-1.754	-1.775
Delta	0.932	0.041	0.003	0.039
Rank	1	2	4	3

Table 4.15: Response Table for Average Warpage of the 85 wt. % rHDPE + 15 wt.% RH Bioplastic.

Level	Extrusion Temperature, °C	Bed Temperature, °C	Printing Speed, mm/s	Layer height, mm
1	1.160	1.228	1.225	1.222
2	1.224	1.222	1.225	1.228
3	1.291	1.225	1.225	1.225
Delta	0.131	0.006	0.000	0.006
Rank	1	2	4	3

b. Residual Stresses of the 85 wt. % rHDPE + 15 wt.% RH Bioplastic

Regarding the residual stresses, the extrusion temperature had the most significant impact, as shown in Table 4.16. The bed temperature then followed it, then the layer height, and lastly the printing speed. The bed temperature came second since, with the inclusion of the organic fillers, the adhesion on the bed had to be enhanced by increasing its temperature. Figure 4.30 illustrates the main effect for the average residual stresses and the signal-to-noise ratio. As seen, changes in the temperature lead to very significant changes in the residual stresses. Very high temperatures are undesirable due to the high temperature gradients introduced in the printing layers. From Table 4.17, the best parameters for minimizing the residual stresses were extrusion temperature of 210 °C, bed temperature of 90 °C, printing speed of 20 mm/s, and layer height of 0.1 mm. This was in agreement with the responses for warpage.

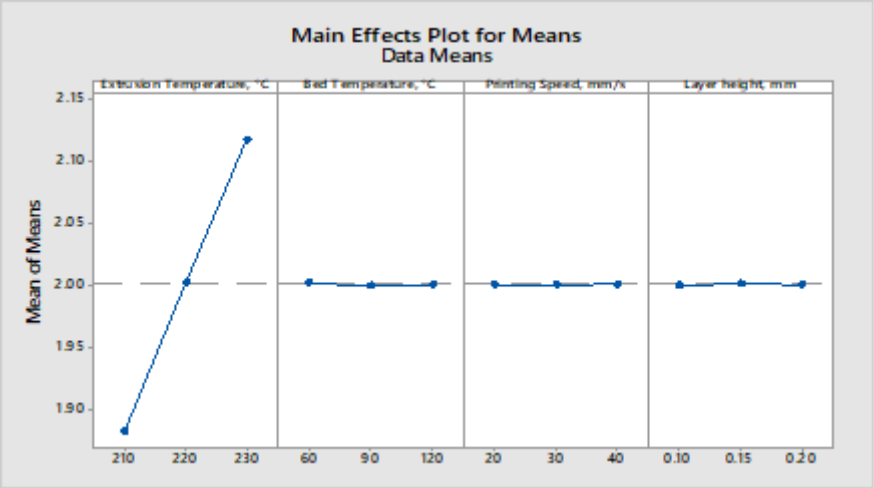

(a)

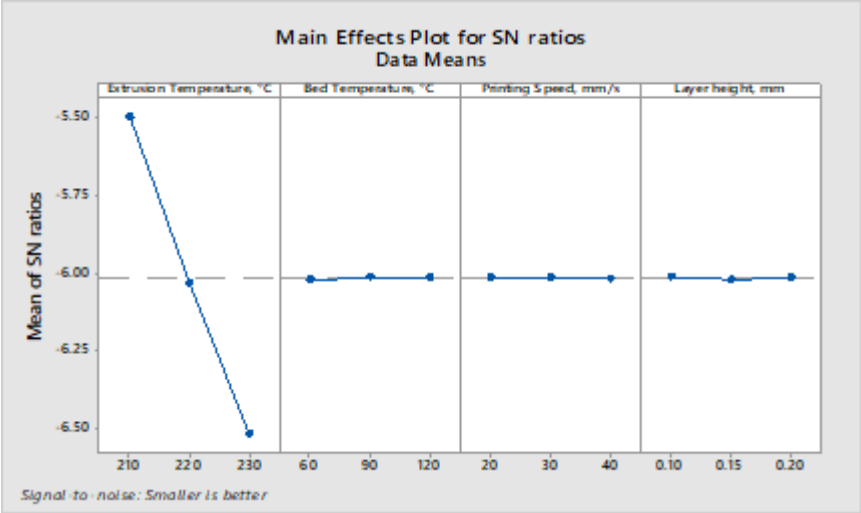

(b)

Figure 4.30: Main Effect Plot for Residual Stresses (a) Means (b) SN Ratio of 85 wt. % rHDPE + 15 wt.% RH Bioplastic

Table 4.16: Response Table for Average Residual Stresses of the 85 wt. % rHDPE + 15 wt.% RH Bioplastic

Level	Extrusion Temperature, °C	Bed Temperature, °C	Printing Speed, mm/s	Layer height, mm
1	1.883	2.002	2.001	2.000
2	2.003	2.000	2.001	2.002
3	2.117	2.001	2.001	2.001
Delta	0.234	0.002	0.001	0.002
Rank	1	2	4	3

Table 4.17: Response Table for Signal-to-Noise Ratios of the 85 wt. % rHDPE + 15 wt.% RH Residual Stresses

Level	Extrusion Temperature, °C	Bed Temperature, °C	Printing Speed, mm/s	Layer height, mm
1	-5.497	-6.021	-6.014	-6.011
2	-6.032	-6.011	-6.015	-6.019
3	-6.516	-6.014	-6.016	-6.015
Delta	1.019	0.010	0.003	0.008
Rank	1	2	4	3

4.5.3 Warpage and Residual Stress for the 40% rHDPE + 30 % RH + 30 % MAPE

The addition of MAPE had the effect of improving the flowability of the bioplastic during extrusion. Likewise, the residual stress was lower than that of the pure rHDPE, decreasing from 2.683 MPa to 2.446 MPa, representing an 8.83% improvement. However, there was a slight increase in warpage, from 4.337 mm to 4.518 mm, representing a 4.2% deterioration, as shown in Table 4.18 and Figure 4.31. Although the use of MAPE at its maximum allowable amount enabled a very high percentage of RH filler (i.e., 30%) to be added to the bioplastic, the net effect was a reduction in mechanical strength and thermal resistance, resulting in a slight increase in warpage.

Ideally, plasticizers, when used in small amounts, reduce residual stresses and warpage by lowering the glass transition temperature and increasing the mobility of polymer

chains within the composite, leading to better relaxation of residual stresses. They also enhance homogeneity in thermal behavior within the composite, allowing for uniformity in heating and cooling. A trade-off is thus necessary when incorporating plasticizers in the development of bioplastics, as excessive plasticizer use will result in higher organic filler incorporation but lower mechanical strength and thermal instability, leading to warpage.

Figure 4.31 illustrates simulation results of 40 wt. % rHDPE + 30 wt. % RH + 30 wt. % MAPE printed at 210 °C, bed temperature of 60 °C, printing speed of 20 mm/s and layer height of 0.1 mm.

Table 4.18: Residual Stress and Warpage for the 40 wt. % rHDPE + 30 wt. % RH + 30 wt. % MAPE Bioplastic

Test	Extrusion Temperature, °C	Bed temperature, °C	Printing Speed, mm/s	Layer height, mm	Warpage, mm	Residual Stress, MPa
1	210	60	20	0.1	1.426	2.446
2	210	90	30	0.15	1.426	2.446
3	210	120	40	0.2	1.425	2.445
4	220	60	30	0.2	1.522	2.634
5	220	90	40	0.1	1.521	2.634
6	220	120	20	0.15	1.522	2.634
7	230	60	40	0.15	1.630	2.822
8	230	90	20	0.2	1.630	2.822
9	230	120	30	0.1	1.630	2.822

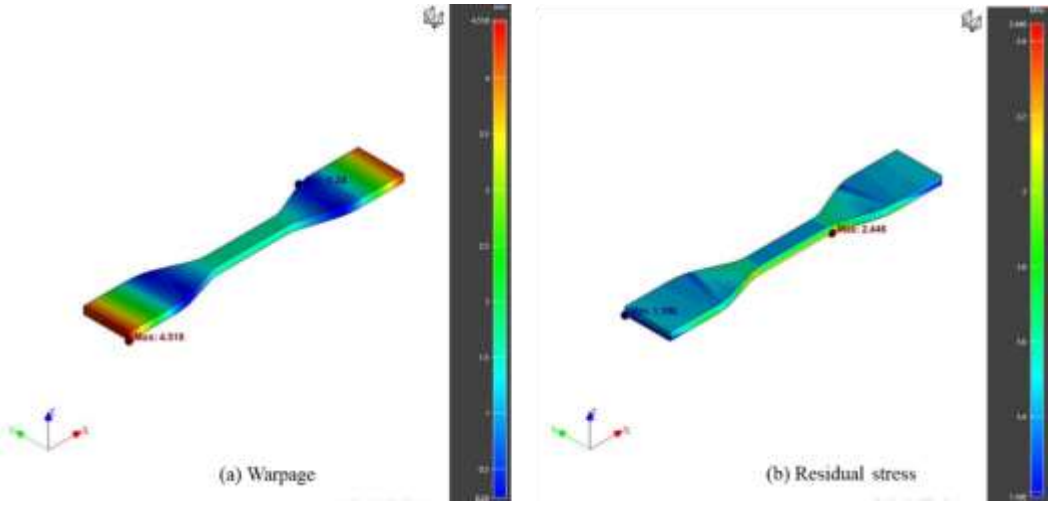

Figure 4.31: Simulation Results of 40 wt. % rHDPE + 30 wt. % RH + 30 wt. % MAPE Bioplastic

a. Warpage of 40 wt. % rHDPE + 30 wt. % RH + 30 wt. % MAPE Bioplastic

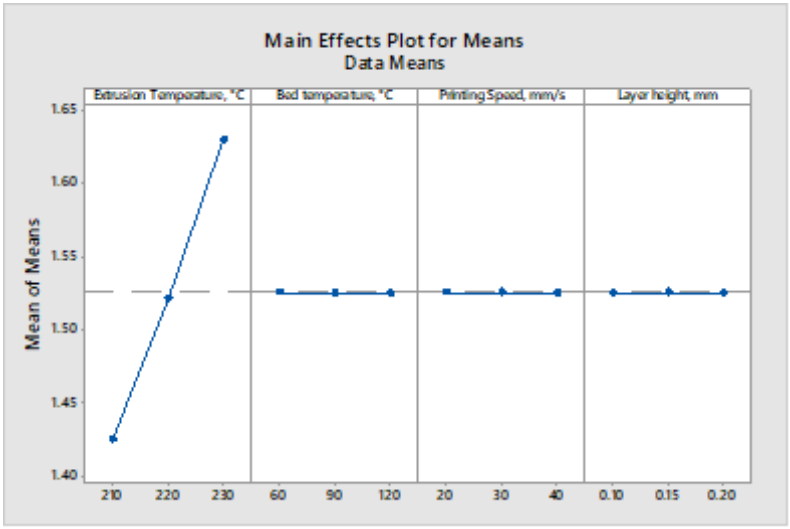

(a)

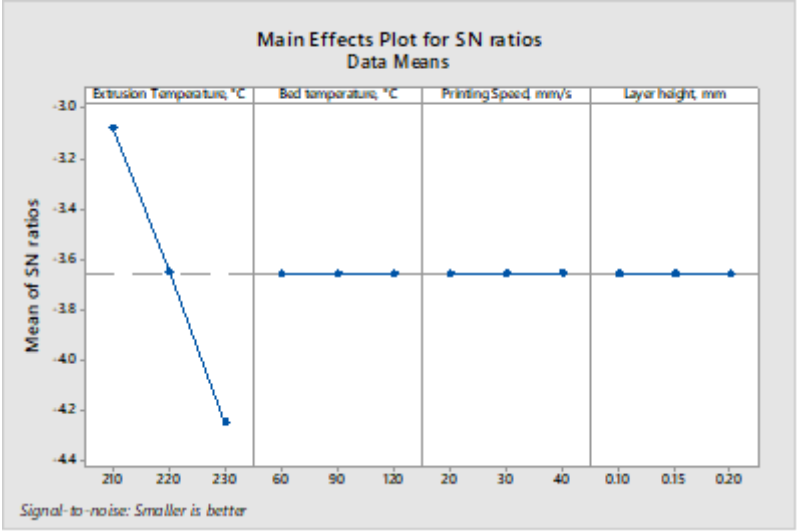

(b)

Figure 4.32: Main Effect Plot for Warpage (a) Means (b) SN Ratio of 40 wt. % rHDPE + 30 wt. % RH + 30 wt. % MAPE Bioplastic

According to Tables 4.19 and 4.20, the extrusion temperature had the most significant impact on warpage, followed by printing speed. The bed temperature and layer height then occupied the third rank equally. The extrusion temperature must be adjusted to accommodate changes in viscosity, ensuring the material flows smoothly from the printing nozzle. Organic fillers increase the viscosity of the melt, causing resistance to material flow, which can lead to nozzle clogging and poor layer adhesion if not well compensated. Printing speed came second in the responses, as it is the parameter that allows the material to be adequately deposited at the reduced flow rate due to the increase in viscosity resulting from the high filler content. From Table 4.20, the best printing parameters for this bioplastic were an extrusion temperature of 210 °C, printing speed of 20 mm/s, bed temperature of 60 °C, and layer height of 0.1 mm.

Table 4.19: Response Table for Average Warpage of the 40 wt. % rHDPE + 30 wt. % RH + 30 wt. % MAPE Bioplastic.

Level	Extrusion Temperature, °C	Bed temperature, °C	Printing Speed, mm/s	Layer height, mm
1	1.426	1.526	1.526	1.526
2	1.522	1.526	1.526	1.526
3	1.630	1.526	1.525	1.526
Delta	0.204	0.000	0.001	0.000
Rank	1	3.5	2	3.5

Table 4.20: Response Table for the Signal-to-Noise Ratio of the 40 wt. % rHDPE + 30 wt. % RH + 30 wt. % MAPE Bioplastic's Warpage

Level	Extrusion Temperature, C	Bed temperature, C	Printing Speed, mm/s	Layer height, mm
1	-3.080	-3.658	-3.654	-3.656
2	-3.646	-3.656	-3.658	-3.658
3	-4.244	-3.656	-3.658	-3.658
Delta	1.163	0.002	0.004	0.002
Rank	1	3.5	2	3.5

b. Residual Stresses of the 40 wt. % rHDPE + 30 wt. % RH + 30 wt. % MAPE Bioplastic

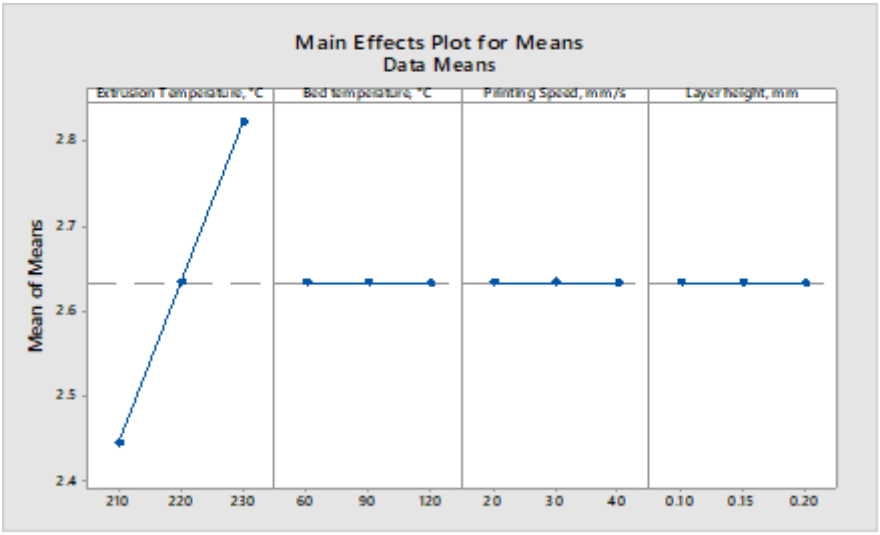

(a)

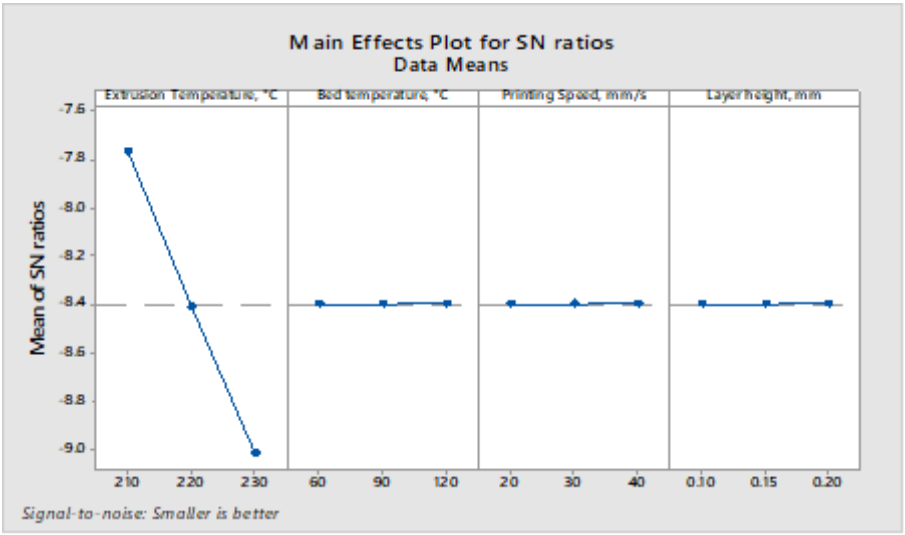

(b)

Figure 4. 2: Main Effect Plot for Residual Stresses (a) Means (b) SN Ratio of 40 wt. % rHDPE + 30 wt. % RH + 30 wt. % MAPE Bioplastic

According to previous responses, the extrusion temperature had the highest influence on residual stress, as shown in Tables 4.21 and 4.22. For residual stress, the other three parameters shared the second rank equally. This situation was in agreement with the 100% rHDPE bioplastic. From Table 4.22, the best extrusion temperature to minimize residual stresses was 210 °C. This analysis, conducted in Minitab 18, reveals that extrusion temperature has the most significant impact on both warpage and residual stresses. To minimize these responses, the temperature had to be at the lower limit of the operating range, as this would reduce the temperature gradient between the printed layers. Since the other three parameters yielded differences in the most favorable selection, a multi-objective optimization technique was necessary to achieve uniformity in the optimal parameters for the three materials.

Table 4.21: Response Table for Average Residual Stresses of the 40 wt. % rHDPE + 30 wt. % RH + 30 wt. % MAPE Bioplastic

Level	Extrusion Temperature, °C	Bed temperature, °C	Printing Speed, mm/s	Layer height, mm
1	2.446	2.634	2.634	2.634
2	2.634	2.634	2.634	2.634
3	2.822	2.634	2.634	2.634
Delta	0.376	0.000	0.000	0.000
Rank	1	3	3	3

Table 4.22: Response Table for Signal-to-Noise Ratios of the 40 wt. % rHDPE + 30 wt. % RH + 30 wt. % MAPE Residual Stresses

Level	Extrusion Temperature, °C	Bed temperature, °C	Printing Speed, mm/s	Layer height, mm
1	-7.768	-8.398	-8.398	-8.398
2	-8.412	-8.398	-8.398	-8.398
3	-9.011	-8.396	-8.396	-8.396
Delta	1.243	0.001	0.001	0.001
Rank	1	3	3	3

4.6 Multi-Objective Optimization using Grey Relational Analysis

As explained in Section 3.3.3, the Grey Relational Analysis (GRA) was employed to optimize process parameters for each material, as it enables multi-response optimization when there are two or more responses to be optimized simultaneously. The goal was to minimize residual stresses and warpage. This was accomplished by combining all of the responses into a single response known as the grey relational grade (GRG), where a higher number denotes better outcomes. Tables 4.23, 4.24, and 4.25 present the grey relational analysis for the three materials.

Table 4.23: Grey Relational Analysis for the 100 wt.% rHDPE

Exp. No	Normalized value		Deviation sequences / DELTA		Grey relational coefficients		GRG
	Warpage	Residual Stress	Warpage	Residual Stress	Warpage	Residual Stress	
1	**1.0000**	**1.0000**	**0.0000**	**0.0000**	**1.0000**	**1.0000**	**1.0000**
2	0.9937	0.9971	0.0063	0.0029	0.9912	0.9878	0.9895
3	1.0000	0.9971	0.0000	0.0029	1.0000	0.9878	0.9939
4	0.4969	0.4985	0.5031	0.5015	0.5842	0.3209	0.4526
5	0.4969	0.5015	0.5031	0.4985	0.5842	0.3222	0.4532
6	0.4969	0.4985	0.5031	0.5015	0.5842	0.3209	0.4526
7	0.0000	0.0000	1.0000	1.0000	0.4142	0.1916	0.3029
8	0.0000	0.0000	1.0000	1.0000	0.4142	0.1916	0.3029
9	0.0000	0.0029	1.0000	0.9971	0.4142	0.1920	0.3031

Table 4.24: Grey Relational Analysis for the 85 wt. % rHDPE + 15 wt.% RH Bioplastic

Exp. No	Normalized value		Deviation sequences / DELTA		Grey relational coefficients		GRG
	Warpage	Residual Stress	Warpage	Residual Stress	Warpage	Residual Stress	
1	**1.0000**	**1.0000**	**0.0000**	**0.0000**	**1.0000**	**1.0000**	**1.0000**
2	0.9977	1.0000	0.0023	0.0000	1.0000	1.0000	0.9984
3	0.9955	1.0000	0.0045	0.0000	1.0000	1.0000	0.9968
4	0.5113	0.4895	0.4887	0.5105	0.5911	0.3170	0.4541
5	0.5656	0.5021	0.4344	0.4979	0.6255	0.3225	0.4740
6	0.5136	0.4937	0.4864	0.5063	0.5911	0.3188	0.4550
7	0.0000	0.0000	1.0000	1.0000	0.4142	0.1916	0.3029
8	0.0566	0.0169	0.9434	0.9831	0.4308	0.1942	0.3125
9	0.0588	0.0169	0.9412	0.9831	0.4288	0.1942	0.3115

Table 4.25: Grey Relational Analysis for the 40 wt. % rHDPE + 30 wt. % RH + 30 wt. % MAPE Bioplastic

Exp. No	Normalized value		Deviation sequences / DELTA		Grey relational coefficients		GRG
	Warpage	Residual Stress	Warpage	Residual Stress	Warpage	Residual Stress	
1	0.9951	0.9973	0.0049	0.0027	0.9931	0.9889	0.9910
2	0.9951	0.9973	0.0049	0.0027	0.9931	0.9889	0.9910
3	**1.0000**	**1.0000**	**0.0000**	**0.0000**	**1.0000**	**1.0000**	**1.0000**
4	0.5268	0.4987	0.4732	0.5013	0.5991	0.3210	0.4600
5	0.5317	0.4987	0.4683	0.5013	0.6016	0.3210	0.4613
6	0.5268	0.4987	0.4732	0.5013	0.5991	0.3210	0.4600
7	0.0000	0.0000	1.0000	1.0000	0.4142	0.1916	0.3029
8	0.0000	0.0000	1.0000	1.0000	0.4142	0.1916	0.3029
9	0.0000	0.0000	1.0000	1.0000	0.4142	0.1916	0.3029

The optimal parameter levels were those that had the highest grey relational grade value. From Table 4.23, the optimum parameter levels for the multiple response of the 100 wt.% bioplastic was an extrusion temperature of 210 °C, a bed temperature of 60 °C, a printing speed of 20 mm/s and a layer height of 0.1 mm. From Table 4.24, the optimum parameter for the 85 wt.% rHDPE + 15 wt.% bioplastic was the same as that of the 100 wt.% bioplastic, i.e., extrusion temperature of 210 °C, a bed temperature of 60 °C, a

printing speed of 20 mm/s and a layer height of 0.1 mm. Table 4.25 presents the optimum parameters for the 40 wt. % rHDPE + 30 wt. % RH + 30 wt. % MAPE where the extrusion temperature was 210 °C, a bed temperature of 120 °C, a printing speed of 40 mm/s and a layer height of 0.2 mm. It can be observed that there was consistency in the extrusion temperature, confirming that this was the optimal extrusion temperature for the developed bioplastics. It also confirms that higher temperatures result in higher residual stresses and warpage. To minimize residual stresses and warpage, it is crucial to reduce the extrusion temperature without compromising the extrusion process and flow rate. Very high amounts of the organic filler will necessitate an increase in bed temperature to improve adhesion to the print bed, due to increased adhesive forces. A higher layer height will improve the temperature gradient since fewer layers will be required to print the complete part.

4.7 Structural Analysis – Coupled Simulation

During the structural analysis, the printing process data was transferred to the structural mesh. This included residual stresses, tool path, printing direction, microstructure, and porosity. Figure 4.34 shows the orientation of the RH fibers, which indicate that at the center of the part, the fiber orientation was in the x-direction, with an orientation tensor of 1, since this was a short-fiber reinforcement.

Figure 4.34: Orientation Tensor after Mapping (Toolpath to the FEA Model)

At the edges, the fibers were oriented in the y-direction due to the tool path. This resulted in differences in stresses within the regions of the printed part due to differences in material behavior caused by differences in the orientation tensor of the fiber-reinforced polymer. The equivalent accumulated plastic strain and failure indicator can now be observed in Ansys.

4.7.1 Structural Results: Total Strain

Figure 4.35 shows the total strain of the 85 wt.% rHDPE +15 wt.% RH bioplastic where the strain ranged from 0.0125 to 0.0382. The maximum strain was experienced at the center of the sample (gauge length) due to the sample's geometry, where the gauge length had a narrower cross-section compared to the other lengths. This reduction in cross-section led to high stress concentrations at the gauge length during the application of axial loading. The rest of the sample length had a wider cross-section, which could resist deformation more effectively. Moreover, at the gauge length, the region was free from constraints; therefore, the load application was symmetrical, resulting in a uniform stress distribution.

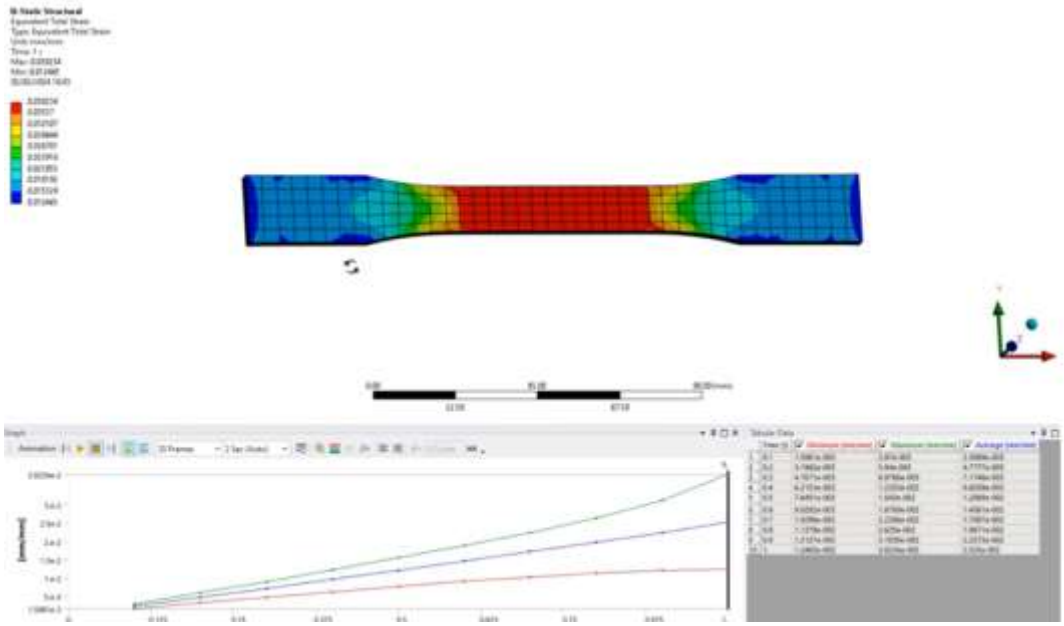

Figure 4.35: Total Strain of the 85 wt.% rHDPE+15wt.% RH Bioplastic

The total strain near the ends of the sample was lower than at the center, as the clamping of the sample was done at the ends, introducing constraints that deterred the deformation of the material. The maximum total strain for 100 wt. % rHDPE was 0.0971, which was higher than that of the fiber-reinforced rHDPE. As for the 40 wt.% rHDPE + 30 wt.% + 30 wt.% MAPE bioplastic, the maximum total strain was 0.0581. The effect of the RH fibers was a reduction in the total strain of the bioplastic, as the fibers constrained polymer chain mobility. The weak interfacial bonding between the RH fiber and the rHDPE matrix led to debonding, which caused early failure. The MAPE improved the interfacial adhesion of the bioplastic; however, the strain of this bioplastic could not match that of the 100 wt.% rHDPE. Even with improved adhesion introduced by the MAPE, the overall deformation was limited by the strain compatibility between the matrix and the fibers.

4.7.2 Structural Results: Failure Indicator

Figure 4.36 displays the failure indicator simulation results for the bioplastic, which consists of 85 wt.% rHDPE and 15 wt.% RH.

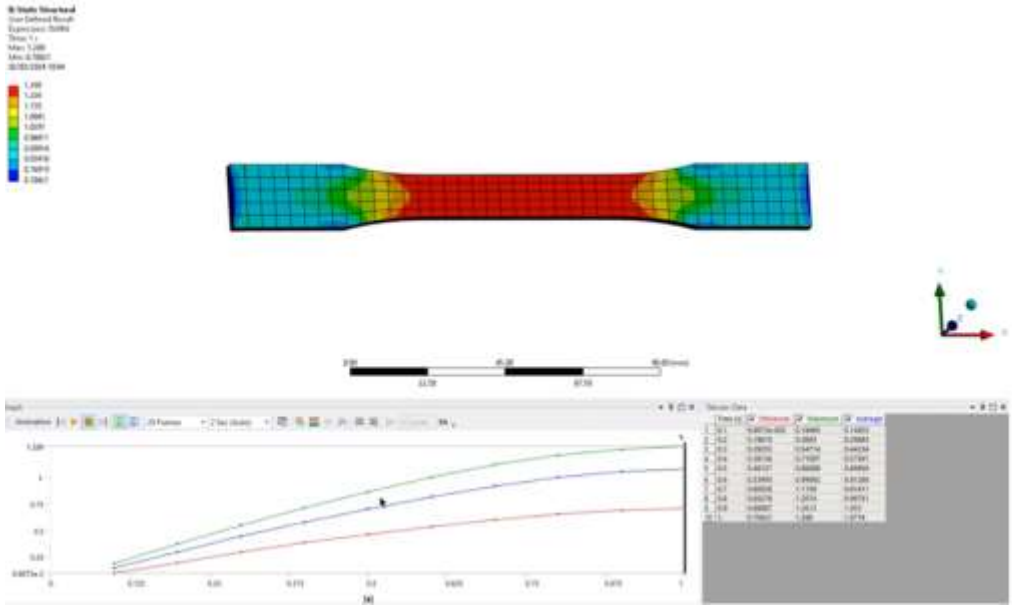

Figure 4.36: Failure Indicator of the 85 wt.% rHDPE+15wt.% RH Bioplastic

In the structural analysis, the hybrid solution was selected because it enables strong coupling for both linear and nonlinear materials, such as bioplastics. The Ansys solver runs with Digimat, where Digimat precomputes the macroscopic material properties and communicates with the structural code at each iteration of the computation. The failure indicator given in Ansys is a measurable structural sign that shows the beginning of material failure under stress. They help to identify when the material has reached or is approaching its service limits.

The failure indicators for the bioplastics were slightly higher than those for the unfilled rHDPE. The unfilled rHDPE ranged from 0.8609 to 0.4616, while the fiber-reinforced bioplastics had a failure indicator ranging from 1.289 to 0.70421. The higher failure indicator in the fiber-reinforced polymer is due to microvoid formation caused by the incorporation of RH fibers. Additionally, aging from recycling reduced material elongation, leading to failure. Stiffness gradually decreased to reflect material damage as element failure occurred in the FE analysis. Stiffness reduction begins once each integration point fails and stops when damage reaches its maximum variable.

4.8 Validation of the Printing Simulation Using Experimental Results

Experimental validation was conducted to assess the warpage and residual stresses of the simulated parts at optimal parameter settings. This section presents and compares the simulated and experimental results.

4.8.1 Warpage Measurement of the Part Printed

From the optimal values identified using the grey relational analysis method, samples were printed, and warpage was measured. From each sample, longitudinal and lateral measurements were taken at three points, i.e., top, center, and bottom points, as shown in Figure 4.37. The 3D image of the warped part, as analyzed by the laser confocal microscope, is shown in Figure 4.38.

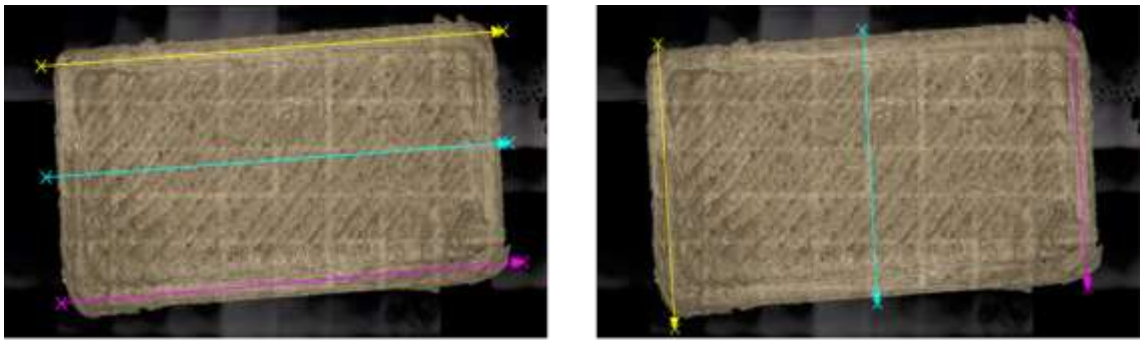

(a) (b)

Figure 4.37: Points for Warpage Measurement: (a) Longitudinal Measurement, (b) Lateral Measurements

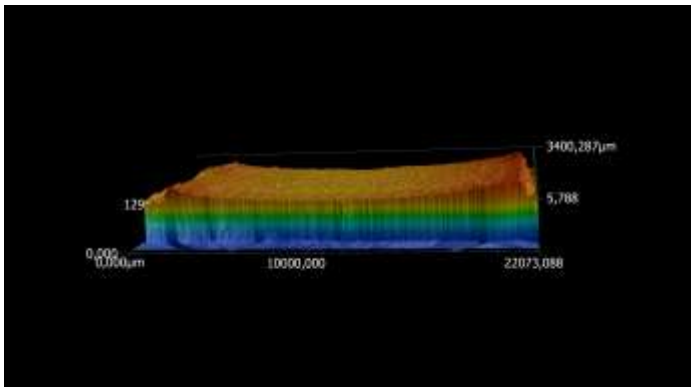

Figure 4.38: 3D Image of Warped Part

In this study, the maximum height of the profile, Rz, was used as the profile parameter for warpage, as illustrated in Figure 4.39. Table 4.26 compares the average measured warpage with the simulated warpage. Lateral measurements are included in Table B1 in the appendix section.

Table 4.26: Comparison of Measured and Simulated Average Values of Longitudinal Warpage

Bioplastic composition	**Measured warpage (mm)**	**Simulated warpage (mm)**	**Deviation (%)**
100 wt. % rHDPE	1.447 ± 0.084	1.368 ± 0.069	5.46
85 wt.% rHDPE + 15 wt.% RH	1.243 ± 0.214	1.160 ± 0.057	6.68
40 wt. % rHDPE + 30 wt. % RH + 30 wt. % MAPE	1.540 ± 0.147	1.426 ± 0.089	7.40

From the table, the error margins for the warpage were 5.46%, 6.68%, and 7.40%, indicating a good agreement between the experimental and simulated values. These error margins present an improvement in validation compared to the work done by (Zhou et al., 2017).The acceptable error margins indicate accuracy in material modelling done in Digimat for process and structural simulation. The confidence level can be further improved by enhancing accuracy in material modelling.

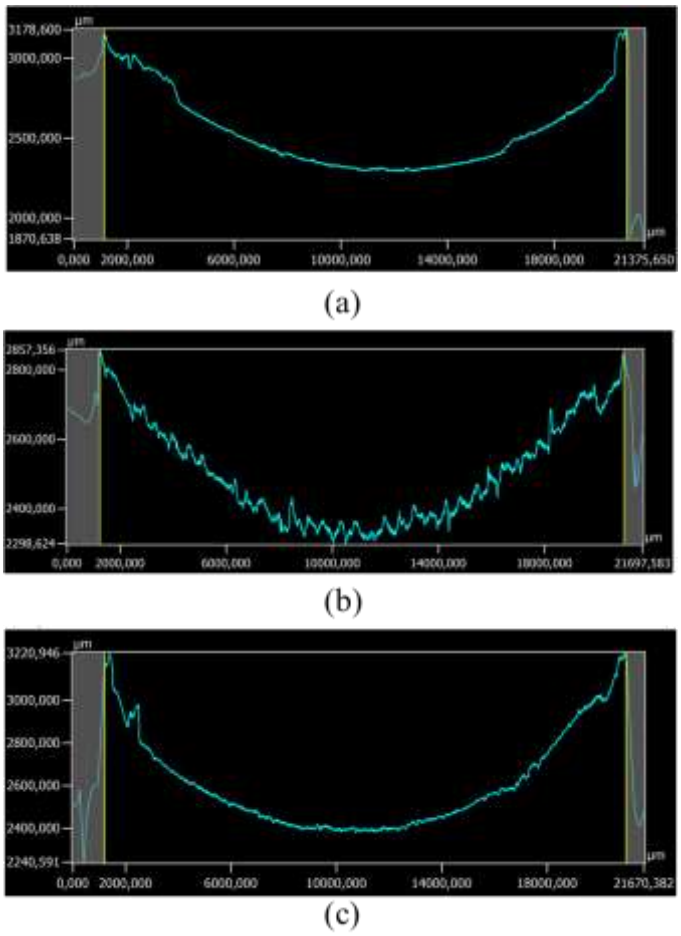

Figure 4.39: Total Profile of Warped Printed Part. (a) Center Profile, (b) Top Profile, (c) Bottom Profile

4.8.2 Residual Stress Analysis of Printed Samples from the Bioplastic

The determination of residual stress using an X-ray diffractometer is based on the diffraction peak positions and how they shift with the tilt angle of the sample. Figures 4.40 and 4.41 show the XRD spectra of the bioplastics with the highest peak at a diffraction angle of 20°. There were no sharp peaks after 60° 2θ, hence the computation for interplanar spacing was done for diffraction angles less than 60°. At the peak shifts, the lattice spacing, that is, the *d*-spacing, was determined for the samples. The changes

in the *d*-spacing were used to determine the strain in the samples, which were then used to determine residual stress from the plot of strain ε_{ψ} vs $sin^2\psi$.

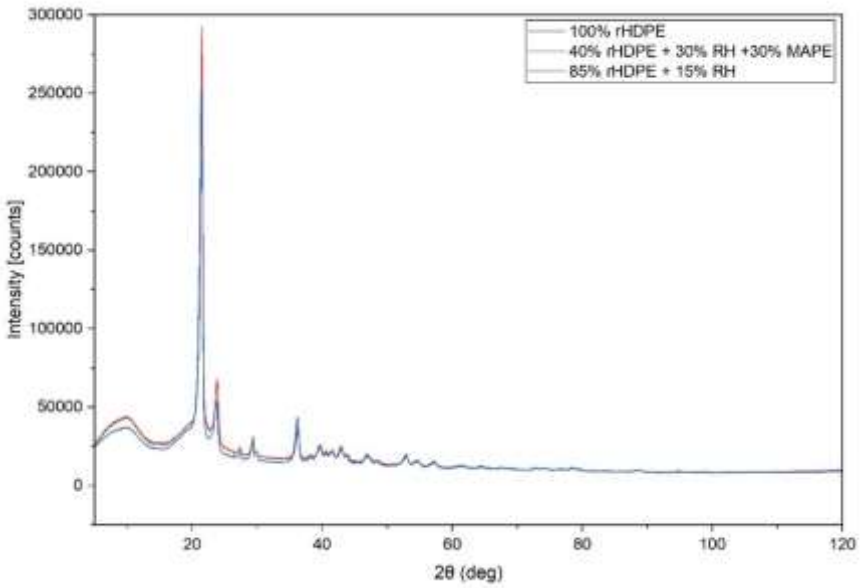

Figure 4.40: Combined XRD Spectra of the Bioplastic Samples

The high intensity was experienced at 20° for all the bioplastics, an indication of material orientation during the analysis. Higher residual stresses were experienced from the unfilled polymer than the organic-filled polymer due to a lowering of the coefficient of thermal expansion introduced by the organic fillers. By lowering the CTE of the biocomposite, the development of residual stresses was introduced.

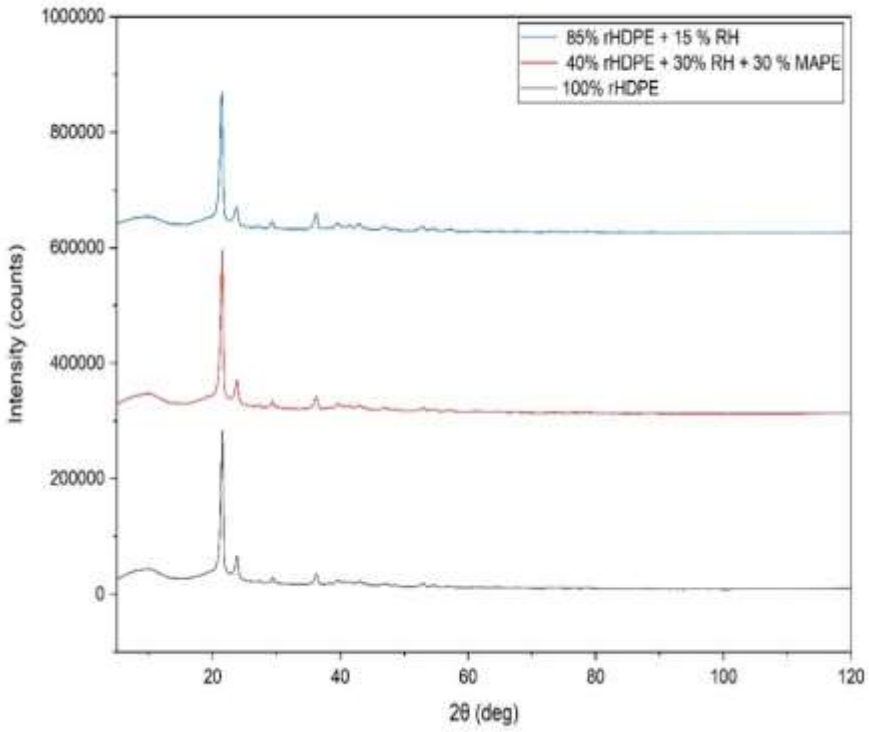

Figure 4.41: XRD Spectra of the Bioplastics Illustrating the Different Profiles at the Y-Offset

Figures 4.42, 4.43, and 4.44 show the plots of the bioplastic with the gradient giving the residual stresses. The values are summarized in Table 4.27. From the Table, the error margins were 4.29%, 1.49%, and 5.56%, showing a good agreement between the measured values and the simulated values. These lower error margins can be attributed to the use of the X-ray diffractometer that employs non-destructive testing with high accuracy and precision.

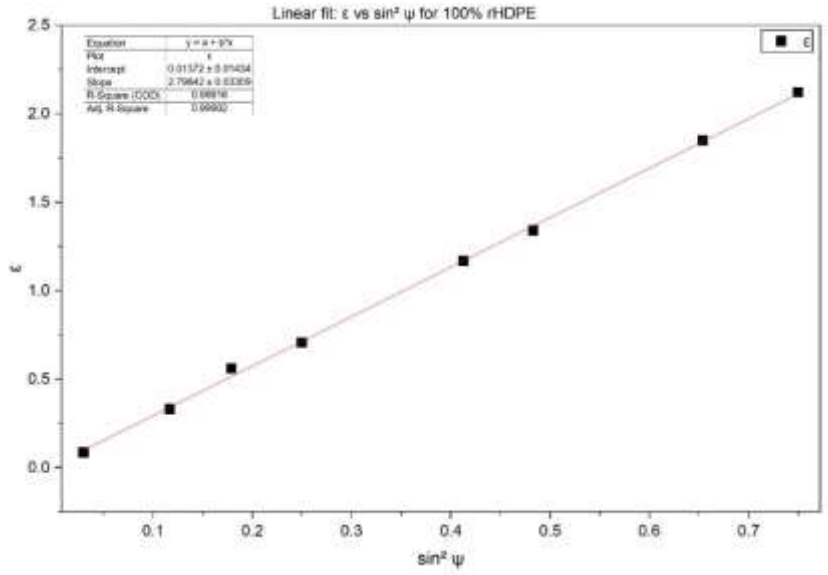

Figure 4.42: A Plot of Strain ε vs sin² ψ for the 100% rHDPE

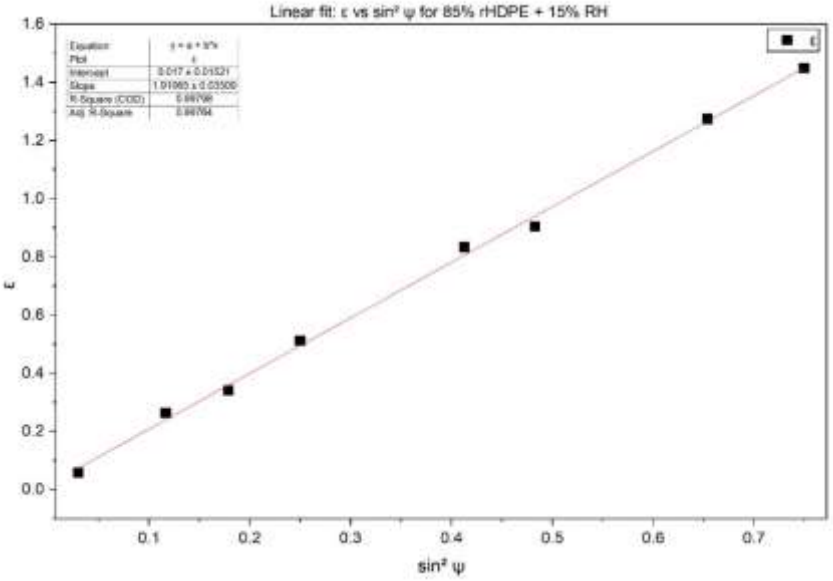

Figure 4.43: A Plot of Strain ε vs sin² ψ for the 85% rHDPE + 15% Bioplastic

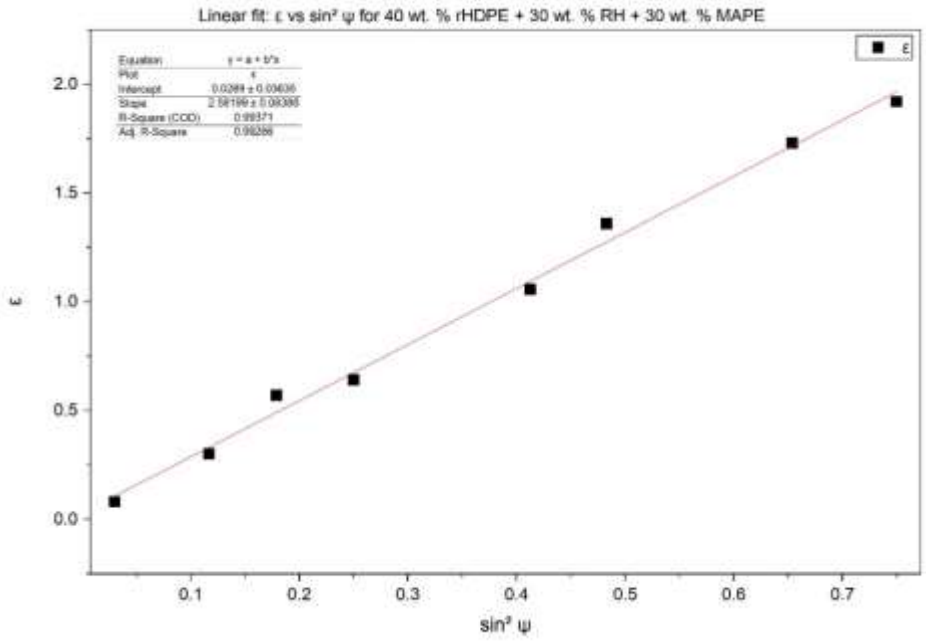

Figure 4.44: A Plot of Strain ε vs sin² ψ for the 40% rHDPE + 30% RH + 30% MAPE Bioplastic

Table 4.27: Comparison of Measured and Simulated Average Values of Residual Stresses

Bioplastic composition	**Measured Residual Stress (MPa)**	**Simulated Residual Stress (MPa)**	**Deviation (%)**
100 wt. % rHDPE	2.798 ± 0.033	2.683 ± 0.074	4.29
85 wt.% rHDPE + 15 wt.% RH	1.911 ± 0.035	1.883 ± 0.062	1.49
40 wt. % rHDPE + 30 wt. % RH + 30 wt. % MAPE	2.582 ± 0.084	2.446 ± 0.095	5.56

4.8.3 Biosensor Fabrication from the Bioplastic

With the developed bioplastic, microfluidic chips have been successfully printed and tested. Figure 4.45 illustrates the printed biomedical devices used in microfluidics. The bioplastic material demonstrated the potential for developing biomedical devices, including microfluidic chips with internal channels, which can be utilized in biological processes such as point-of-care applications and the measurement of pathogens, using cost-efficient materials.

Figure 4.45: Printed Biomedical Devices from the Bioplastic (a) Microfluidic Substrate (b) Microfluidic Chip

CHAPTER FIVE

CONCLUSIONS AND RECOMMENDATIONS

5.1 Conclusions

This work described the development of bioplastics from recycled HDPE and rice husk fillers in various percentages. The plasticizer MAPE was used to enhance the flowability and coupling between the organic rice husks and the inorganic polymer. The characterization of the developed bioplastics was conducted to determine their mechanical, thermal, physical, and morphological properties. Fused filament fabrication was used to test the printability of the developed biofilaments and determine the maximum percentage of biofilament that could be printed. The L9 Taguchi DoE was conducted to investigate the impact of printing parameters on residual stresses and warpage. The extrusion temperature was identified as the most crucial parameter in printing with fiber-reinforced polymers. The developed bioplastics were modeled for simulation to optimize printing parameters and determine the performance of printed parts. Experimental validation was conducted to validate the material model and the optimal parameters.

From this study, the key findings are summarized below:

i. The development of biofilaments using an extrusion system by melt-mixing recycled high-density polyethylene with rice husk filler was successful with up to 35 wt.% of rice husk filler as a fiber reinforcement. The printability of the biofilament was achievable up to 30 wt.% of rice husk filler. This high percentage was enabled by adding a compatibilizer, maleic anhydride-functionalized polyethylene (MAPE).
ii. Although there was a slight decrease in maximum tensile strength with the addition of RH fillers into the rHDPE matrix, the fabricated biofilaments demonstrated good mechanical properties, with the 30 wt.% RH biofilament

showing a maximum tensile strength of 8.53 MPa, an elongation of 6.6%, and a tensile modulus of 129 MPa. These characteristics are suitable for producing non-load-bearing parts, such as housings for electrical and electronic devices, food packaging, and biomedical equipment.

iii. Incorporating rice husk filler decreased the crystallinity from 54.91% to 43.45%, which limited the mobility of the polymer chains. This resulted in better thermal shrinkage controls, leading to less warping of printed objects and showing improved thermal stability.

iv. The biodegradability of the material increased to 10.54% over 24 weeks with the addition of rice husk filler into the rHDPE matrix. Additionally, the rice husk fillers improved the biofilaments' water absorption capability, thereby speeding up biodegradation.

v. Extrusion temperature had the most significant influence on both the residual stresses and warpage. Higher extrusion temperatures resulted in more residual stress and subsequently warpage because they cause reheating to occur more extensively on the previously deposited layer, leading to higher temperature gradients within the material.

vi. New material files from rHDPE and RH were created for FFF process simulation. The materials could be tuned for customized applications. Optimized process parameters for printing the biofilaments were established. Non-load-bearing applications in biomedical fields, such as casings and microfluidic substrates, were demonstrated.

vii. The failure indicators for the bioplastics were slightly higher than those for the unfilled rHDPE. This was due to the formation of microvoids caused by the incorporation of RH fibers. Additionally, recycling introduced material aging, which resulted in a reduction in material elongation, ultimately leading to failure.

viii. Experimental validation achieved maximum error margins of less than 8% indicating a high level of accuracy in the material modelling.

5.2 Recommendations

From this study, the following recommendations are presented for future considerations:

i. To further improve the interfacial bonding between polymer and organic filler, surface modification techniques, e.g., plasma treatment, UV treatment, coatings, and laser texturing, should be considered.
ii. Advanced optimization techniques for non-linear data can be considered for the process optimization, e.g., ANN, GA. These advanced techniques could help reduce the error margin.
iii. Further studies should explore the effect of other printing parameters, such as different print orientations, infill percentages, and extrusion percentages, on the residual stresses and warpage.
iv. Porosity measurement should be performed during printing simulation and structural analysis. The impact of different fiber percentages on part porosity should be examined.
v. The homogeneity and flowability of the mixture could be analyzed through the determination of the melt flow to check if the dispersion of the filler is uniform within the filler matrix.

REFERENCES

Ahmad, H., Chhipi-Shrestha, G., Hewage, K., & Sadiq, R. (2022). A Comprehensive Review on Construction Applications and Life Cycle Sustainability of Natural Fiber Biocomposites. In *Sustainability (Switzerland) 14*(23). MDPI. https://doi.org/10.3390/su142315905

Akampumuza, O., Wambua, P. M., Ahmed, A., Li, W., & Qin, X. H. (2017). Review of the applications of biocomposites in the automotive industry. In *Polymer Composites*, *38*(11), 2553–2569. https://doi.org/10.1002/pc.23847

Al Mahmud, Md. Z. (2023). Exploring the versatile applications of biocomposites in the medical field. *Bioprinting*, *36*, e00319. https://doi.org/https://doi.org/10.1016/j.bprint.2023.e00319

Alam, N., Alam, M., & Ahmad, S. (2021). Optimization of Fused Deposition Modelling process parameters using Teaching Learning Based Optimization (TLBO) algorithm. *IOP Conference Series: Materials Science and Engineering*, *1149*(1), 012014. https://doi.org/10.1088/1757-899x/1149/1/012014

Al-Oqla, F. M., & Omari, M. A. (2017). Sustainable biocomposites: Challenges, potential and barriers for development. *Green Energy and Technology*, 13–29. https://doi.org/10.1007/978-3-319-46610-1_2

Andanje, M. N., Mwangi, J. W., Mose, B. R., & Carrara, S. (2023). Biocompatible and biodegradable 3D printing from bioplastics: a review. *Polymers 2023 15*, 2355.

ASTM International [ASTM]. (2013). *ASTM F2792-12a Standard Terminology for Additive Manufacturing Technologies*. *Procedia Eng*, *63*, 4-11.

Avient Corporation. (2024, October 21). *Long vs Short Fiber*. Avient Corporation.

Azam, F. A. A., Royan, N. R. R., Yuhana, N. Y., Radzuan, N. A. M., Ahmad, S., & Sulong, A. B. (2020). Fabrication of porous recycled HDPE biocomposites foam: Effect of rice husk filler contents and surface treatments on the mechanical properties. *Polymers*, *12*(2). https://doi.org/10.3390/polym12020475

Azizi Machekposhti, S., Mohaved, S., & Narayan, R. J. (2019). Inkjet dispensing technologies: recent advances for novel drug discovery. In *Expert Opinion on Drug Discovery 14*(2), 101–113.. https://doi.org/10.1080/17460441.2019.1567489

Balla, V. K., Kate, K. H., Satyavolu, J., Singh, P., & Tadimeti, J. G. D. (2019). Additive manufacturing of natural fiber reinforced polymer composites: Processing and prospects. In *Composites Part B: Engineering* (Vol. 174). New York: Elsevier Ltd. https://doi.org/10.1016/j.compositesb.2019.106956

Bhagia, S., Bornani, K., Agarwal, R., Satlewal, A., Ďurkovič, J., Lagaňa, R., Bhagia, M., … & Ragauskas, A. J. (2021). Critical review of FDM 3D printing of PLA biocomposites filled with biomass resources, characterization, biodegradability, upcycling and opportunities for biorefineries. *Applied materials today*, *24*, 101078.

Bi, H., Xu, M., Ye, G., Guo, R., Cai, L., & Ren, Z. (2018). Mechanical, thermal, and shape memory properties of three-dimensional printing biomass composites. *Polymers*, *10*(11). https://doi.org/10.3390/polym10111234

Bisht, N. G. P. C. & Nisha, R. (2020). Rice husk as a fibre in composites. *Journal of the Mechanical Behavior of Materials*, *29*(1), 147–162.

Boyron, O., Marre, T., Delauzun, A., Cozic, R., & Boisson, C. (2019). An advanced technique for linear low-density polyethylene composition determination: TGA–IST16–GC–MS coupling. *Macromolecular Chemistry and Physics*, *220*(17), 1900162.

Calignano, F., Manfredi, D., Ambrosio, E. P., Biamino, S., Lombardi, M., Atzeni, E., Salmi, A., Minetola, P., Iuliano, L., & Fino, P. (2017). Overview on additive manufacturing technologies. *Proceedings of the IEEE*, *105*(4), 593–612. https://doi.org/10.1109/JPROC.2016.2625098

Carrara, S. (2025). More Sustainable Bio/CMOS Interfaces for Remote Monitoring of Human Health [Feature]. *IEEE Circuits and Systems Magazine*, *25*(2), 42–56. https://doi.org/10.1109/MCAS.2025.3544986

Carruthers, J. (2012). Technology Overview Biocomposites. *Technology Strategy Board*, 1–40.

Cestari, S. P., Mendes, L. C., Da Silva, D. F., Chimanowsky, J. P., Altstädt, V., Demchuk, V., Lang, A., Leonhardt, R. G., & Keller, J. H. (2013). Properties of recycled high density polyethylene and coffee dregs composites. *Polimeros*, *23*(6), 733–737. https://doi.org/10.4322/polimeros. 2014.011

Chen, R. S., Ab Ghani, M. H., Ahmad, S., Salleh, M. N., & Tarawneh, M. A. (2015). Rice husk flour biocomposites based on recycled high-density polyethylene/polyethylene terephthalate blend: Effect of high filler loading on physical, mechanical and thermal properties. *Journal of Composite Materials*, *49*(10), 1241–1253. https://doi.org/10.1177/0021998314533361

Chohan, J. S., Mittal, N., & Kumar, R. (2020). Parametric optimization of fused deposition modeling using learning enthusiasm enabled teaching

learning based algorithm. *SN Applied Sciences*, *2*(12). https://doi.org/10.1007/s42452-020-03818-4

Dey, A., Rahman, M. M., Yodo, N., & Grewell, D. (2023). Development of biocomposite filament for fused filament fabrication from soy hulls and soy protein isolate. *Materials Today Communications*, *34*, 105316. https://doi.org/https://doi.org/10.1016/j.mtcomm.2023.105316

Dey, A., & Yodo, N. (2019). A systematic survey of FDM process parameter optimization and their influence on part characteristics. *Journal of Manufacturing and Materials Processing*, *3*(3), 64.

Donelli, I., Freddi, G., Nierstrasz, V. A., & Taddei, P. (2010). Surface structure and properties of poly-(ethylene terephthalate) hydrolyzed by alkali and cutinase. *Polymer Degradation and Stability*, *95*(9), 1542–1550. https://doi.org/https://doi.org/10.1016/j.polymdegradstab.2010.06.011

El-Hadi, A. M. (2014). The effect of additives interaction on the miscibility and crystal structure of two immiscible biodegradable polymers. *Polimeros*, *24*(1), 9–16. https://doi.org/10.4322/polimeros.2014.039

Fadillah, F., Suryanto, H., & Suprayitno, S. (2023). Study on Effect of 3D Printing Parameters on Surface Roughness and Tensile Strength Using Analysis of Variance. *Journal of Mechanical Engineering Science and Technology (JMEST)*, *7*(2), 96. https://doi.org/10.17977/um016v7i22023p096

Faruk, O., Bledzki, A. K., Fink, H. P., & Sain, M. (2012). Biocomposites reinforced with natural fibers: 2000-2010. In *Progress in Polymer Science* 37(11), 1552–1596. https://doi.org/10.1016/j.progpolymsci.2012.04.003

Feng, X.; Yang, Z.; Chmely, S.; Wang, Q.; Wang, S. & Xie, Y. (2017). Lignin-coated cellulose nanocrystal filled methacrylate composites prepared via 3D stereolithography printing: Mechanical reinforcement and thermal stabilization. *Carbohydrate Polymers, 169,* 272–281. https://doi.org/10.1016/j.carbpol.2017.04.001

Ferreira, R. T. L., Amatte, I. C., Dutra, T. A., & Bürger, D. (2017). Experimental characterization and micrography of 3D printed PLA and PLA reinforced with short carbon fibers. *Composites Part B: Engineering, 124,* 88–100. https://doi.org/10.1016/j.compositesb.2017.05.013

Fredi, G., & Dorigato, A. (2024). Compatibilization of biopolymer blends: A review. *Advanced Industrial and Engineering Polymer Research, 7*(4), 373-404.

Gad, A. G. (2022). Particle Swarm Optimization Algorithm and Its Applications: A Systematic Review. *Archives of Computational Methods in Engineering*, *29*(5), 2531–2561. https://doi.org/10.1007/s11831-021-09694-4

Gardan, J. (2016). Additive manufacturing technologies: State of the art and trends. *International Journal of Production Research*, *54*(10), 3118–3132. https://doi.org/10.1080/00207543.2015.1115909

Ghosh, N., Pal, P. K., & Nandi, G. (2017). GMAW dissimilar welding of AISI 409 ferritic stainless steel to AISI 316L austenitic stainless steel by using AISI 308 filler wire. *Engineering Science and Technology, an International Journal*, *20*(4), 1334–1341. https://doi.org/https://doi.org/10.1016/j.jestch. 2017.08.002

Goldberg, D. E. (1989). *Genetic Algorithms in Search, Optimization and Machine Learning* (Vol. 1). Boston: Addison-Wesley Publishing Company.

Gorrepotu, S. R., Debnath, K., & Mahapatra, R. (2021). *Development and Characterization of PLA-Based Green Composites: Experimental and Simulation Studies* (pp. 209–223). Singapore: Springer Singapore.

Haibo Long, Zhiqiang Wu, Qianqian Dong, Yuting Shen, Wuyi Zhou, Ying Luo, Chaoqun Zhang, X. D. (2019). Mechanical and thermal properties of bamboo fiber reinforced polypropylene/polylactic acid composites for 3D printing. *Polymer Engineering and Science*, *59*(s2), E247–E260. https://doi.org/10.1002/pen.25043

Han, N., Zhao, X., & Thakur, V. K. (2023). Adjusting the interfacial adhesion via surface modification to prepare high-performance fibers. *Nano Materials Science*, *5*(1), 1–14. https://doi.org/https://doi.org/10.1016/j.nanoms.2021.11.004

Harper, D., & Wolcott, M. (2004). Interaction between coupling agent and lubricants in wood–polypropylene composites. *Composites Part A: Applied Science and Manufacturing*, *35*(3), 385–394. https://doi.org/https://doi.org/10.1016/j.compositesa.2003.09.018

Hasanzadeh, R., Mihankhah, P., Azdast, T., Aghaiee, S., & Park, C. B. (2023). Optimization of Process Parameters of Fused Filament Fabrication of Polylactic Acid Composites Reinforced by Aluminum Using Taguchi Approach. *Metals*, *13*(6). https://doi.org/10.3390/met13061013

He, Y., Zhang, F., Saleh, E., Vaithilingam, J., Aboulkhair, N., Begines, B., Tuck, C. J., Hague, R. J. M., Ashcroft, I. A., & Wildman, R. D. (2017). A Tripropylene Glycol Diacrylate-based Polymeric Support Ink for Material Jetting. *Additive Manufacturing*, *16*, 153–161. https://doi.org/10.1016/j. addma. 2017.06.001

Hertzberg, Richard, W. Vinci, Richard, P & Hertzberg, J. L. (2020). *Deformation and fracture mechanics of engineering materials* (Sixth). New York: John Wiley & Sons.

Heylin, M. (2019). European Bioplastics: Facts and figures. *13th European Bioplastics Conference*, *13*(13), 1–16. https://doi.org/10.1021/cen-v050n023.p003

Hidayat, Rahmat, A., Nissa, R. C., Sukamto, Nuraini, L., Nurtanto, M., & Ramadhani, W. S. (2023). Analysis of rice husk biochar characteristics under different pyrolysis temperature. *IOP Conference Series: Earth and Environmental Science*, *1201*(1). https://doi.org/10.1088/1755-1315/1201/1/012095

Huang, S. H., Liu, P., Mokasdar, A., & Hou, L. (2013). Additive manufacturing and its societal impact: A literature review. In *International Journal of Advanced Manufacturing Technology, 67*(5–8), 1191–1203). https://doi.org/10.1007/ s00170-012-4558-5

Imre, B., García, L., Puglia, D., & Vilaplana, F. (2019). Reactive compatibilization of plant polysaccharides and biobased polymers: Review on current strategies, expectations and reality. In *Carbohydrate Polymers*, *209*, 20–37). https://doi.org/10.1016/j.carbpol.2018.12.082

International, A. (n.d.). *ASTM International - ASTM E473-18 : Standard Terminology Relating to Thermal Analysis and Rheology*.

Jin, Z., Zhang, Z., Demir, K., & Gu, G. X. (2020). Machine Learning for Advanced Additive Manufacturing. *Matter*, *3*(5), 1541–1556. https://doi.org/https://doi.org/ 10.1016/j.matt.2020.08.023

Kanchana, J., Prasath, V., Krishnaraj, V., & Geetha Priyadharshini, B. (2019). Multi response optimization of process parameters using grey relational analysis for milling of hardened Custom 465 steel. *Procedia*

Manufacturing, *30*, 451–458. https://doi.org/10.1016/j.promfg.2019.02.064

Kariz, M., Sernek, M., Obućina, M., & Kuzman, M. K. (2018). Effect of wood content in FDM filament on properties of 3D printed parts. *Materials Today Communications*, *14*, 135–140. https://doi.org/10.1016/j.mtcomm.2017.12.016

Keiluweit, M., Nico, P. S., Johnson, M. G., & Kleber, M. (n.d.). *Dynamic Molecular Structure of Plant Biomass-derived Black Carbon (Biochar) 2-Supporting Information-3*.

Kenny, J. M., & Nicolais, L. (1989). Science and Technology of Polymer Composites. In G. Allen & J. C. Bevington (Eds.), *Comprehensive Polymer Science and Supplements* (pp. 471–525). New Jersey: Pergamon. https://doi.org/https://doi.org/10.1016/B978-0-08-096701-1.00236-6

Koffi, A., Toubal, L., Jin, M., Koffi, D., Döpper, F., Schmidt, H. W., & Neuber, C. (2022). Extrusion-based 3D printing with high-density polyethylene Birch-fiber composites. *Journal of Applied Polymer Science*, *139*(15). https://doi.org/10.1002/app.51937

Kumar, N., & Das, D. (2017). Fibrous biocomposites from nettle (Girardinia diversifolia) and poly(lactic acid) fibers for automotive dashboard panel application. *Composites Part B: Engineering*, *130*, 54–63. https://doi.org/10.1016/j.compositesb.2017.07.059

Lamm, M. E., Wang, L., Kishore, V., Tekinalp, H., Kunc, V., Wang, J., ... & Ozcan, S. (2020). Material extrusion additive manufacturing of wood and lignocellulosic filled composites. *Polymers*, *12*(9), 2115.

Lin, C. L., Lin, J. L., & Ko, T. C. (2002). Optimisation of the EDM Process Based on the Orthogonal Array with Fuzzy Logic and Grey Relational Analysis Method. In *Int J Adv Manuf Technol* (Vol. 19). London: Springer-Verlag London Limited.

Liu, N., Ren, K., Zhang, W., Zhang, Y. F., Chew, Y. X., Bi, G. J., & Fuh, J. Y. H. (2021). An evolutional algorithm for automatic 2D layer segmentation in laser-aided additive manufacturing. *Additive Manufacturing*, *47*, 102342.

Ma, H., & Suhling, J. C. (2009). A review of mechanical properties of lead-free solders for electronic packaging. *Journal of Materials Science*, *44*(5), 1141–1158. https://doi.org/10.1007/s10853-008-3125-9

Mohamed, O. A., Masood, S. H., & Bhowmik, J. L. (2016). Optimization of fused deposition modeling process parameters for dimensional accuracy using I-optimality criterion. *Measurement*, *81*, 174–196. https://doi.org/https://doi.org/ 10.1016/j.measurement.2015.12.011

Moscicki, L. & Janssen, L., (Eds.). (2009). *Thermoplastic starch: a green material for various industries*. John Wiley & Sons.

Mouallif, I., Latrach, M', A., Chergui, H., Benali, A., Barbe, N., Ftir, N. B., Mouallif, I., Latrach, A., Chergui, M., Benali, A., & Barbe, N. (n.d.). *FTIR study of HDPE structural changes, moisture absorption and mechanical properties variation when exposed to sulphuric acid aging in various temperatures*. Retrieved https://hal.science/hal-03420950

Ngo, T. D., Kashani, A., Imbalzano, G., Nguyen, K. T. Q., & Hui, D. (2018). Additive manufacturing (3D printing): A review of materials, methods, applications and challenges. In *Composites Part B: Engineering* (Vol. 143, pp. 172–196). New York: Elsevier Ltd. https://doi.org/10.1016/j.compositesb.2018.02.012

Nguyen, N. A., Bowland, C. C., & Naskar, A. K. (2018). Mechanical, thermal, morphological, and rheological characteristics of high performance 3D-printing lignin-based composites for additive manufacturing applications. *Data in Brief*, *19*, 936–950. https://doi.org/10.1016/j.dib.2018.05.130

Niaounakis, M. (2019). Recycling of biopolymers – The patent perspective. *European Polymer Journal*, *114*(September 2018), 464–475. https://doi.org/10.1016/j.eurpolymj.2019.02.027

Nida, S., Moses, J. A., & Anandharamakrishnan, C. (2020). Biopolymers and biocomposites from agricultural waste. In *Advanced Green Materials: Fabrication, Characterization and Applications of Biopolymers and Biocomposites* (pp. 279–295). New York: Elsevier. https://doi.org/10.1016/B978-0-12-819988-6.00013-6

Oehlmann, P., Osswald, P., Blanco, J. C., Friedrich, M., Rietzel, D., & Witt, G. (2021). Modeling Fused Filament Fabrication using Artificial Neural Networks. *Production Engineering*, *15*(3–4), 467–478. https://doi.org/10.1007/s11740-021-01020-y

Okolie, J. A., Epelle, E. I., Nanda, S., Castello, D., Dalai, A. K., & Kozinski, J. A. (2021). Modeling and process optimization of hydrothermal gasification for hydrogen production: A comprehensive review. *The Journal of Supercritical Fluids*, *173*, 105199. https://doi.org/https://doi.org/10.1016/j.supflu.2021.105199

Pazhamannil, R. V., Govindan, P., & Sooraj, P. (2021). Prediction of the tensile strength of polylactic acid fused deposition models using artificial neural network technique. *Materials Today: Proceedings*, *46*, 9187–9193. https://doi.org/https://doi.org/10.1016/j.matpr.2020.01.199

Pilla, S. (2011). Engineering Applications of Bioplastics and Biocomposites - An Overview. In *Handbook of Bioplastics and Biocomposites Engineering Applications 1*(1), 2–4). Scrivener Publishing LLC.

Porras, A., Maranon, A., & Ashcroft, I. A. (2016). Optimal tensile properties of a Manicaria-based biocomposite by the Taguchi method. *Composite Structures*, *140*, 692–701. https://doi.org/10.1016/j. compstruct. 2016.01.042

Potočnik, P., Jeromen, A., & Govekar, E. (2024). Genetic Algorithm-Based Framework for Optimization of Laser Beam Path in Additive Manufacturing. *Metals*, *14*(4). https://doi.org/10.3390/met14040410

Rabinowitz, A., DeSantis, P. M., Basgul, C., Spece, H., & Kurtz, S. M. (2023). Taguchi optimization of 3D printed short carbon fiber polyetherketoneketone (CFR PEKK). *Journal of the Mechanical Behavior of Biomedical Materials*, *145*, 105981. https://doi.org/https://doi.org/10.1016/ j.jmbbm. 2023.105981

Rahman, W. A. W. A., Isa, N. M., Rahmat, A. R., Adenan, N., & Ali, R. R. (2010). Rice husk/high density polyethylene bio-composite: Effect of rice husk filler size and composition on injection molding processability with respect to impact property. *Advanced Materials Research*, *83–86*, 367–374. https://doi.org/10.4028/www.scientific.net/AMR.83-86.367

Rao, R. V., & Rai, D. P. (2016). Optimization of fused deposition modeling process using teaching-learning-based optimization algorithm. *Engineering Science and Technology, an International Journal*, *19*(1), 587–603. https://doi.org/10.1016/j.jestch.2015.09.008

Rashed, K., Kafi, A., Simons, R., & Bateman, S. (2022). Fused filament fabrication of nylon 6/66 copolymer: parametric study comparing full factorial and

Taguchi design of experiments. *Rapid Prototyping Journal*, *28*(6), 1111–1128. https://doi.org/10.1108/RPJ-06-2021-0139

Rodi, E. G., Langlois, V., Renard, E., Sansalone, V., & Lemaire, T. (2018). Biocomposites based on poly (3-hydroxybutyrate-co-3-hydroxyvalerate) (PHBHV) and Miscanthus giganteus fibers with improved fiber/matrix interface. *Polymers*, *10*(5). https://doi.org/10.3390/polym10050509

Roy, S. B., Shit, Dr. S. C., Gupta, Dr. R. A. Sen, & Shukla, Dr. P. R. (2014). A Review on Bio-Composites: Fabrication, Properties and Applications. *International Journal of Innovative Research in Science, Engineering and Technology*, *03*(10), 16814–16824. https://doi.org/10.15680/ijirset.2014.0310058

Sai Revanth, J., Sai Madhav, V., Kalyan Sai, Y., Vineeth Krishna, D., Srividya, K., & Mohan Sumanth, C. H. (2019). TGA and DSC analysis of vinyl ester reinforced by Vetiveria zizanioides, jute and glass fiber. *Materials Today: Proceedings*, *26*(xxxx), 460–465. https://doi.org/10.1016/j.matpr.2019.12.082

Sánchez-Safont, E. L., Aldureid, A., Lagarón, J. M., Gámez-Pérez, J., & Cabedo, L. (2018). Biocomposites of different lignocellulosic wastes for sustainable food packaging applications. *Composites Part B: Engineering*, *145*, 215–225. https://doi.org/https://doi.org/10.1016/j.compositesb.2018.03.037

Sandia National Laboratory. (2022). *The Dakota - Sandia National Laboratory*. United States: National Technology and Engineering Solutions of Sandia, LLC.

Schirmeister, C. G., Hees, T., Licht, E. H., & Mülhaupt, R. (2019). 3D printing of high density polyethylene by fused filament fabrication. *Additive Manufacturing*, *28*(May), 152–159. https://doi.org/10.1016/j.addma.2019.05.003

Schultz, N., Fazli, A., Piros, S., Barranco-Origel, Y., DeLa Cruz, P., & Schneider, D. Y. (2024). Characterization of Mycelium Biocomposites under Simulated Weathering Conditions. *ACS Applied Bio Materials*. *7*(12), 8408-8422.

Sengupta, A., Pattnaik, S., & Sutar, M. K. (2017). Biocomposites : An Overview. *International Journal of Engineering Technology Science and Research*, *4*(8), 648–653.

Shah, A. ur R., Imdad, A., Sadiq, A., Malik, R. A., Alrobei, H., & Badruddin, I. A. (2023). Mechanical, Thermal, and Fire Retardant Properties of Rice Husk Biochar Reinforced Recycled High-Density Polyethylene Composite Material. *Polymers*, *15*(8). https://doi.org/10.3390/polym15081827

Shakeri, Z., Benfriha, K., Shirinbayan, M., Ahmadifar, M., & Tcharkhtchi, A. (2021). Mathematical modeling and optimization of fused filament fabrication (Fff) process parameters for shape deviation control of polyamide 6 using taguchi method. *Polymers*, *13*(21). https://doi.org/10.3390/polym 13213697

Sharma, R., Singh, R., & Batish, A. (2020). On multi response optimization and process capability analysis for surface properties of 3D printed functional prototypes of PVC reinforced with PP and HAp. *Materials Today: Proceedings*, *28*, 1115–1122. https://doi.org/https://doi.org/10.1016/j. matpr.2020.01.092

Shieh Em, T., & Chee Kiong, S. (2023). Optimization of Process Parameters for Polylactic Acid (PLA) of FDM Using Particle Swarm Optimization (PSO). *Research Progress in Mechanical and Manufacturing Engineering*, *4*(1), 205–217. https://doi.org/10.30880/rpmme.2023.04.01.022

Shirmohammadi, M., Goushchi, S. J., & Keshtiban, P. M. (2021). Optimization of 3D printing process parameters to minimize surface roughness with hybrid artificial neural network model and particle swarm algorithm. *Progress in Additive Manufacturing*, *6*(2), 199–215. https://doi.org/10.1007/s40964-021-00166-6

Singh, B. (2018). 13 - Rice husk ash. In R. Siddique & P. Cachim (Eds.), *Waste and Supplementary Cementitious Materials in Concrete* (pp. 417–460). London: Woodhead Publishing. https://doi.org/https://doi.org/10.1016/B978-0-08-102156-9.00013-4

Sood, A. K., Ohdar, R. K., & Mahapatra, S. S. (2012). Experimental investigation and empirical modelling of FDM process for compressive strength improvement. *Journal of Advanced Research*, *3*(1), 81–90. https://doi.org/https://doi.org/10.1016/j.jare.2011.05.001

Spoerk, M., Gonzalez-Gutierrez, J., Sapkota, J., Schuschnigg, S., & Holzer, C. (2018). Effect of the printing bed temperature on the adhesion of parts produced by fused filament fabrication. *Plastics, Rubber and Composites*, *47*(1), 17–24. https://doi.org/10.1080/14658011.2017.1399531

Srinivasan, R., Nirmal Kumar, K., Jenish Ibrahim, A., Anandu, K. V, & Gurudhevan, R. (2020). Impact of fused deposition process parameter (infill pattern) on the strength of PETG part. *Materials Today: Proceedings*, *27*, 1801–1805. https://doi.org/https://doi.org/10.1016/j.matpr.2020.03.777

Srivastava, M., & Rathee, S. (2018). Optimisation of FDM process parameters by Taguchi method for imparting customised properties to components. *Virtual and Physical Prototyping*, *13*(3), 203–210. https://doi.org/10.1080/17 452759.2018.1440722

Suniya, N. K., & Verma, A. K. (2023). A review on optimization of process parameters of fused deposition modeling. In *Research on Engineering Structures and Materials 9*(2), 631–659.. https://doi.org/10.17515/resm2022.520ma0909

Syed Ali Ashter. (2016). *Introduction to Bioplastics Engineering* (W. A. 2016, Ed.; 1st ed.). New York: Elsevier Science.

Tanase-Opedal, M., Espinosa, E., Rodríguez, A., & Chinga-Carrasco, G. (2019). Lignin: A biopolymer from forestry biomass for biocomposites and 3D printing. *Materials*, *12*(18), 1–15. https://doi.org/10.3390/ma12183006

Tao, Y., Wang, H., Li, Z., Li, P., & Shi, S. Q. (2017). Development and application ofwood flour-filled polylactic acid composite filament for 3d printing. *Materials*, *10*(4). https://doi.org/10.3390/ma10040339

Teharia, R., Singari, R. M., & Kumar, H. (2022). Optimization of process variables for additive manufactured PLA based tensile specimen using taguchi design and artificial neural network (ANN) technique. *Materials Today: Proceedings*, *56*, 3426–3432. https://doi.org/https://doi.org/10.1016/j.matpr.2021.10.376

Thakur, V. K., Singha, A. S., & Thakur, M. K. (2012). Biopolymers Based Green Composites: Mechanical, Thermal and Physico-chemical Characterization. *Journal of Polymers and the Environment*, *20*(2), 412–421. https://doi.org/10.1007/s10924-011-0389-y

Tran, T. N., Bayer, I. S., Heredia-Guerrero, J. A., Frugone, M., Lagomarsino, M., Maggio, F., & Athanassiou, A. (2017). Cocoa Shell Waste Biofilaments for 3D Printing Applications. *Macromolecular Materials and Engineering*, *302*(11), 1–10. https://doi.org/10.1002/mame.201700219

Utracki, L. A. (2002). *Polymer blends handbook*. Dordrecht: Kluwer Academic Publishers.

Vaissier, B., Pernot, J.-P., Chougrani, L., & Véron, P. (2019). Genetic-algorithm based framework for lattice support structure optimization in additive manufacturing. *Computer-Aided Design*, *110*, 11–23. https://doi.org/https://doi.org/10.1016/j.cad.2018.12.007

Vizureanu, P., Nabiałek, M., Perju, M. C., Achitei, D. C., Sandu, A. V., Bălțatu, M. S., & Burduhos-Nergis, D.-D. (2025). Biocomposites: Materials, Properties, and Applications. In P. Vizureanu (Ed.), *Composite Materials - Science and Engineering*. IntechOpen. https://doi.org/10.5772/intechopen.1010197

White, E., Bassilakis, R., & Nogués, S. (2020). From the plastics present to a sustainable future: the bioplastics innovation landscape, players and market opportunities. *Clarivate*^{TM}. Retrieved from https://clarivate.com/derwent/campaigns/from-the-plastics-present-to-a-sustainable-future/

Wojciechowski, S., W. Maruda, R., M. Krolczyk, G., & Niesłony, P. (2018). Application of signal to noise ratio and grey relational analysis to minimize forces and vibrations during precise ball end milling. *Precision Engineering*, *51*, 582–596. https://doi.org/https://doi.org/10.1016/j.precisioneng.2017.10.014

Yang, D., Cao, Y., Zhang, Z., Yin, Y., & Li, D. (2021). Effects of crystallinity control on mechanical properties of 3D-printed short-carbon-fiber-reinforced polyether ether ketone composites. *Polymer Testing*, *97*, 107149. https://doi.org/10.1016/j.polymertesting.2021.107149

Yang, T. C., Chien, Y. C., Wu, T. L., Hung, K. C., & Wu, J. H. (2017). Effects of heat-treated wood particles on the physico-mechanical properties and

extended creep behavior of wood/recycled-HDPE composites using the time-temperature superposition principle. *Materials*, *10*(4). https://doi.org/10.3390/ma10040365

Zhou, X., Hsieh, S. J., & Sun, Y. (2017). Experimental and numerical investigation of the thermal behaviour of polylactic acid during the fused deposition process. *Virtual and Physical Prototyping*, *12*(3), 221–233. https://doi.org/10.1080/17452759.2017.1317214

APPENDICES

Appendix I: Material Model Definition

Figure A. 1: 45 wt.% rHDPE + 25 wt.%RH+30wt.% MAPE bioplastic material model definition

Figure A. *2*: 40 wt.% rHDPE + 30 wt. % RH + 30 wt.% MAPE bioplastic material model definition

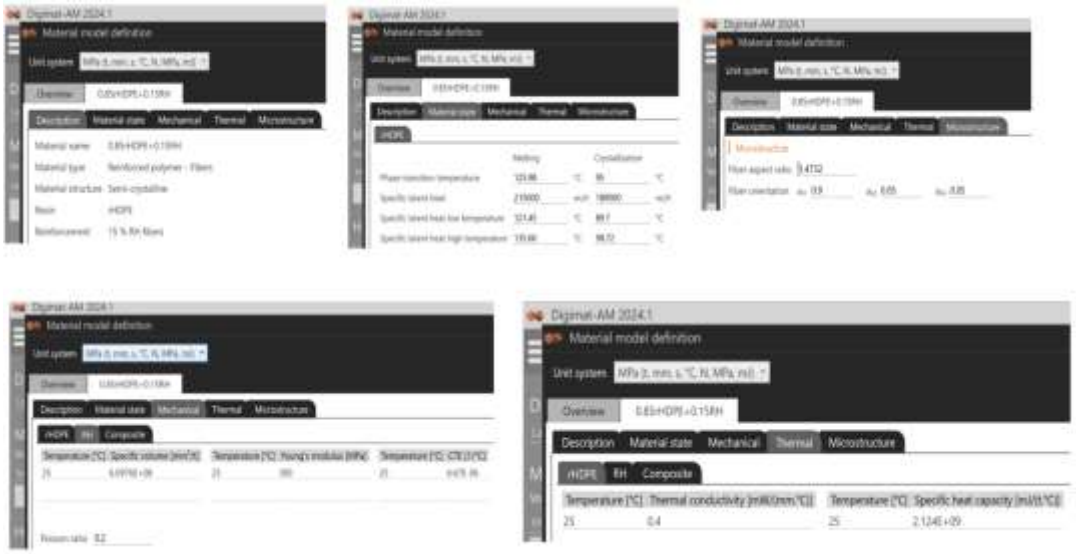

Figure *A. 3*: 85% rHDPE + 15% RH bioplastic material model definition

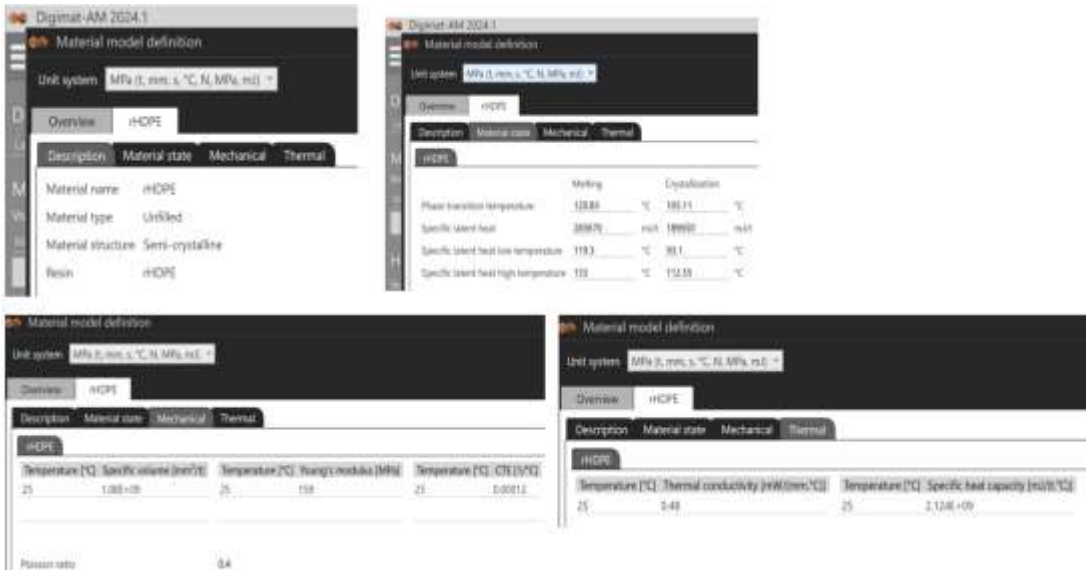

Figure A. 4: 100%rHDPE bioplastic material model definition

Appendix II: Measured Warpage

Table B. 1: Measured values of lateral warpage

Bioplastic composition	Measured warpage
100 wt. % rHDPE	1.110 ± 0.084
85 wt.% rHDPE + 15 wt.% RH	0.486 ± 0.218
40 wt. % rHDPE + 30 wt. % RH + 30 wt. % MAPE	1.360 ± 0.127

Appendix III: FFF Simulation Results

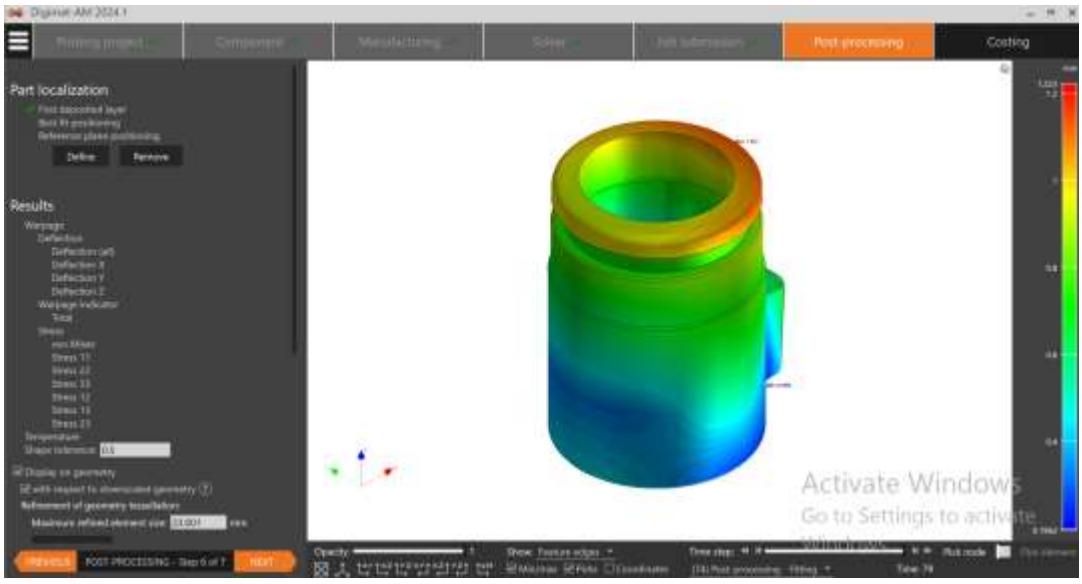

Figure B. 1: Warped geometry of the breath analyzer's adapter using the 100% rHDPE Bioplastic

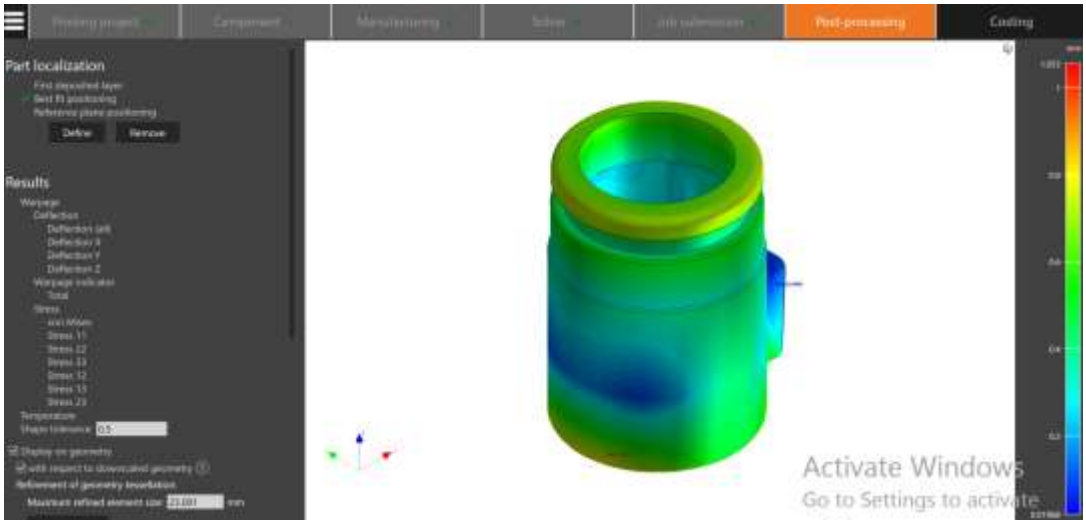

Figure B. 21: Warped geometry of the breath analyzer's adapter using the 0.4 rHDPE + 0.3RH +0.3 MAPE

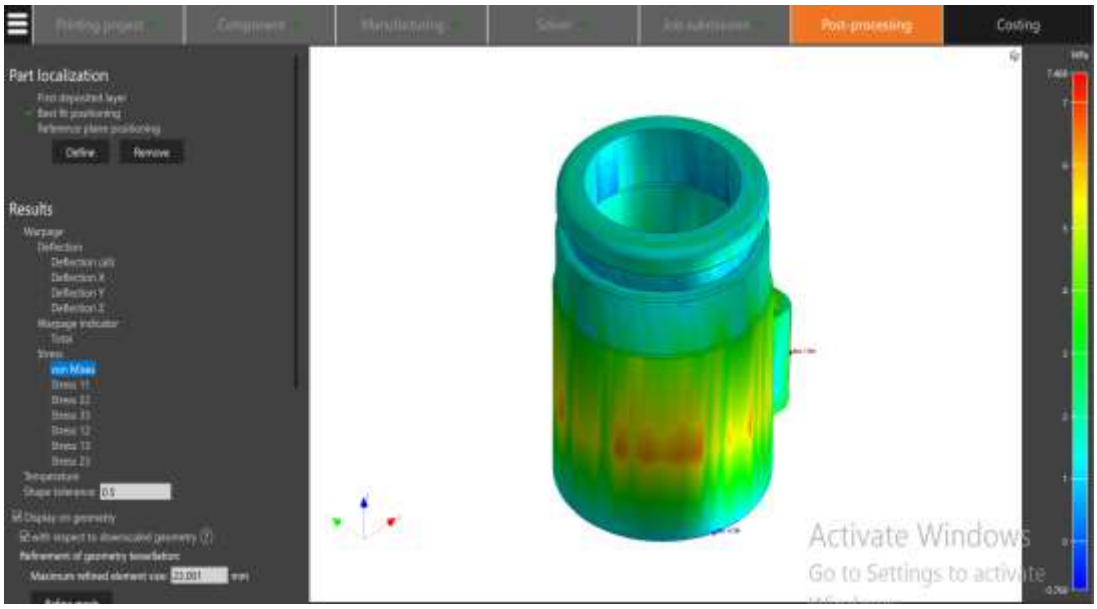

Figure B. 3: Residual stresses of the breath analyzer's adapter using the 100% rHDPE bioplastic

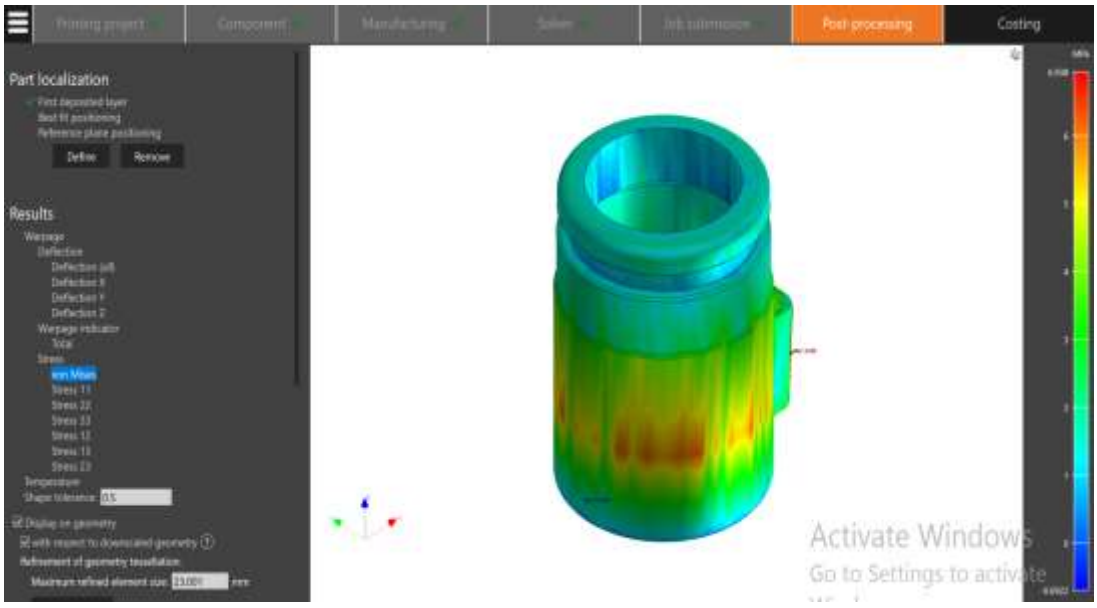

Figure B. 2: Residual stresses of the breath analyzer's adapter using 0.4 rHDPE + 0.3RH +0.3 MAPE bioplastic

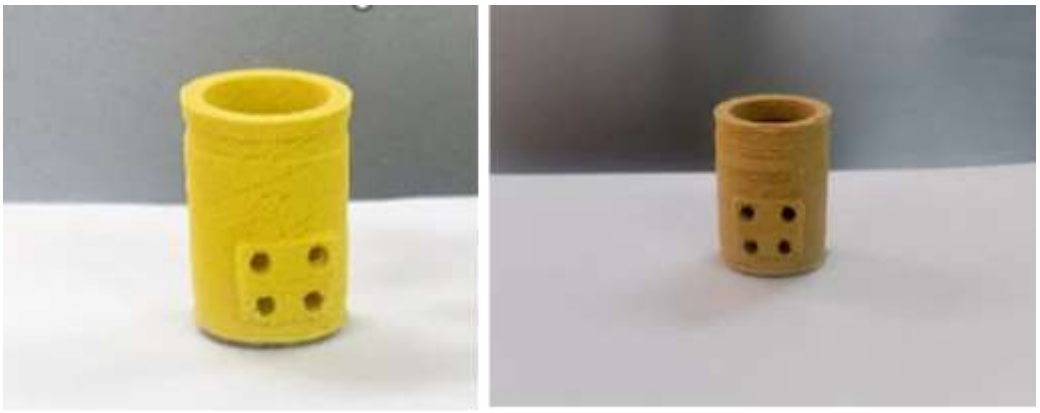

Figure B. 3: Printed adapter of the breath analyzer (a) 100 wt.% rHDPE (b) bioplastic

Appendix IV: Modules of Digimat 2024.1

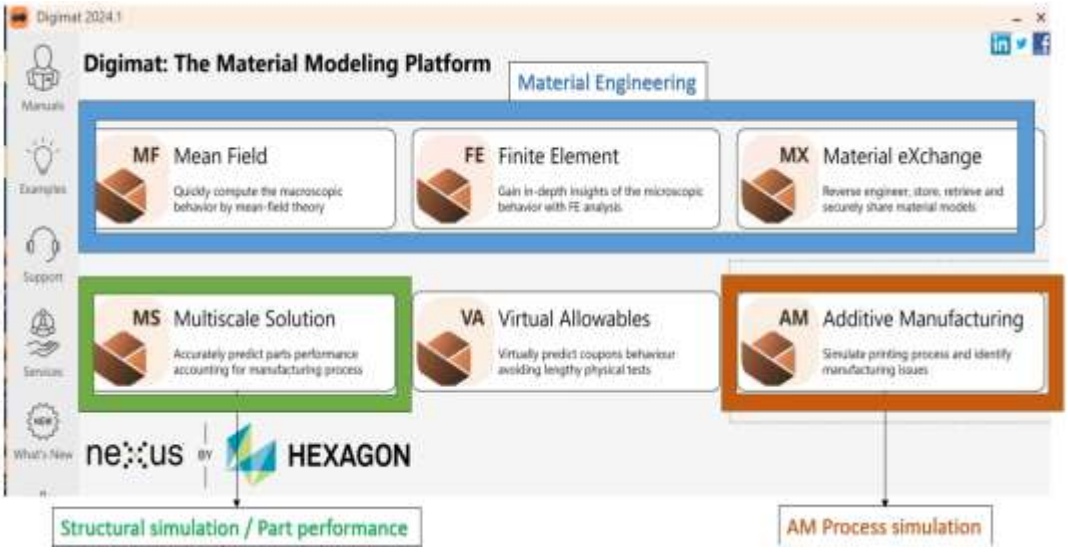

Figure C. 1: Digimat 2024.1 interface showing different modules of Digimat

i. Mean Field homogenization, MF, module is used to develop new materials which can be used in coupled simulations and to analyze materials using analytical solvers.

ii. Finite Element homogenization, FE, module is used to build a full 3D finite element model of the material, study the material's behaviour (matrix and fibers). The models used in FE are heavy and time-consuming in their analysis, hence they cannot be used for coupled simulations.

iii. The Material Exchange (MX) module is a material database that contains public materials provided by various material manufacturers, as well as MF material models developed by users for private use. It also features a tool for reverse engineering materials, where experimental data is used to calibrate material files for simulation.

iv. The Multiscale Solution (MS) module is used to run a coupled simulation. It builds a coupled model from a finite element model, 3D manufacturing data (e.g., inclusion orientation or tool path), and a material model to solve a part and determine the part's performance.

v. The Virtual Allowable (VA) module is mainly for continuous fiber materials and is not for additive manufacturing.
vi. The Additive Manufacturing (AM) module is used for the printing process simulation and identifying manufacturing issues.